STUDIES ON LANTHANUM BASED IONIC CONDUCTORS AS ELECTROLYTE MATERIALS

A

Thesis

submitted for the award of

DOCTOR OF PHILOSOPHY

Submitted by

KAPIL SOOD

(Regn. No. 950912004)

School of Physics and Materials Science
Thapar University, Patiala-147004
(Punjab) India

July-2014

CERTIFICATE

This is to certify that the thesis entitled **"Studies on Lanthanum based ionic conductors as electrolyte materials"** which is being submitted by Kapil Sood in fulfillment of the requirements for the award of the degree of Doctor of Philosophy in School of Physics and Materials Science, Thapar University, Patiala (Punjab), India is an exclusive record of candidate's own research work under our guidance and supervision. The thesis in part or in full has not been submitted in any other university or institute for the award of any degree. The thesis is fit to be considered for the award of degree of Doctor of Philosophy.

Dr. O. P. Pandey
Senior Professor and Dean [R & SP]
School of Physics and Materials Science
Thapar University
Patiala-147004 (INDIA)

Dr. Kulvir Singh
Professor and Associate Dean [Strategy]
School of Physics and Materials Science
Thapar University
Patiala-147004 (INDIA)

Date: 15-10-2014

Acknowledgement

This thesis is the result of a challenging journey, upon which many people have contributed and given their support. I would like to thank all those people who made this thesis possible and an unforgettable experience for me. At the end of my thesis, it is a pleasant task to express my thanks to all those who contributed in many ways to the success of this study and made it an unforgettable experience for me.

At this moment of accomplishment, first of all, I wish to thanks my guides **Dr. O. P. Pandey**, Senior Professor and Dean (R & SP), School of Physics and Materials Science, Thapar University, Patiala and **Dr. Kulvir Singh**, Professor and Associate Dean (Strategy), School of Physics and Materials Science, Thapar University, Patiala for their interest and encouragement throughout the course of this research work. Their deep insights into the problem and ability to provide guidance and solutions have been of immense value in improving the quality of my research work at all stages.

I am very thankful to my doctoral committee members Dr. Puneet Sharma, Dr. B. N. Chudasama, Dr. Amjad Ali for their guidance, suggestions and support during my six months progress report. I warmly thank Dr. Bhupendra Chudasama and Dr. B.C. Mohanty for their valuable advice, constructive criticism and extensive discussions during the work. I am also grateful to Mr. Devender Kumar, Assistant Professor, Department of Mechanical Engineering, for his technical support throughout my work.

My special thanks are also due to all the respective faculty of School of Physics and Materials Science, Dr. K.K. Raina Distinguished Professor, Dr. N.K. Verma, Senior Professor, Dr. M.K. Sharma, Dr. Suneel Kumar, Dr. S.D. Tiwari, Dr. D.P. Singh, Ms. Loveleen Brar, Dr. Alka Upadhyay, Dr. Punam Uniyal and Dr. Soumendu Jana for their encouragement and moral supports.

Most of the results described in this thesis would not have been obtained without a close collaboration with few laboratories. I owe a great deal of appreciation and gratitude to Professor Ajit R. Kulkarni, Department of metallurgical Engineering, IIT Bombay, for providing me his lab facilities for my research work. I am also thankful to Mr. Rajan and Mr. Raj Kumar Chadda, research scholars, Department of metallurgical Engineering, IIT Bombay for their support during my stay at IIT Bombay. I am also thankful to Dr. Prabhakar Singh, Professor, Department of

Applied Physics, IITBHU, for providing his lab facilities for my research work. I wish to offer my thanks to Mr. Praveen Kumar and Mr. Raghuvendra Kumar, research scholars, Department of Applied Physics, IITBHU for their help in my research work. I am also thankful to Dr. Vinay Gupta, Professor, and Dr. Monica, Assistant Professor, Department Physics and Astro-Physics, Dr. Roy Johnson, Scientist F & team leader, Dr. Suresh, Scientist C, ARCI, Hydrabad, for providing their lab facilities for my research work.

My sincere thanks are due to Mr. Purushotam, Mr. Jant Singh, Mr. Ghanshyam, Mr. Mukesh Kumar, Mr. Indermani for their valuable help and technical support.

This journey was not that beautiful without you my friends, especially Mr. Paramjyot Jha and Mr. Gourav Singla, Research scholars, SPMS, Thapar University, Patiala, who always helped and supported personally and technically throughout the way. You guys are amazing in too many ways. I am also thankful to Mr. Suresh (nick name *chacha*) who is wonderful and supportive for me. Words are not enough for expressing my sincere thanks to my friends Dr. Vishal Kumar, Dr. Dinesh Kumar, Dr. Harjinder Singh, Dr. Satnam Singh, Dr. Akshay, Dr. Kamalpreet, Dr. Jasmeet, Dr. Bhupinder, Dr. Gurbinder, Dr. Dinesh Pathak, Dr. C.P. Khattar, Dr. Ravi Kant, Dr. Anu, Ms. Mani, Ms. Jagdeep, Ms. Chandni, Ms. Samita, Mrs. Samiksha, Ms. Sakshi, Ms. Parveer, Mr. Mintu, Mr. Satwinder, Mr. Rishi, Mr. Jaspal, Ms. Kamal, Ms. Geetanjali, Mr. Vinoth. A special thanks to Mr. Sunil Kumar Arya, for his friendly and moral support during crucial time. I am also thankful to Ms. Shivani Sharma, research scholar, UGC-DAE, Indore for her valuable discussion and support on Rietveld refinement. I am also thankful to my close friend Mr. Harminder Singh, Assistant Professor, BGIET, Sangrur, who was always with me in every up and downs during my Ph.D work.

My wife Mrs. Shivani Sood, deserves a special thanks for her patience, persistent moral support and capability to revitalize me during the course of the PhD work at each step. She was always there to stand with me in my ups and down. You really made the things possible for me.

I am also grateful to my mother Mrs. Suman Sood and my father Mr. Kedar Nath Sood for their tremendous support throughout this beautiful journey of research. I am also thankful to my sister Ms. Shailja Sood and brother Mr. Atul Sood for providing me unconditional support.

Above all, hidden force by Almighty God steered me in the right direction to achieve the goal.

Kapil Sood

LIST OF PUBLICATIONS

SCI Journals.

[1] Studies on Sr substituted lanthanum indate as mixed ionic Conductor, Kapil Sood, K. Singh, O.P. Pandey, Journal of Materials Science, 47 (2012) 4520-4529.

[2] Study of the Structural and Electrical Behaviour of Ca Doped $LaInO_3$ Electrolyte Material, Kapil Sood, K. Singh, O.P. Pandey, Transactions of Indian Ceramic Society, 72 (2013) 32-35.

[3] Structural, Conductivity and Dielectric Relaxation Studies of $La_{0.9}Ba_{0.1}GaO_{3-\delta}$ System, Kapil Sood, K. Singh, O.P. Pandey, Particulate Science and Technology **(DOI: 10.1080/02726351.2014.938379).**

[4] Co-existence of cubic and orthorhombic phases in Ba-doped $LaInO_3$ and their effect on conductivity, Kapil Sood, K. Singh, O.P. Pandey, Physica B, 456 (2015) 250-257.

Non-SCI Journals.

[1] AC Conductivity and Dielectric Relaxation Studies of $La_{0.95}Sr_{0.05}GaO_{2.975}$ Gallate, Advanced Materials Research, 585 (2012) 205-209.

Under review:

[1] Preferential occupancy of Ca^{2+} dopant in $La_{1-x}Ca_xInO_{3-\delta}$ (x=0-0.20) perovskite: structural and electrical properties, Kapil Sood, K. Singh, O.P. Pandey, Journal of Molecular structure, (**under 2nd revision**).

[2] "Structural and electrical study of Ba-doped $LaGaO_3$ composite electrolyte" Kapil Sood, K. Singh, O.P. Pandey, Journal of Renewable energy Sources, (**under 1st revision**).

Papers presented in national and international conferences:

[1] Kapil Sood, K. Singh, O.P. Pandey , "Study of the structural and electrical behavior for Ca doped $LaInO_3$ electrolyte material", **International conference/Platinum jubilee session of the Indian Ceramic society" Shilpgram, Agra, India** (Dec 20-22, 2011).

[2] Kapil Sood, K. Singh, O.P. Pandey , "Study of The Effect On Ionic Conductivity And Structral Morphology of The Sr Doped Lanthanum Gallate Solid Electrolyte" **Asian conference on solid state ionics, Tohoku University, Sendai, Japan** (Jul 17-20, 2012).

[3] Kapil Sood, K. Singh, O.P. Pandey , "AC Conductivity and Dielectric Relaxation Studies of $La_{0.95}Sr_{0.05}GaO_{2.975}$ Gallate " **International conference on advances in materials and processing: challenges and opportunities" IIT, Roorkee, India** (Nov 2-4, 2012).

[4] Kapil Sood, K. Singh, O.P. Pandey , "Structural and conductivity studies of doped lanthanum gallate" **37th International conference on advanced ceramics and composites" Daytona, Florida, USA** (Jan27-Feb1, 2013).

[5] Kapil Sood, K. Singh, O.P. Pandey , "Study of Structural and Electrical Behavior for Ca Doped $LaInO_3$ Electrolyte" **National Symposium on Materials and Processing-2012" Multipurpose Hall, Training School Hostel, Anushaktinagar, BARC, Mumbai- 400 094** (Oct 10-12, 2012).

[6] Kapil Sood, K. Singh, O.P. Pandey , "Study of the electrical properties for Ca-doped $LaInO_3$ electrolyte material" **19th International conference on solid state Ionics" Kyoto, Japan** (June 2-7, 2013).

[7] Kapil Sood, K. Singh, O.P. Pandey, "Conductivity and dielectric relaxation studies Ba-doped lanthanum gallate" **International Conference & Exhibition of Powder, Granule and Bulk Solids: Innovations and Applications, Thapar University, Patiala, Punjab** (Nov 28-30, 2013).

Index

List of figures

List of tables

Abstract

Solid oxide fuel cell (SOFC) is the most efficient fuel cell where different fuels can be used without any external reformers. Additionally, they are portable and cost-effective as compared to other cells. However, the high operating temperature of SOFC leads to decrease its life and efficiency as material used in SOFC start degrading with time. Because of chemical reactions within the components of SOFC at high temperature reduce its life, the need is felt to reduce its operating temperature without compromising the properties of the SOFCs. Therefore, material development, particularly electrolyte is very critical for the commercialization of intermediate temperature (IT) SOFCs. Among all the electrolyte materials, perovskite based oxide ion conductors, particularly, Sr- and Mg-doped lanthanum gallate (LSGM) are of great interest. The ionic conductivity of LSGM is higher than those of YSZ and scandia stabilized zirconia (SSZ) and lower than that of gadolinia doped ceria (CGO). Moreover, LSGM does not have an easily reducible ion, like Ce^{4+}. Therefore, LSGM is better than Gd doped CeO_2. The conductivity of LSGM depends on dopant concentration, particularly with transition element doping that shows good conductivity, especially at temperatures, upto 600 ºC. Moreover, the performance of these electrolytes is still a major issue. Lanthanum based perovskites including $LaScO_3$, $LaInO_3$, $LaYO_3$ and $LaAlO_3$ are used as oxygen ion conductors and are suitable electrolyte materials for SOFC. Considering these facts, it has been planned to investigate the effect of systematic doping of SrO, BaO and CaO in $LaGaO_3$ and $LaInO_3$ system. The work carried out in this Ph.D thesis is divided into five chapters.

Chapter 1 contains introductory aspects of fuel cells (FCs) and describes a brief overview of different categories of FC types, their design and role of different components. Since, the present work is on development of electrolyte material for IT-SOFCs, so, emphasis is given on the factors that influence ionic motion. The origin of perovskite structure and their properties are explained. Study reveals that systematic investigation is required to find suitable electrolyte, which can be used in IT-SOFCs.

Chapter 2 describes the detailed literature review on various types of solid electrolytes used. It includes the review of structural, thermal, morphological, and electrical study of yttria stabilized zirconia (YSZ), ceria based systems, bismuth based system, pyrochlore based systems and lanthanum based perovskites. From the literature review, it was concluded that lanthanum based

electrolytes are most suitable for their use in IT-SOFCs. However, systematic study of uniform doping in $LaGaO_3$ and $LaInO_3$ synthesis has not been studied in detail. The reason for selecting the dopants to achieve the required properties has been explained and accordingly the objectives of the present work have been defined.

Chapter 3 describes the source of raw materials used and synthesis route followed to prepare the samples. It also describes the techniques utilized for structural, electrical and thermal characterization of solid electrolyte. These techniques include X-ray diffraction (XRD) for phase identification, Raman spectroscopy to analyze structural modification with doping, scanning electron microscopy (SEM) for morphological study and energy dispersive spectroscopy (EDS) for semi-quantitative elemental analysis. Besides this, thermal expansion coefficient (TEC) of each sample was measured to study the lattice expansion behavior of electrolyte at higher temperatures. Thermogravimetric analysis (TGA) is used to analyze thermal stability at higher temperatures. Two probe impedance spectroscopy (IS) technique was used to study the electrical conduction behavior of the synthesized materials.

Chapter 4 describes the results and discussion part of the synthesized samples. This chapter is divided into six sections. In the first section, $La_{1-x}Sr_xGaO_{3-\delta}$ (where, x=0.0-0.20) system was analyzed. The substitution of Sr^{2+} at La-site of $LaGaO_3$ forms solid solulion upto 10 mol%. The strain increases uniformly with Sr-substitution for all the synthesized samples. 5 mol% Sr-substitution leads to vacancy ordering within the system. It resulted in lesser electrical conductivity of this sample. However, 10 mol% Sr-content shows highest conductivity (2.37 mS/cm at 800 °C) among all the synthesized samples. Higher substitution (15 and 20 mol%) leads to formation of secondary phase ($LaSrGa_3O_7$) which adversely affected the overall conductivity of the system. Moreover, the Sr-content decreased the grain size in comparison to unsubstituted sample. TEC values of this system are in the required range for SOFC applications. In the second series, $La_{1-x}Ba_xGaO_{3-\delta}$ (where, x=0.0-0.20) system was analyzed. Phase identification followed by Rietveld refinement of selected samples was done. This study revealed that Ba^{2+} substitution leads to stabilization of rhombohedral phase at room temperature, which facilitates the increase in overall conductivity upto 15 mol% Ba-content. Moreover, the activation energy values of Ba-substituted samples (~0.65 eV from 600-800 °C) indicates that conduction in this system is mainly due to oxygen ions.

In the third series, $La_{1-x}Ca_xGaO_{3-\delta}$ (where, ×=0.0-0.20) system was analyzed. Morphological features indicated that Ca-content facilitated better sinterability and grain growth in the synthesized samples. Ca-substituted samples formed single phase upto 10 mol%, above which secondary phase ($LaCaGa_3O_7$) formation takes place. The highest conductivity achieved is 3.8 mS/cm at 800 °C for LCG-10 sample. The activation energy values (~1.15 eV from 600-800 °C) are higher than Sr and Ba-substituted systems.

In the fourth series, $La_{1-x}Sr_xInO_{3-\delta}$ (where, ×=0.20-0.50) system was analyzed. The solid solubility limit was achieved upto 20 mol% Sr-content. LSI-23 possesses highest conductivity (0.16mS/cm at 800 °C) in this series. However, increased Sr-content also increases porosity in the sample. At higher temperature, the conductivity phenomenon changes from protonic to oxide ion conductivity in all the samples. The LSI-23 is most stable at higher temperature in reducing atmosphere. The thermal expansion of LSI-23 sample is also in the required range of SOFCs.

In the fifth series, $La_{1-x}Ba_xInO_{3-\delta}$ (where, ×=0.0-0.20) system was analyzed. Ba-substituted system was single phase up to 5 mol%, above which polymorphic cubic perovskite phase (***pm$\bar{3}$m***) was co-formed. Raman analysis indicated A-site substitution of Ba-ion and formation of oxygen vacancies with substitution. LBI-10 shows the highest ionic conductivity among all the investigated samples. The SEM analysis indicated the formation of well packed grains.

In the last series, Ca-substituted lanthanum indate ($La_{1-x}Ba_xInO_{3-\delta}$, where ×=0.0-0.20) was investigated. The $LaInO_3$ formed single phase up to 10 mol% of Ca-substitution. Ca-content leads lattice expansion due to partial Ca^{2+} occupancies at In-sites. It is also confirmed from the Raman bands, particularly 180-300 cm^{-1} shifted to the lower wave number. The decrease in intensity and an increase in FWHM in Raman bands with substitution indicated the disorderness in the system. The Arrhenius plots of all LCI samples show almost linear behavior. The activation energy values indicated that the conduction is dominated by ion movement.

Chapter 5 describes the overall conclusion drawn from the entire study. Based on the present work, the scope for the future work is also provided at the end of this section.

Appendix

Symbol used and their abbreviations

Symbol	**Abbreviations**
Sr	Strontium
Ba	Barium
Ca	Calcium
La	Lanthanum
In	Indium
Ga	Gallium
O	Oxygen
N	Nitrogen
a, b, c	Unit cell lattice parameters
V	Unit cell volume
g	Occupancy ratio
x, y, z	Atomic positions
Å	Angstrom
R_s	Series resistance
R_b	Bulk (grain) resistance
R_{gb}	Grain-boundary resistance
C_b	Bulk (grain) capacitance
C_{gb}	Grain-boundary capacitance
F	Farad
$\in$	Strain
τ	Relaxation time
f	Linear frequency
ω	Angular frequency
σ	Conductivity
E_a	Activation energy
k	Boltzmann constant
T	Temperature
ρ	Electrical resistivity
l	Thickness of disc
A	Area of disc
α	Thermal expansion coefficient

Chapter I

INTRODUCTION

OVERVIEW

This chapter describes the requirement of energy and its fulfillment through alternative sources, particularly by fuel cells. Among the various fuel cells, solid oxide fuel cell (SOFC) is one of the important electrochemical energy devices where compound oxides are used as an electrolyte. The present work deals with the development of solid electrolyte, which is one of the main components of SOFC. The parameters which affect the working of SOFC are also discussed along with the importance of operating temperature. It is observed that intermediate temperature (IT) SOFCs are practically more viable for commercialization of SOFCs. Furthermore, the cell configuration also plays an important role on the overall performance of SOFCs. The different types of solid electrolytes which can be used in IT-SOFCs are described and discussed. In case of perovskite (ABO_3 structure) type electrolytes, it is observed that selective doping on A- and B-site of ABO_3 systems can enhance the ionic conductivity, density, phase stability and compatibility with other components of SOFC. The effects of porosity, density and grain size on conductivity of electrolytes are discussed in this chapter.

1.1. Clean energy and requirements:

With continuous growth in population, the energy demand is also increasing. As per the survey of energy resources, the world energy demand is expected to double by 2050 [1]. At the same time, available energy resources are expected to increase by 1.5 to 3 times [2]. Moreover, this growing energy demand has posed the problem of green house gas emission. According to latest reports, carbon-dioxide (CO_2) levels in the atmosphere have exceeded 400 parts per million (ppm) for the first time in several hundred millennia [3]. The scientific analysis indicates that, the climate change has resulted unexpected weather events such as floods, storms, localized heavy rain falls, which has become more frequent and intense. It has caused an increase in global temperature and rise in sea levels. In addition to these factors, the major challenge is to limit the global temperature rise below 2 °C. The energy production is the main cause since it contributes two-third of greenhouse-gas emissions, where more than 80% of global energy consumption is based on fossil fuels [3].

Despite many efforts, a historic increase in CO_2 emissions have occurred and has gone to 1.4% higher to reach 31.6 gigatonnes (Gt) in 2012. In Asian countries, especially India has experienced increasing demand for energy because of rapid economic growth. Asian economics is mainly relying on coal and nuclear energy to meet their demand. However, the accident at the Fukushima Daiichi nuclear power plant and Chernobyl disaster in Russia has not only affected the world, but its impact is directly felt in Asia. Because of this, many countries have taken high safety measures and also reduced their energy dependency on nuclear power plants.

Renewable-energy sources have great advantages to meet decentralized needs. The safe renewable-energy sources are: solar cells, wind mills and fuel cells. Among these, fuel cells have attracted wide attention due to their high efficiency, versatile fuel adaptability, portability, reliability and combustion-free output, which makes them most suitable for future energy source. Additionally, it is considered a clean source of energy due to the production of water (H_2O steam) and electricity.

1.2. Fuel cells:

Fuel cells (FCs) are the electrochemical energy devices which convert the Gibb's free energy stored in a liquid or gaseous fuel, e.g., H_2, CH_4, CH_3OH, C_2H_5OH, etc., directly to electric energy with high efficiency. This type of conversion process is quite different from the classical thermodynamically conversion process. It is not limited by Carnot's principle [4]. The Carnot's cycle describes the thermodynamic processes occurring during the

expansion/compression of the gas [5]. Since, fuel cells convert chemical energy directly to electrical energy, so Carnot principle, which limits the efficiency is not applicable in FCs. All fuel cells contain two electrodes i.e. cathode and anode separated by an electrolyte. At the anode side, the fuel is oxidized to form positive ions, which may pass through proton conducting membrane (electrolyte) and react with O_2 or air at the cathode-electrolyte interface to give H_2O as a product and electrons will pass through an external circuit to give electricity as an output. Moreover, FCs emits least harmful gases like CO_2 in petroleum fuels, so these cells are eco-friendly. The operating principle in terms of thermodynamics can be defined as: The electromotive force (E^o) of the fuel cell is the difference between reduction potentials at the cathode and anode reactions, which is always positive. The standard free energy change (ΔG^o) of the overall reaction of the fuel cell is given by equation 1.1:

$$\Delta G^o = -nFE^o_{,cell} \quad (1.1)$$

where, n is the number of electrons transferred and F is Faraday's number (96.475 °C/equivalent) [6]. The n, F and E_o are positive numbers and the standard free energy change is negative, indicating a spontaneous reaction. FCs can be classified in a number of ways depending upon the type of electrolytes used. There are six types of FCs based on the type of electrolyte used.

1. Phosphoric acid fuel cell (PAFC).
2. Alkaline fuel cell (AFC).
3. Proton exchange membrane fuel cell (PEMFC).
4. Direct methanol fuel cell (DMFC).
5. Molten carbonate fuel cell (MCFC).
6. Solid oxide fuel cell (SOFC).

The comparative features of these fuel cells are given in Table 1.1. This comparison indicates that SOFCs are the best choice for further investigation.

SOFCs exhibit higher efficiency than above-mentioned fuel cells. The present work is also related with the development of electrolytes for SOFC. So, in this section, the working of SOFC, its components are discussed.

Table 1.1: Comparison between various types of fuel cells.

	PAFC	**AFC**	**PEMFC**	**DMFC**	**MCFC**	**SOFC**
Electrolyte	Aqueous phosphoric acid	Liquid KOH	Solid polymer	Polymer ion exchange	Immobilized molten carbonate	Ceramic
Charge carrier	H^+	OH^-	H^+	H^+	CO_3^{2-}	O^{2-}
Operating temperature	150-200 °C	100-250 °C	~80 °C	~ 70 °C	600-800 °C	600-1000 °C
Efficiency	40%	60%	60%	~ 70%	~ 80%	~85%
Power range (W)	10k-1000k	500-10k	1-100k	1-100	100k-10000k	1k-10000k
Primary contaminate sensitivities	CO	CO and CO_2	CO and NH_3	CO	Sulphur	_____
Main advantages	Impure H_2 can be used as fuel, use in stationary power stations.	Internal reforming not required, used for transport applications.	Automobile applications	Portable applications, methanol can be used as fuel.	Good efficiency and less noice.	Flexible in fuel, portable, higher efficiency and expansive catalyst like Pt not reqd.

1.3. Solid oxide fuel cells (SOFCs):

SOFCs have emerged as the most suitable FCs among the investigated cells. In SOFC, oxygen reacts catalytically to form oxide ions at the cathode, which passes through the electrolyte. At the anode side, these oxide ions react with fuel (e.g., H_2) to form water and electrons flow through an external circuit to give electricity as output. In actual practice, the oxygen partial pressure between cathode and anode is responsible to move oxide ions through the electrolyte. The SOFCs operate at high temperature (600-1000 °C) and has high efficiency in co-generation (~85%). The reactions that take place in the cell are given as:

$$\frac{1}{2}O_2 + 2e^- \rightarrow O^{2-} \qquad (1.2)$$

at the cathode:

$$H_2 + O^{2-} \rightarrow H_2O + 2e^- \qquad (1.3)$$

with the overall cell reaction:

$$\frac{1}{2}O_2 + H_2 \rightarrow H_2O \quad (1.4)$$

Further, CO and hydrocarbons such as CH_4 can also be used as fuel in SOFC. At the high temperatures within the cell, it is feasible that the water gas may shift the reaction as follows:

$$CO + H_2O \rightarrow H_2 + CO_2 \quad (1.5)$$

and the steam reforming reaction as given in equation (1.6) takes place to produce H_2, which is easily oxidized at the anode [7].

$$CH_4 + H_2O \rightarrow 3H_2 + CO \text{ (in the case of natural gas)} \quad (1.6)$$

The direct oxidation of CO in fuel cells is well established, while the direct oxidation of CH_4 has not been thoroughly investigated. Any sulfur compound present in the fuel has to be removed prior to use in the cell to a concentration <0.1 ppm.

High operating temperature of SOFC (600-1000 °C) produces high quality of heat which can be used for co-generation. This temperature also enables to achieve high-efficiency conversion of fuel to electricity [8]. They are flexible in the choice of fuel such as carbon-based fuels, natural gas, H_2 etc. It also possesses some limitations, which are summarized in Table 1.2.

Table 1.2: Merits and demerits of solid oxide fuel cells [9].

Features	**Merits**	**Demerits**	**Solutions**
High-temperature operation	High conversion efficiency, Hybrid system with gas turbines cogeneration system.	Thermal stress. Long start-up time.	Sealless tubular
All solid	Long life, no need for water management	Difficult to stack, volume change cause degradation,	Monolithic cells Anode supported cells Microtubes
Membrane Reactor	CO_2 removal	Difficulty of 100% fuel utilization	Hybrid system with gas turbine

1.4. Cell configuration:

SOFCs are made in a variety of sizes. Individual fuel cells produce relatively small electrical potentials~0.7 volt. Cells are stacked to increase the voltage and meet an application's requirements [10]. Two types of major stack design are being used:

1. Tubular SOFCs.
2. Planar SOFCs.

1.4.1. Tubular design:

Tubular SOFCs have good thermal shock resistance, high mechanical strength, easy sealing and high-volume manufacturing ability. For tubular design, the tube size is one of the critical parameters to be determined. Small tubes cause the problem of assembling due to the fragile nature of the tubes. The power of each cell is proportional to the size of the cell. So, larger the area of cell more will be the cell power. However, increasing the cell size in tubular will decrease the power packaging density and fuel utilization. Further, the tubular design forces the electrons to travel along a much larger path than other fuel cells, causing increased ohmic loss and lower current density [7].

1.4.2. Planar design:

The planner SOFC was the first geometry attempted for the SOFC. The schematic diagram of planner SOFC is shown in Fig. 1.1. In this design, the components are assembled in flat stacks, with fuel and air flowing through channels built into the cathode and anode.

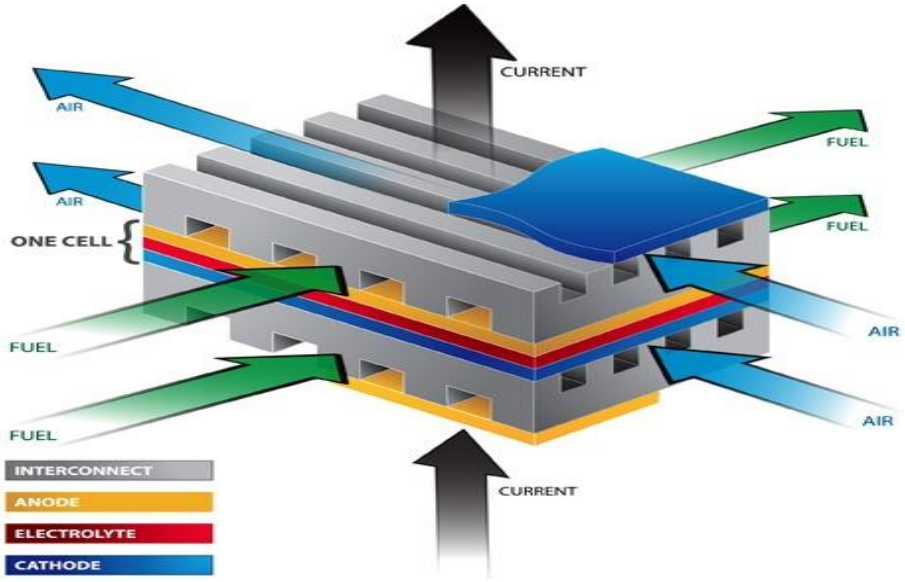

Fig. 1.1: Stacking arrangements for planar SOFCs [11].

Although it has many advantages such as higher current density than tubular design due to the short path of conduction and capable of achieving high-power densities up to 2W/cm^2 [12, 13], but the major drawbacks are the gas leakage at the higher temperature as well as the thermal mismatch with other SOFC components. Therefore, a proper sealing material is required for its better performance in SOFC stack. The fabrication techniques for planar SOFCs are relatively cheap and easy to perform.

1.5. Components of SOFCs:

The main components of SOFCs are cathode, anode, electrolyte and interconnect or separator as shown in Fig. 1.2. Each component of SOFC serves several functions and must meet specific requirements. Earlier, the most common materials used for SOFCs are YSZ as electrolyte, nickel/stabilized zirconia cermet for anodes, doped lanthanum magnetite for cathodes and doped lanthanum chromites as interconnect.

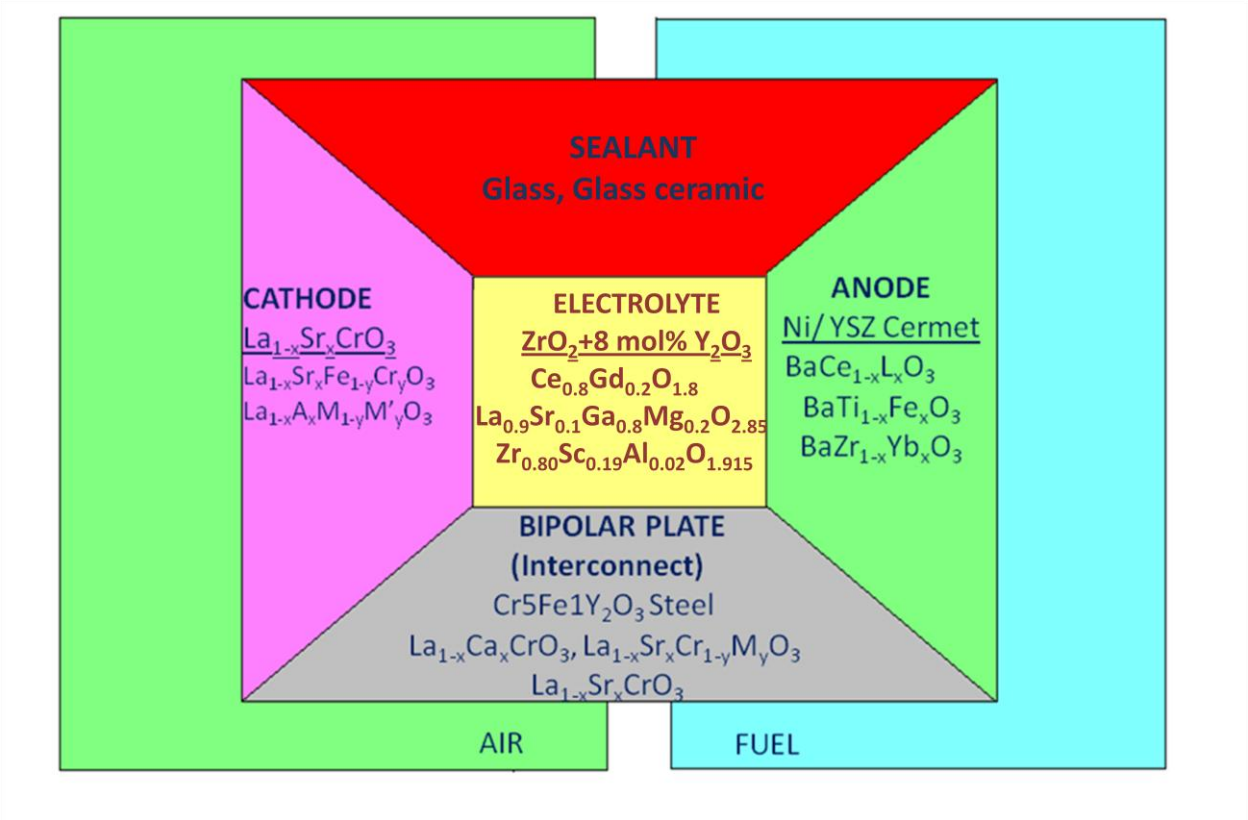

Fig. 1.2: Various components of SOFC.

The most important component among this is an electrolyte which is an ionic conductor separating cathode and anode. The properties of electrolytes mainly depend on its crystal structure, extent of doping and its chemical stability with other components of SOFC. Different categories of solid electrolytes used in SOFC applications are discussed in the next chapter. Since, the present work is based on systems containing perovskite (ABO_3) structure, so a brief introduction of ABO_3 is presented below.

1.6. Perovskite structure:

The crystal structure with general stoichiometry ABX_3 is called perovskite structure, where "A" and "B" are cations and "X" is an anion. In most of the perovskites, "X" is oxygen, "A" and "B" cations can have different charges. Here, we have considered the case where both A and B is trivalent cations and X is an oxide ion as shown in Fig. 1.3.

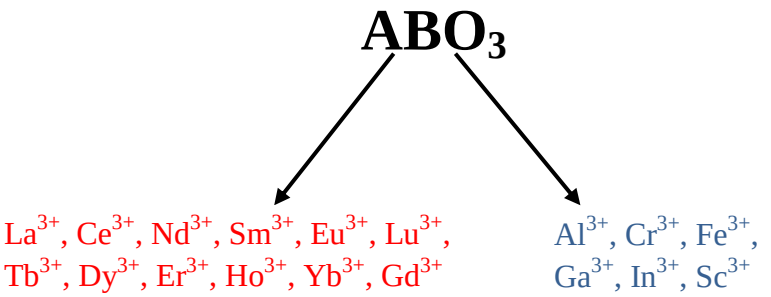

Fig. 1.3: Schematic representation of perovskite composition.

With these compositions, large number of perovskite oxides is currently recognized. Typical perovskite structures consist of larger cation at A-site which is 12-fold coordinated by oxygen and smaller cation at B-site with 6-fold coordinated oxygen. This structural family was originated from mineral $CaTiO_3$ which is named after Russian mineralogist, Count Lev Aleksevich von Perovski. $CaTiO_3$ exhibits orthorhombic structure with space group *Pnma*. Most of the ABO_3 compounds are crystallized in polymorphic structures, which show only a small distortion from the idealized perovskite structure [14]. The description of perfect perovskite structure was given by Cook and Sammell [10]. In cubic perovskite, each cation is the perfect spherical size to be in contact with an oxygen anion; the radii of the ions can be related as [10]:

$$R_A + R_O = \sqrt{2}(R_B + R_O) \qquad (1.7)$$

Where, R_A, R_B and R_O are the radii of cations at *A*-site, cation at *B*-site and oxide ion, respectively. However, with decreasing *A*-cation size, a point will be reached where the cations will be too small to remain in contact with the oxide ion in the cubic structure. Therefore, the *B-O-B* links bend slightly, tilting the BO_6 octahedral to bring some anions into contact with the *A* cations [9]. To allow for this distortion, a constant (*t*) is introduced into the above equation (1.7), thus:

$$R_A + R_O = t\sqrt{2}(R_B + R_O) \qquad (1.8)$$

Where, *t* is known as the Goldsmith tolerance factor. From geometric analysis, the ideal cubic structure should possess $t=1$. However, for cubic structure, the tolerance factor varies from 1.04 to 0.95 [15]. With the further decrease in *t*, the cubic symmetry gets disturbed and lower symmetric orthorhombic or rhombohedral phase than cubic is formed. It is further reported that the perovskite structures are stable only for $1.0<t<0.75$. Moreover, the perovskite lattice is more stable when *A*-site is twelve fold coordinated [16]. With the consideration of these factors, various perovskite types of solid electrolytes have been investigated so far [14, 17-

24]. The most successful among them is doped lanthanum gallates. The selective doping of lanthanum gallates on A- and B-site, the ionic conductivity as well as the chemical stability of these electrolytes can be tailored.

1.7. Factors influencing ionic motion:

Ionic conduction in solids takes place due to migration of ions through hopping mechanism via point defects such as vacancies in the crystal lattice. At ambient temperature, very little ion hopping takes place, since, the ions are at relatively low energy states. At the higher temperatures, the vacancies become mobile and certain ionic solids exhibit the phenomena known as fast ionic conduction.

There are many factors that affect the overall ionic conductivity of ionic conductors. These factors include ionic transport, negligible electronic conduction and thermodynamic stability of conducting phase over a wide range of temperature and oxygen partial pressure. In addition, they must possess negligible volatilities of components and negligible parasitic electronic conductivity [22].

The addition of suitable impurity to certain defect structures has a dramatic effect on overall conductivity. These extrinsic defects are the basis on which ionic conductivity of solid electrolytes has been tailored.

When an aliovalent-cation impurity is substituted to host cation, it could lead to formation of anion vacancies, which can be well represented by using Kronig-Vink notations. For example, when Sr^{2+} is doped on *A*-site of $LaGaO_3$ system, then to maintain the overall charge neutrality, formation of oxygen ion vacancy can be explained as follows:

$$2SrO \xrightarrow{La_2O_3} 2Sr'_{La} + V_o^{\bullet\bullet} + 2O_o^{\times} \qquad (1.9)$$

Where, Sr'_{La} means *Sr* in *La* site with the apparent unit negative charge (denoted by symbol ′) and $V_o^{\bullet\bullet}$ is the vacancy in the oxygen site with double positive charge. $O_o^{\times}$ means the lattice oxygen with mean charge zero. These oxygen vacancies so formed enhances the overall ionic conductivity of $LaGaO_3$ systems.

1.7.1. Importance of operating temperature:

Solid electrolytes make use of ion-flow mechanism for the conduction which exists at the higher temperatures. In comparison to liquid electrolytes, the higher activation energy is required for solid electrolytes, thus leads to Joule loss. This limitation corresponds to a high-temperature operation of solid electrolytes for SOFCs. However, this condition imposes some

merits as well as demerits for SOFC operation. In SOFCs, the temperature for reforming process is less than its operating temperature, which leads to higher efficiency of these cells. In addition, SOFCs do not require expensive metals like Pt for catalytic reduction of fuel; hence its cost is reduced. Moreover, SOFCs are suitable for hybrid systems with gas turbines, and they further increase the efficiency by post combustion of remaining fuels.

Besides these merits, higher operating temperature exhibits serious limitations. Higher temperature can create the thermal mismatch with other SOFC components, increase thermal reactivity and decrease components lifetime [9].

Due to these limitations, researchers are more focusing on such materials, which can operate at inter-mediate temperature range (400-600 °C) to make them cost effective without reducing their efficiency [14, 25-28].

1.7.2. Electrolytes used in intermediate temperature-solid oxide fuel cell (IT-SOFC):

During last decades, many noble electrolytes have been investigated for their use in IT-SOFCs. The most popular electrolyte for SOFC applications is yttria stabilized zirconia (YSZ). It has high ionic conductivity at 1000 °C and excellent phase stability, almost pure oxide ionic conductivity at wide oxygen partial pressure, good compatibility with other components of SOFC at operating temperature range. The major limitation of YSZ is its sharp decrease in conductivity at temperature below 800 °C. One way to solve this problem is to make thin electrolyte. A shorter path of oxygen ions will allow thin film YSZ electrolyte to have less ohmic resistance at IT-range. Various efforts have been made to synthesize thin film YSZ to improve its electrolyte properties at IT-range [26]. Further, anode supported thin film YSZ has considerably improved the conductivity at 800 °C. The most common electrolyte system in intermediate temperature range is perovskite based oxide ion conductors. Ishihara *et al.* [14] reported the use of Sr and Mg-doped lanthanum gallate (LSGM) as a solid electrolyte in IT-SOFCs. The ionic conductivity of LSGM is higher than YSZ and comparable to gadolinium doped ceria (CGO). Moreover, LSGM does not contain the easily reducible ions such as Ce^{4+}, and thus is superior to CGO for use in low oxygen partial pressure [27]. Further, LSGM has the high ion transport number close to one at wide oxygen partial pressure, making it suitable as an electrolyte for IT-SOFCs [14]. Based on encouraging results of LSGM, other perovskites such as $LaMO_3$ (M=Al, Lu, Sc and In) have also been investigated for their use as electrolytes [29-32]. It is reported that $LaAlO_3$ with different type of dopants can work as a mixed ionic conductor at high oxygen partial pressure and as an ionic conductor at low oxygen partial pressure [28, 30]. Furthermore, Sr- and Mg-

doped $LaScO_3$ is a mixed conductor (p-type and ionic). Furthermore, $(La_{0.9}Sr_{0.1})MO_{3-\delta}$ (M=Sc, In, and Lu) (LSMs) type perovskites are predominantly protonic conductors. However, with increasing the size of B-site cation from Sc^{3+} to Lu^{3+}, there is a decrease in proton conductivity [29].

1.7.3. Microstructure and ionic conductivity:

Microstructural parameters such as pore concentration, pore size, pore location, phase assemblage, grain size and its distribution, concentration and location of impurities can all have a significant influence on the total conductivity. All these parameters are further dependent upon the synthesis process and sintering conditions employed to produce the ceramic.

In general, the role of microstructure is divided into bulk and grain boundary effects. These effects can be investigated by analyzing Nyquist's plots with frequency at different temperatures. The ideal Nyquist plot contains three semicircular regions, which indicate the contribution of bulk, grain boundary and electrode polarization [33]. Studies employing this technique have contributed largely to analyze the effect of microstructure upon ionic motion through electrolyte material.

The influence of grain size on ionic conductivity was initially reported for YSZ system [34-38]. It was found that the grain-boundary conductivity increases with increasing grain size from 0.3 to 4 μm and was constant for larger grain size. For the bulk volume, the ionic conductivity was almost independent of grain size [36]. This behavior was explained on the basis of brick-layer model [39], according to which, the segregation of Y^{3+} cations led to the formation of space charge layers and the depletion of oxygen vacancies around the grain boundaries. The decrease in grain size could lead to an increase in grain boundary density, which in turn increases the space-charge layers and leads to enhance the grain boundary resistivity. The similar effect has also been reported for doped ceria [40-42]. It was further reported that nanosized ceria exhibited electronic conductivity under conditions at which microcrystalline samples showed impurity controlled ionic conductivity [42]. For systems such as $(Bi_2O_3)_{0.75}(Dy_2O_3)_{0.25}$, the similar ionic conductivities have been observed for samples with grain size larger than 100 nm, whereas the ionic conductivities were found to decrease for the samples with grain size below 100 nm [40].

The extent and size of pores within the grain volume affects the overall ionic conductivity since pores act as resistive barriers to ionic motion. Therefore, the number and size of pores should be as less as possible to have minimum obstruction to the ionic flow. The lower

porosity results in higher density which is essential for the electrolyte material [41]. To achieve density > 95% of theoretical density, various techniques have been explored such as solid-state reaction method, co-precipitation, sol-gel, flame pyrolysis [41, 42]. Apart from density, phase purity is another important requirement while selecting any synthesis technique. So, it can be said that all these factors have to be taken into account to get better electrolyte material. From the fore said discussion, we can conclude that the significant experimentation is required to achieve better conductivity and stability of electrolyte for its use in IT-SOFCs.

References:

[1] P. Gadonneix, World energy issue monitor, World energy council, UK (2013).

[2] B. Liu, Y Zhang, J. Univ. Sci. Technol. B, 15 (2008) 84.

[3] R. Priddle, Redrawing the energy climate map, International energy agency (IEA), France, (2013).

[4] G.G. Scherer, Fuel cell types and their electrochemistry, Springer, New York (2013) 97-119.

[5] N.Q. Minh, T. Takahashi, Science and Technology of Ceramic Fuel Cells, Elsevier, New York (1995) 16.

[6] V. Ramani, Electrochem. Soc. Interface, 15 (2006) 41.

[7] C. Rayment, S. Sherwin, Introduction to fuel cell technology, Department of Aerospace and Mechanical Engineering, University of Notre Dame USA (2003).

[8] J. Jacobson, Chem. Mater., 22 (2010) 660.

[9] H. Yokokawa, N. Sakai, History of high temperature fuel cell development, Fuel cell handbook, Wiley, USA (2003) 217.

[10] R.L. Cook, A. F. Sammells, Solid State Ionics, 45 (1991) 311.

[11] http://www.netl.doe.gov/technologies/coalpower/fuelcells/seca/primer/cell.html.

[12] H.W. Lee,H.Y. Jung, J.W. Jung, J.W. Son, J. Kim, J.H. Lee, in: M. Singh, H.T. Lin (Eds.), Development of SOFC Stack at Kist Using 10 × 10 cm^2 Anode Supported Cells, in Developments and Applications of Advanced Engineering Ceramics and Composites: Ceramic Transactions Series, John Wiley & Sons, Inc., Hoboken, NJ, USA. 192 (2006).

[13] S. J. Visco, C.P. Jacobson, L.C. De Jonghe, in**:** S.C. Singhal, M. Dokiya (Eds.), Proceedings of the Sixth International Symposium on Solid Oxide Fuel Cells, PV 99-19, Electrochem. Soc. Pennington, NJ, USA 861 (1999).

[14] T. Ishihara, H. Matsuda, Y. Takita, J. Am. Chem. Soc., 116 (1994) 3801.

[15] P. Huang, A. Petric, J. Electrochem. Soc., 143 (1996) 1644.

[16] S. Kim, M.C. Chun, K.T. Lee, H.L. Lee, J. Power Sources, 93 (2001) 279.

[17] M. Lindera, T. Hockera, L. Holzera, K. A. Friedrichb, B. Iwanschitzc, A. Maic, J. A. Schuler, J. Power Sources, 243 (2013) 508.

[18] B. Vaidhyanathan, A.P. Singh, D.K. Agrawal, T.R. Shrout, R. Roy, S. Ganguly, J. Am. Ceram. Soc., 84 (2001) 1197.

[19] P. Datta, P. Majewski, F. Aldinger, J. Alloys Compds., 438 (2007) 232.

[20] J.W. Fergus, R. Hui, X. Li, D.P. Wilkinson, J. Jhang, Solid oxide fuel cells, Materials properties and performance, CRC press, Taylor & Francis Group, USA (2009).

[21] H. Inaba, H. Hayashi, M. Suzuki, Solid State Ionics, 144 (2001) 99.

[22] P.S. Anderson, G.C. Mather, F.M.B. Marques, D.C. Sinclair, A.R. West, J. Eur. Ceram. Soc., 19 (1999) 1665.

[23] E.J. L. Schouler, N. Mesbahi, G.Vitter, Solid State Ionics, 9&10 (1983) 989.

[24] S.H. Chu, M.A. Seutx, J. Solid State Chem., 23 (1978) 297.

[25] B. Zhu, J. Power Sources, 93 (2001) 82.

[26] E. Courtin, P. Boy, T. Piquero, J. Vulliet, N. Poirot, C. L. Robert, J. Power Sources, 206 (2012) 77.

[27] J. W. Fergus, J. Power Sources, 162 (2006) 30.

[28] J.A. Kilner, R.J. Brook, Solid State Ionics, 6 (1982) 237.

[29] K. Nomura, T. Takeuchi, H. Kageyama, Y. Miyazaki, Solid State Ionics, 162 (2003) 99.

[30] D. Lybye, F.W. Poulsen, M. Mogensen, Solid State Ionics, 128 (2000) 91.

[31] E.R. Trejo, G. Tavizon, A.A. Landeros, J. Phys. Chem. Solids, 64 (2003) 515.

[32] H. He, X. Huang, L. Chen, Solid State Ionics, 130 (2000) 183.

[33] M.J. Verkerk, B.J. Middelhuis, A.J. Burggraaf, Solid State Ionics, 6 (1982) 159.

[34] M. Miyayama, H. Yanagida, J. Am. Chem. Soc., 67 (1984) 194.

[35] M. Aoki, Y.M. Chiang, I. Kosachi, J.R. Lee, H. Tuller, Y. Liu, J. Am. Chem. Soc., 79 (1996) 1169.

[36] X. Guo, Solid State Ionics, 81 (1995) 235.

[37] C. Tian, S.W. Chan, Solid State Ionics, 134 (2000) 89.

[38] G.B. Jung, T.J. Huang, J. Mater. Sci., 38 (2003) 2461.

[39] A. Tschope, E. Sommer, R. Birringer, Solid State Ionics, 139 (2001) 255.

[40] R. Li, Q. Zhen, M. Drache, A. Rubbens, C. Estournes, R. N. Vannier, Solid State Ionics, 198 (2011) 6.

[41] D. Ganguli, M. Chatterjee, Ceramic powder preparation: A handbook, Kluwer Academic Publishers, Boston (1997) 35.

[42] F.F. Lange, B.I. Davis, H.C. Graham, J. Am. Ceram. Soc., 66 (1983) 98.

Chapter II

LITERATURE REVIEW

Overview

The purpose of this chapter is to highlight some of the key developments in the area of oxide ion conductors, which can be used as a solid electrolyte for SOFC applications. Oxide ion conductors are the important class of materials that can be used in many technological applications such as oxygen sensors, SOFCs and gas separation membranes. In terms of clean energy devices, SOFCs are important and well known system because of high efficiency and ability to act as a bridging technology between hydrocarbon and hydrogen fuel system. One of the important components of SOFC is the electrolyte. An ideal solid electrolyte should be ionic conductor and an electronic insulator. The most common electrolyte for SOFCs in use is YSZ. However, the ionic conductivity of YSZ reduces abruptly below 800 °C. So, alternative electrolytes have been investigated for the intermediate temperature SOFCs. In IT-SOFCs, the most common electrolyte in use is doped lanthanum gallate. The selective doping of $LaGaO_3$ could lead to the better electrolytic properties that can be used as an electrolyte in IT-SOFCs. Furthermore, the thermal expansion coefficient, chemical stability at different atmospheres, structure and optical properties can be enhanced by selective doping. In addition to oxide ion conducting materials, proton conducting oxides are also discussed as electrolytes in fuel cells. These proton conducting electrolytes have the potential to lower the operating temperature for SOFC, thereby significantly lowering the cost of SOFCs.

2.1. Background:

Advancement made in high-temperature electrochemical cells with oxide ion conducting electrolytes has led to development of efficient and comparable SOFCs having longer life. These are considered as alternative power generation sources, which offer a clean and pollution-free technology through electrochemical reaction to generate electricity with high efficiency (~85 %), thus bypassing the Carnot cycle [1-5]. These fuel cells provide many advantages over traditional energy conversion systems, including high efficiency, reliability, modularity, fuel adaptability and very low level of NO_x and SO_x emissions [6].

2.2. ZrO_2 based electrolytes:

The operating temperature of SOFC is mainly dependent on the electrolyte used in the cell. ZrO_2 based electrolytes have been studied extensively. ZrO_2 exists in three polymorphic forms; below 1000 °C, it exists in monoclinic form, from 1200-2300 °C, it is tetragonal followed by cubic structure from 2300-2700 °C. The cubic structure is most favorable for ionic conduction [7]. In order to stabilize high conducting cubic phase at lower temperature, different dopants have been used. Among various dopants, 8 to 10 mol% yttria are most suitable to stabilize cubic phase of zirconia, which is the most common electrolyte used in SOFC [8]. It possesses unique combination of properties such as pure oxide ion conductivity, excellent chemical and thermal stability under oxidizing and reducing atmospheres. Due to this, YSZ is still most common among electrolyte materials in SOFC applications. Cologna *et al.* [9] investigated the synthesis of 8YSZ at much lower sintering temperature of 750 °C using flash-sintering process. The lower sintering temperature could be beneficial to achieve higher ionic conductivity and decrease the manufacturing cost of other components of SOFCs [9]. Ghatee *et al.* [10] reported the effect of 3YSZ addition over 8YSZ on the electrical conductivity and grain size of the composite system. It was reported that the conductivity of the composite system was enhanced with increasing 3YSZ content up to temperature <550 °C but decreased at higher temperatures (T >550 °C). Further, the activation energy of the composite system was decreased with respect to 8YSZ. Moreover, the addition of 3YSZ on 8YSZ decreased the grain boundary contribution to total conductivity of the composite system [10]. Kumar *et al.* [11] investigated the effect of nanosize Al_2O_3 doping on 8YSZ. They reported that Al_2O_3 doping led to decrease in grain size and

increase in grain boundary area. The overall conductivity increased slightly by Al_2O_3 doping on 8YSZ system.

Shukla *et al.* [12] synthesized the nano-size YSZ with sol-gel process. The results indicated a remarkable reduction of activation energy for grain growth from 580 kJ/mol (for micron sized YSZ) to 13 kJ/mol for nano 3YSZ. Recently, nano-scale thin film of YSZ was synthesized using the atomic layer deposition (ALD) technique [13]. Thin film of 8YSZ on amorphous Si_3N_4 having polycrystalline nature with fine spherical grains were reported. Moreover, the power density of 270 mW/cm^2 was obtained between 265- 350 °C. Geiger and Parker [14] synthesized nano-sized YSZ of high purity using electrospray-based flame synthesis process. Miller *et al.* [15] have compared the effect of dopant clustering in YSZ and Scandia stabilized zirconia (SSZ) with respect to the ionic conductivity and stability of the cubic phase. The effect of clustering in YSZ and SSZ results in the trapping of vacancies causing a stable ordering process to occur. Also, their results indicated that yttria was a poorer stabilizer than scandia under similar conditions of doping and clustering. Further, mutual repulsion of dopant ions in case of Y^{3+} was stronger than Sc^{3+}, which led to slower clustering in YSZ than SSZ.

2.3. Bi_2O_3 based electrolytes:

Another potential candidate to be used as the solid electrolyte in SOFC applications is doped bismuth oxide. The high oxide ion conductivity of solid solutions of Bi_2O_3 was initially reported by Takahashi and co-workers [16]. Bi_2O_3 possesses four polymorphic forms in which fluorite related δ-phase (fcc) exists between 729 to 825 °C. Below 729 °C, the δ-phase transforms to the low temperature monoclinic α-phase. However, during cooling, it exists in two intermediate phases viz. the tetragonal β-phase at 750 °C and the body centered cubic γ-phase at 639 °C. Takahashi *et al.* [16] were the first to report that the face centered cubic (fcc) phase of Bi_2O_3 can be stabilized by various aliovalent metal ions doping which exhibit highest ionic conductivity among all oxide ion conductors known so far [16, 17]. Unfortunately, Bi_2O_3 based materials possess a number of disadvantages such as thermodynamic instability under reducing atmosphere, volatilization of bismuth oxide at moderate temperatures, a high corrosion activity and low mechanical strength [3]. Hence, the use of these oxides in SOFCs is limited.

The stabilization of high conducting δ-Bi_2O_3 phase to lower temperature can be achieved by selective doping of bismuth oxide with rare-earth and higher valency cations (such as Y, Dy, Sn,

Ti, W or Er) [3, 18-20]. The selective doping of Bi_2O_3 with Dy_2O_3 and WO_3 exhibited 1.5 times higher ionic conductivity (0.57 S/cm at 500 °C) as compared to 20 mol % Er doped Bi_2O_3 [20]. In addition, the double doping (W and Dy) on Bi_2O_3 leads to non-linear ionic conductivity. The highest ionic conductivity was found for materials containing minimum dopant required for the stabilization of desired phase [3]. Further doping leads to a decrease in oxygen ion conductivity due to decrease in unit cell volume and increase in average strength of cation-anion bonds. Moreover, the binary and ternary solid solutions lead to the formation of disordered fluorite structure and undergo a slow phase transformation and decrease in conductivity with time.

In addition to this, solid solutions based on γ-$Bi_4V_2O_{11}$ have been widely investigated [21-25]. The crystal structure of γ-$Bi_4V_2O_{11}$ is based on the Aurivillius structure, which consists of alternating $Bi_2O_2^{2+}$ and perovskite type $VO_{3.5}^{2-}$ layers, with the formation of intrinsic oxygen vacancies [3]. Kant *et al.* [21] reported that $Bi_4V_{2-x}Cu_xO_{11-\delta}$, $Bi_4V_{2-x}Mn_xO_{11-\delta}$, $Bi_4V_{2-x}Ti_xO_{11-\delta}$ and $Bi_4V_{2-x}Al_xO_{11-\delta}$ systems stabilized γ-phase for $\times \leq 0.2$. According to them, the conductivity of undoped $Bi_4V_2O_{11}$ was observed to be 1.12×10^{-6} S/cm at 300 °C. The highest conducting $Bi_4V_{2-x}Ti_xO_{11-\delta}$ system follows the conductivity order as $\sigma_{0.4}>\sigma_{0.3}>\sigma_{0.2}>\sigma_{0.1}$ in terms of composition and $\sigma_{800°C}>\sigma_{825°C}>\sigma_{775°C}>\sigma_{750°C}$ in terms of sintering temperature.

Li *et al.* [26] investigated the effect of nano to micro grain-size on ionic conductivity of $(Bi_2O_3)_{0.75}(Dy_2O_3)_{0.25}$. The total ionic conductivity was not affected by grain size down to 100 nm. However, conductivity decreased when the grain size was reduced to 20 nm. Kuo *et al.* [18] investigated the synthesis of Ti_2O_3 doped bismuth oxide ($Bi_{12}TiO_{20}$) using colloid processing pressure filtration method sintered in the temperature range 775-850 °C. The $Bi_{12}TiO_{20}$ compound was reported to be stable material at operating range of 550-775 °C without undergoing any phase transition.

Despite the high ionic conductivity of bismuth based materials, the practical use of these materials is limited due to their narrow operating temperature range, high chemical reactivity [3, 17] and low mechanical strength [27, 28].

2.4. CeO_2 based electrolytes:

Another important material which has been widely investigated for its use as a solid electrolyte for SOFC application is the doped ceria system. The electrical conductivity of gadolinia-stabilized ceria is about one order of magnitude higher than that of YSZ and it is about 0.1 S/cm

at 800 °C [29]. The pure CeO_2 is a mixed (ionic and electronic) conductor with almost same partial conductivities of oxygen ion, electron and hole. The corresponding activation energies were 2.57, 1.15 and 0.63 eV (at 600–1000°C, $1<Po_2<10^{-4}$ atm) [30]. The ionic conductivity of ceria can be increased significantly by doping with alkaline earth metals such as MgO, CaO, SrO and BaO. The doping of CaO and SrO increases the overall ionic conductivity and lowers the activation energy of ceria as reported by Inaba *et al.* [29], whereas, the doping of BaO and MgO do not increase the electrical conductivity in comparison to CaO and SrO. Furthermore, the effect of doping of rare earth oxides in ceria on electrical conductivity has been investigated by many researchers [31-34]. Yahiro *et al.* [31] investigated the electrical conductivity of Sm_2O_3, Gd_2O_3 and Y_2O_3 doped CeO_2 where 10 mol% Sm doping on CeO_2 possessed higher electrical conductivity among ceria based oxides. Kuharuangrong [34] further reported the similar results for Sm, Gd, Dy and Er dopants. The doping of Sm^{3+} ions among rare earth oxides and Ca^{2+} ions among alkaline-earth oxides with an ionic radius of 1.1Å reported the maximum electrical conductivity due to the similar ionic radius with host cation. It further led to minimize the association enthalpy between dopant ion and oxygen vacancy which in turn give minimum activation energy for conductivity process. However, the major limitation of ceria based electrolytes is that they get reduced to give electronic conduction under reducing atmospheres and thus less suitable as solid electrolytes for SOFC applications.

The composite electrolytes based on ceria have also been investigated to get better applicability as solid electrolytes in IT-SOFCs [35-38]. Baek *et al.* [35] investigated the composite of nano-structured neodymium doped ceria and 38 wt % $(Li\text{-}0.5Na)_2CO_3$ with overall conductivity of 0.1 S/cm at 600 °C. Choi *et al.* [36] recently reported the ionic conductivity data of twenty four compounds of differently doped-ceria systems. Among these doped systems, Nd doped ceria possessed highest ionic conductivity in air at 600 °C.

2.5. Pyrochlore based electrolytes:

Another category of ionic conducting material that can be used as a solid electrolyte in SOFCs is pyrochlore. The chemical formula of pyrochlore is $A_2B_2O_6O'$or $A_2B_2O_7$ where the A-site cation, which is larger rare earth alkali metal, or post-transition metal cation that lies in a distorted (6O+2O′) coordination, while the B-site cation, which is a smaller transition metal cation, forms a slightly distorted BO_6 octahedron [39]. The pyrochlore structure is a super structure derivative

of the simple fluorite structure ($AO_2 = A_4O_8$, where the A and B cations are ordered along the <110> direction. The additional anion vacancy resides in the tetrahedral interstice between adjacent B-site cations. This intrinsic anionic vacancy is responsible for high oxygen ion conduction in pyrochlore system. Moreover, the substitution of larger B′ ion in solid solution for B can lead to disorder in pyrochlore structure such as in $Y_2(Zr_yTi_{1-y})O_7$. The oxide ion conductivity for this system was 10^{-2} S/cm at 1000 °C, slightly less than doped zirconia systems [40]. Wilde and Catlow [41] investigated the defects and oxide-ion diffusion mechanism of $A_2B_2O_7$ (for A is Gd or Y and B is Zr and Ti). They found that pyrochlore structured compounds with higher zirconium contents had higher oxygen ion conductivity than those with lower zirconium and titanium contents, although, lesser migration energies of oxide-ion conductions were obtained in titanates as compared to zirconates. Also, the controlling factor in the ionic conductivity is the energy of formation of the anion defects, necessary for the formation of vacancy hopping mechanism. In addition, lesser degree of anionic disorder was obtained for the titanate as compared to the ziconates which was comparable with the higher energies for the formation of isolated Frenkel defects in the titanate materials [41]. Omata *et al.* [42] reported the proton conductivity behavior of Ca^{2+} doped $La_2Zr_2O_7$ pyrochlore system at temperatures above 800 °C. The changes in lattice parameters with Ca^{2+} ion doping at La-site, the Zr-site in $La_2Zr_2O_{7-\delta}$ indicated the solid solution formation in this pyrochlore system. Pizada *et al.* [43] investigated the effect of cation radii, which influences the activation energies for oxygen migration of pyrochlore structures. They suggested that in $A_2B_2O_7$ compounds with B^{4+} cation radii of intermediate or larger size (i.e. Pb, Zr, Sn and even Mo) exhibit the lowest migration activation energies for oxygen migration. However, the dependence on *A*-cation radius was less pronounced for oxygen migration energies. Liu *et al.* [44] reported the structural and electrical studies of $Sm_{2-x}La_xZr_2O_7$ ($0 \leq x \leq 1.0$) series. The investigated series is mainly oxide ion conductor at 1.0×10^{-4} to 1.0 atmosphere pressure exhibiting highest ionic conductivity of 5.94×10^{-3} S/cm for the $Sm_2Zr_2O_7$ at 900 °C. Moreover, the electrical conductivity of $Sm_{2-x}La_xZr_2O_7$ gradually decreased with increasing lanthanum content at identical temperature levels. Liu *et al.* [45] investigated the oxide ion conductivity of $Gd_{1-x}Eu_{2x}Sm_{1-x}Zr_2O_7$ pyrochlore system. The highest ionic conductivity for this system was 1.01×10^{-2} S/cm at 900 °C in air. Xia *et al.* [46] further reported the effect of Gd and Dy co-doping on the structural and electrical properties of $Sm_2Zr_2O_7$ system. The $SmDy_{1-x}Gd_xZr_2O_7$ ceramics (x=0.2, 0.4, 0.6, 0.8, 1.0) exhibit a pyrochlore

structure except for $SmDyZr_2O_7$ ceramic which possessed defective-fluorite structure. The substitution of Gd^{3+} facilitated the structural change from defective fluorite to pyrochlore structure. Moreover, all the samples possessed pure oxide ion conductivity and with increasing Gd^{3+} content in $SmDy_{1-x}Gd_xZr_2O_7$ systems, the grain conductivity of the system was increased. The highest grain conductivity reported was 1.9×10^{-2} S/cm in $SmGdZr_2O_7$ at 900 °C. Li-ion doping on $Y_2Ti_2O_7$ was reported by Wen *et al.* [47]. The highest ionic conductivity reported for $Y_{1.94}Li_{0.18}Ti_2O_7$ was 4.3×10^{-4} S/cm at 700 °C. Moreover, the additional Li_2O content could act as a self-flux which could lead to the higher density and grain size.

2.6. Perovskite based electrolytes:

Perovskite based materials have also attracted a wide attention for their role as solid electrolytes in IT- SOFCs. Typical perovskite lattice has chemical formula ABO_3 that consists of small B cations within oxygen octahedral (BO_6), and a larger A cation which are mainly 12-coordinated by oxygen. The structure of ideal cubic perovskite lattice is shown in Fig. 2.1, where A are shown at the corners of the cube, and the B cation is at the body centre with oxygen ions at the face-centered positions.

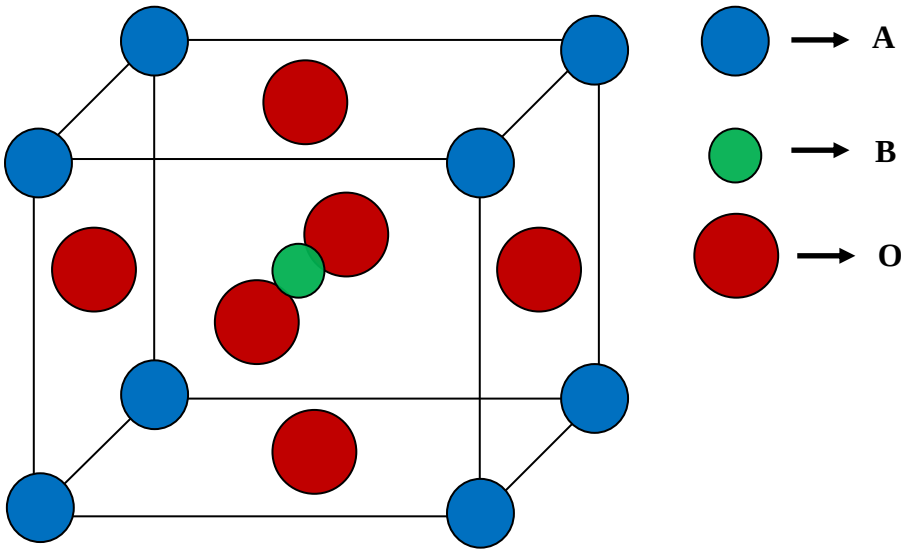

Fig. 2.1: Cubic perovskite unit cell. Blue spheres represent the A cations, green sphere represent the B cation, and red spheres represent oxygen anions forming an octahedra (BO_6).

Initially, Ishihara [48] and Feng [49] have reported high oxide ion conductivity in lanthanum gallate systems with composition $La_{1-x}Sr_xGa_{1-y}Mg_yO_{3-\delta}$ (LSGM). In early work, Ishihara *et al.*

[48] showed that the ionic conductivity of $La_{0.9}Sr_{0.1}Ga_{0.8}Mg_{0.2}O_3$ was higher than zirconia or ceria based electrolytes and slightly lower than Bi_2O_3 doped systems. Moreover, LSGM possessed pure oxide ion conductivity from 10^{-20} to 1 *atm* pressure.

The ionic conductivity for $La_{0.9}Sr_{0.1}Ga_{0.8}Mg_{0.2}O_{2.85}$ system was independently reported by Feng and Goodenough [49]. The observed conductivity was ~1×10^{-2} S/cm at 600 °C with a transport number ~ 1 over the same oxygen partial pressure (p_{O2}) range. They observed from Arrhenius behavior that the ionic conductivity deviates above 600 °C. The apparent activation energy below 600 °C is 1.07 eV, which is slightly larger than 0.98 eV of YSZ [49, 50]. Since then, there is considerable interest in the development of doped lanthanum gallate systems to get better electrolyte properties for SOFCs.

The crystal structure of $LaGaO_3$ and doped lanthanum gallate was investigated independently by various researchers [48-54]. Kajitani *et al.* [51] reported that Sr and Mg doping on $LaGaO_3$ systems significantly affected the symmetry of parent phase and increased the transition temperature. The parent phase ($LaGaO_3$) is orthorhombic (*Pbnm*) up to 150 °C and rhombohedral ($R\bar{3}c$) from 160 to 800 °C. However, in doped systems such as $LaGa_{0.9}Mg_{0.1}O_{2.95}$ crystallizes in orthorhombic (*Ibmm*) up to 340 °C and rhombohedral ($R\bar{3}c$) from 350 to 800 °C. On the other hand, $La_{0.9}Sr_{0.1}Ga_{0.9}Mg_{0.1}O_{2.9}$ exhibited monoclinic structure (I2/a) up to 400 °C and rhombohedral ($R\bar{3}c$) from 410 to 800 °C. Moreover, doping causes the reduction of GaO_6 octahedral tilt in $La_{0.9}Sr_{0.1}Ga_{0.9}Mg_{0.1}O_{2.9}$, which is responsible to enhance the overall ionic conductivity of LSGM system. Similar results on phase transitions with doped lanthanum gallate have also been reported by Rozumek *et al.* [52]. They reported that variation in dopant concentration leads to phase transitions from orthorhombic (*Pbnm*) to rhombohedral ($R\bar{3}c$) in $La_{0.825}Sr_{0.175}Ga_{0.825}Mg_{0.175}O_{2.825}$. The cubic phase ($Pm\bar{3}m$) is observed for the composition $La_{0.8}Sr_{0.2}Ga_{0.8}Mg_{0.2}O_{2.8}$. At 500 °C in air and at constant Sr-and Mg-content, a phase transformation from orthorhombic (*Pbnm*) to cubic ($Pm\bar{3}m$) was observed. Moreover, for the orthorhombic transformations, thermal expansion coefficient were $\alpha_{a,ortho}$ = 10.81 $\times10^{-6}$ °C^{-1}, $\alpha_{b,ortho}$ = 9.77 $\times10^{-6}$ °C^{-1}, $\alpha_{c,ortho}$ = 9.83 $\times10^{-6}$ °C^{-1} in the temperature range 25-400 °C, and for the cubic phase, the TEC (α_{cubic}) was ~ 13.67 $\times10^{-6}$ °C^{-1} (500-1000 °C).

Matraszek *et al.* [53] investigated the solid solubility limit for LSGM system and reported the solubility of Sr in $La_{1-x}Sr_xGa_{1-y}Mg_yO_{3-(x+y)/2}$ perovskite phase up to about 20 mol% if Mg and Sr

are added simultaneously. Datta *et al.* [54] investigated the thermal expansion behavior of Sr and Mg doped lanthanum gallate from room temperature to 1000 °C. The TEC values were higher when Mg substituted Ga. Moreover, the transition temperature was observed ~ 148 °C from orthorhombic to rhombohedral phase. At a given Sr-content, varying the amount of Mg-content increased the phase transformation temperature. On the other hand, the phase transition temperature decreased with the increase of Sr-content. The abnormality of transition temperature for orthorhombic to rhombohedral phase becomes broadened with the increase of Mg-content. The increased value of TEC with doping was interpreted as the weakening of the binding energy because of creation of oxygen vacancies.

Kim *et al.* [55] reported the Ba-and Mg-doping on the lanthanum gallate system. The non-linear conductivity behavior of Ba-doped lanthanum gallate system was related to dopant-cation vacancy association. This vacancy-dopant association was responsible for increased activation energy in the low-temperature region. Vaporization process of Ga from doped $LaGaO_3$ has been reported by Yamaji *et al.* [56]. At the higher temperatures in reducing atmosphere, substitution in $LaGaO_3$ electrolytes, especially by Sr for La-site, changed the vaporization process of Ga and caused the Ga depletion from the lanthanum gallate system. So, operating temperature and controlled atmosphere is playing an important role for doped lanthanum gallate to be used as a solid electrolyte. Moreover, lanthanum based perovskites including $LaScO_3$, $LaInO_3$, $LaYO_3$ and $LaAlO_3$ based materials are also used as oxygen ion conductors and find their application as electrolyte material for SOFC [57]. Sinha *et al.* [58] studied undoped and Ca-doped $GdAlO_3$ systems. These systems exhibited good sinterability leading to high experimental density. Kakinuma *et al.* [59] studied the behavior of SOFC in which $Ba_{0.3}Sr_{0.2}La_{0.5}InO_{2.75}$ was used as an electrolyte material and power density found to be maximum at 800 °C. He *et al.* [60] have reported the electrical conductivity (7.6×10^{-3} S/cm^{-1}) at 900 °C in $La_{0.9}Sr_{0.1}InO_{3-\delta}$ system. In this system, p-type and n-type conduction behavior are reported at high and low oxygen partial pressure, respectively. At intermediate oxygen partial pressure, the conductivity is mainly due to oxide-ion conduction. TEC and structural phase transitions of $LaMO_3$ and $La_{0.9}Sr_{0.1}MO_{3-\delta}$ with different B-site cations are reported by Inaba *et al.* [61]. The transition temperature from orthorhombic to rhombohedral structure of $LaGaO_3$ rises with Mg doping, but it did not change significantly in the case of Sr-doping. TEC of $LaScO_3$, $LaInO_3$ and $LaAlO_3$ showed no thermal expansion anomaly from orthorhombic to rhombohedral structure. Transition temperature from

orthorhombic to rhombohedral structure for $LaMO_3$ and $La_{0.9}Sr_{0.1}MO_{3-\delta}$ with different size of B-site ions decreased linearly with the tolerance factor (*t*), which is defined in equation (1.8). It indicated that the perovskite with a small tolerance factor is distorted, resulting in the higher transition temperature. Electrical conduction behavior of $La_{0.9}Sr_{0.1}MO_{3-\delta}$ (with B=Al, Ga, In and Lu) as a function of crystalline free volume has been investigated by Nomura *et al.* [62]. These compounds exhibited almost similar pre-exponential factor, $A \sim 10^5$ S/cm from 730 to 980°C in N_2. Moreover, the calculated values of activation energy in this range indicated that the conduction mechanism in these systems is mainly ionic. The Ga in B-site possessed maximum free volume ~13$Å^3$, so is most suitable for oxide ion conduction among studied systems. High-temperature crystallographic study of $La_{0.9}Sr_{0.1}MO_{3-\delta}$ (M=Sc, In and Lu) indicated these systems as predominantly protonic conductors [63]. All these systems possess an orthorhombic structure with the space group *Pnma*. For the Sc-compound, the oxygen–oxygen (O–O) bond lengths of intra-ScO_6 octahedra were shorter than those of inter-ScO_6 octahedra, suggesting the predominant three-dimensional (3D) proton conduction along the edges of ScO_6-octahedra. On increasing the size of B-site cation from Sc^{3+} to Lu^{3+}, the O–O bond lengths and tilting angles of $BO_6(M^{3+}O_6)$ octahedra increased. For Lu-compound, the O–O bond lengths of intra-LuO_6 octahedra were almost same as those of inter-LuO_6 ones, indicating the predominant one-dimensional (1D) proton conduction along O1–O1 and O2–O2 sites on the vertices of BO_6 octahedra. This change in proton conduction pathway from 3D to 1D resulted in the lowering of proton mobility, hence lower proton conductivity. Point defects and ion migration in $LaInO_3$ using atomic simulation method are reported by Trejo *et al.* [64]. This system ($LaInO_3$) exhibited a very limited amount of Schottky defects and doping of aliovalent impurity is helpful to increase the conductivity of the system. Moreover, the estimation of the energy of water solution in the lattice points toward the absorption of water for $LaInO_3$ was reported. The presence of *In* may cause an increase in basicity in the lattice and therefore could lead to the protonic conductivity in the system. Kimpton *et al.* [5] have predicted the microstructural and electrical conduction behavior in In_2O_3 substituted LSGM system. The In^{3+} replaced the Ga^{3+} and Mg^{2+} ion which had the detrimental effect on the conductivity of doped-LSGM system. Moreover, secondary phases such as $LaInO_3$ and $LaSrGaO_4$ were also formed which interfere with the formation of homogenous single phase compact. Yao *et al.* [65] have further reported the interrelationship between crystal symmetry and ionic conductivity in doped lanthanum gallate

system. They revealed rhombohedral structure in $La_{0.9}Sr_{0.1}Ga_{0.9}Mg_{0.1}O_{2.9}$ (LSGM1010) and $LaGa_{0.8}Mg_{0.2}O_{2.9}$ (LGM20) while detected orthorhombic symmetry in $La_{0.8}Sr_{0.2}GaO_{2.9}$ (LSG20). Also, the electrical conductivity of LSGM1010 and LGM20 was similar but higher than that of LSG20. Similar reports on crystal structure and phase transition behavior of LSGM are also reported by Shibasaki *et al.* [66]. For A-site dopant, Sr^{2+}, formation of secondary phases limit the solid solubility upto $\times$=0.05 in $La_{1-x}Sr_xGaO_{3-\delta}$ system. Also, $LaGa_{1-y}Mg_yO_{3-\delta}$ with $0 \leq y \leq 0.2$ could be prepared as a single phase, although Bravais lattice varied from primitive orthorhombic to a body-centered one with substitution of y=0.1 Mg. Partial substitution of Sr at La-site in $LaGa_{1-y}Mg_yO_{3-\delta}$, where y=0.15 and y=0.20 was possible with solid solution limit of 0.10 and 0.20, respectively. Moreover, the crystal system changed from orthorhombic to cubic at Sr content of $\times$=0.15 in $La_{1-x}Sr_xGa_{0.8}Mg_{0.2}O_{3-\delta}$. Also, the structural phase transition from orthorhombic to rhombohedral phase observed in $La_{1-x}Sr_xGa_{1-y}Mg_yO_{3-(x+y/2)}$ was found to increase with Sr and Mg content.

As discussed above, many researchers have reported the structural and electrical conductivity of unsubstituted and substituted lanthanum gallate. However, the systematic study on uniform substitution at A-site of $LaGaO_3$ has not been done. Moreover, the effect of substitution of alkaline earth metals at La-site on the structure and thermal stability is very important to explore the possibilities of better electrolyte system which can operate at intermediate temperature range.

In the periodic table, indium and gallium are lying in the same group, where indium lies just below gallium. There are some reports in the literature that substituted lanthanum indate can be used as solid electrolyte in SOFC applications [60-62]. But, the detailed study on this system is still lacking. Moreover, thermal stability of these systems is still lacking which is very important for materials to be used as solid electrolyte in SOFCs.

Considering these facts, in the present work, it is planned to develop substituted lanthanum gallate and lanthanum indates with the following objectives:

- To synthesize $La_{1-x}M_xInO_3$ and $La_{1-x}M_xGaO_3$ where lanthanum can be doped/substituted with M=Sr, Ca, Ba .
- These components so synthesized have been characterized employing various techniques such as X-ray diffraction (XRD), Thermal analysis (TGA), Scanning electron microscopy (SEM), Energy dispersive spectroscopy (EDS) and ac impedance spectroscopy (IS).

In order to achieve above mentioned objectives, the different samples were synthesized and characterized by different techniques. The details of the synthesis, characterization techniques and their mechanism are given in the next chapter.

References:

[1] E. Kendrick, M.S. Islam and P.R. Slater, J. Mater. Chem., 17 (2007) 3104.

[2] J.B. Goodenough, Solid State Ionics, 94 (1997) 17.

[3] V.V. Kharton, F.M.B. Marques, A. Atkinson, Solid State Ionics, 174 (2004) 135.

[4] O. Yamamoto, Electrochim. Acta, 45 (2000) 2423.

[5] J.A. Kimpton, Conductivity and Microstructural Characterisation of Doped Zirconia-Ceria and Lanthanum Gallate Electrolytes for the Intermediate-Temperature, Solid Oxide Fuel Cell, Ph.D Thesis, School of Engineering and Science, Swinburne University of Technology, Melbourne, Australia (2000).

[6] S.C. Singhal, Solid State Ionics, 135 (2000) 305.

[7] J.P. Golf, W. Hayes, S. Hull, M.T. Hutchings, K.N. Clausen, Phys. Rev. B, 59 (1999) 14202.

[8] T.H. Etsell, S.N. Flengas, Chem. Rev., 70 (1970) 339.

[9] M. Cologna, A.L.G. Prette, R. Raj, J. Am. Ceram. Soc., 94 (2011) 316.

[10] M. Ghatee, M.H. Shariat, J.T.S. Irvine, Solid State Ionics, 180 (2009) 57.

[11] B. Kumar, C. Chen, C. Varanasi, J.P. Fellner, J. Power Sources, 140 (2005) 12.

[12] S. Shukla, S. Seal, R. Vij, S. Bandyopadhyay, Nano Letters, 3 (2003) 397.

[13] J.H. Shim, C.C. Chao, H. Huang, F.B. Prinz, Chem. Mater., 19 (2007) 3850.

[14] M. Geier, T. Parker, Ind. Eng. Chem. Res., 52 (2013) 16842.

[15] S.P. Miller, B.I. Dunlap, A.S. Fleischer, Solid State Ionics, 253 (2013) 130.

[16] T. Takahashi, H. Iwahara, Y. Nagai, J. Appl. Electrothem., 2 (1972) 97.

[17] P. Shuk, H.D. Wiemhofer, U. Guth, W. Gopel, M. Greenblatt, Solid State Ionics, 89 (1996) 179.

[18] Y.L. Kuo, L.D. Liu, S.E. Lin, C.H. Chou, W.C. J. Wei, J. Eur. Ceram. Soc., 31 (2011) 3119.

[19] T.C. Kuo, Y.L. Kuo, W.C. J. Wei, J. Eur. Ceram. Soc., 31 (2011) 3153.

[20] N. Jiang, E.D. Wachsman, S.H. Jung, Solid State Ionics, 150 (2002) 347.

[21] R. Kant, K. Singh, O.P. Pandey, Int. J. Hydrogen Energy, 33 (2008) 455.

[22] A.A. Yaremchenko, V.V. Kharton, E.N. Naumovich, F.M.B. Marques, J. Electroceram., 4 (2000) 235.

[23] A. Watanabe, K. Das, J. Solid State Chem., 163 (2002) 224.

[24] R.N. Vannier, R.J. Chater, S.J. Skinner, J.A. Kilner, G. Mairesse, Solid State Ionics, 160 (2003) 327.

[25] V.N. Tikhonovich, E.N. Naumovich, V.V. Kharton, A.A. Yaremchenko, A.V. Kovalevsky, A.A. Vecher, Electrochim. Acta, 47 (2002) 3957.

[26] R. Li, Q. Zhen, M. Drache, A. Rubbens, C. Estournes, R.N. Vannier, Solid State Ionics, 198 (2011) 6.

[27] A.A. Yaremchenko, V.V. Kharton, E.N. Naumovich, A.A. Tonoyan, V.V. Samokhval, J. Solid State Electrochem., 2 (1998) 308.

[28] G. Mairesse, J.C. Boivin, G. Lagrange, P. Cocolios. Int. Patent Application PCT WO 94/06544 (1994).

[29] H. Inaba, H. Tagawa, Solid State Ionics, 83 (1996) 1.

[30] M.A. Panhans, R.N. Blumenthai, Solid State Ionics, 60 (1993) 279.

[31] H. Yahiro, K. Eguchi, H. Arai, Solid State lonics, 36 (1989) 71.

[32] K. Eguchi, T. Setoguchi, T. Inoue, H. Arai, Solid State Ionics, 52 (1992) 165.

[33] D.Y. Wang, D.S. Park, J. Griffith, A.S. Nowick, Solid State Ionics, 2 (1981) 95.

[34] S. Kuharuangrong, J. Power Sources, 171 (2007) 506.

[35] S.S. Baek, N. Lee, B.K. Kim, H. Chang, S.J. Song, J.Y. Park, Int. J. Hydrogen Energy, 37 (2012) 16823.

[36] Y.G. Choi, J.Y. Park, J.W. Son, J.H. Lee, H.J. Je, B.K. Kim, H.W. Lee, K.J. Yoon, Int. J. Hydrogen Energy, 38 (2013) 9867.

[37] B. Zhu, J. Power Sources 114 (2003) 1.

[38] G.Y. Meng, Q.X. Fu, S.W. Zha, C.R. Xia, X.Q. Liu, D.K. Peng, Solid State Ionics, 148 (2002) 533.

[39] J.I. Yamaura, S. Yonezawa, Y. Muraoka, Z. Hiroi, J. Solid State Chem., 179 (2006) 336.

[40] B.J. Wuensch , K.W. Eberman , C. Heremans, E.M. Ku, P. Onnerud, E.M.E. Yeo, S.M. Haile, J.K. Stalick, J.D. Jorgensen, Solid State Ionics, 129 (2000) 111.

[41] P.J. Wilde, C.R.A. Catlow, Solid State Ionics, 112 (1998) 173.

[42] T. Omata, K. Okuda, S. Tsugimoto, S.O.M. Yao, Solid State Ionics, 104 (1997) 249.

[43] M. Pirzada, R.W. Grimes, L. Minervini, J.F. Maguire, K.E. Sickafus, Solid State Ionics, 140 (2001) 201.

[44] Z.G. Liu, J.H. Ouyang, Y. Zhou, J. Xiang, X.M. Liu, 32 (2011) 4201.

[45] Z.G. Liu, J.H. Ouyanga, K.N. Sun, Y. Zhou, J. Xiang, Electrochim. Acta, 56 (2011) 7045.

[46] X.L. Xia, Z.G. Liu, J.H. Ouyang, Y. Zheng, J. Power Sources, 217 (2012) 316.

[47] L.C. Wen, Y.I. Tsai, H.K. Lin, S.C. Chang, M.Y. Lin, H.S. Chang, H.C.I. Kao, L.Y. Jang, M.C. Lee, Y.S. Lee, Solid State Ionics, 253 (2013) 227.

[48] T. Ishihara, H. Matsuda, Y. Takita, J. Am. Chem. Soc., 116 (1994) 3801.

[49] M. Feng, J.B. Goodenough, Eur. J. Solid State Inorg. Chem., 31 (1994) 663.

[50] A.J. Jacobson, Chem. Matter., 22 (2010) 660.

[51] M. Kajitani, M. Matsuda, A. Hoshikawa, S. Harjo, T. Kamiyama, T. Ishigaki, F. Izumi, M. Miyake, Chem. Matter, 17 (2005) 4235.

[52] M. Rozumek, P. Majewski, F. Aldinger, J. Am. Ceram. Soc., 87 (2004) 656.

[53] A. Matraszek, L. Singheiser, D. Kobertz, K. Hilpert, M. Miller, O. Schulz, M. Martin, Solid State Ionics, 166 (2004) 343.

[54] P. Datta, Peram. Majewski, F. Aldinger, J. Eur. Ceram. Soc., 29 (2009) 1463.

[55] S. Kim, M.C. Chun, K.T. Lee, H.L. Lee, J. Power Sources, 93 (2001) 279.

[56] K. Yamaji, H. Negishi, T. Horita, N. Sakai, H. Yokokawa Solid State Ionics, 135 (2000) 389.

[57] M. Kumar, M.A. Kulandainathan, I.A. Raj, R. Chandrasekaran, R. Pattabiraman, Mater. Chem. Phys., 92 (2005) 303.

[58] A. Sinha, B.P. Sharma, P. Gopalan, Electrochim. Acta, 51 (2006) 1184.

[59] K. Kakinuma, T. Arisaka, H. Yamamura, T. Atake, Solid State Ionics, 175 (2004) 139.

[60] H. He, X. Huang, L. Chen, Solid State Ionics, 130 (2000) 183.

[61] H. Inaba, H. Hayashi, M. Suzuki, Solid State Ionics, 144 (2001) 99.

[62] K. Nomura, S. Tanase, Solid State Ionics, 98 (1997) 229.

[63] K. Nomura, T. Takeuchi, H. Kageyama, Y. Miyazaki, Solid State Ionics, 162 (2003) 99.

[64] E.R. Trejo, G. Tavizon, A.A. Landeros, J. Phys. Chem. Solids, 64 (2003) 515.

[65] W. Yao, Z. Tang, Z. Zhang, S. Luo, J. Li, Q. Tan, Mater. Sci. Eng. B, 99 (2003) 309.

[66] T. Shibasaki, T. Furuya, S. Wang, T. Hashimoto, Solid State Ionics, 174 (2004) 193.

EXPERIMENTAL PROCEDURES

Overview

Two series based on $La_{1-x}M_xInO_{3-\delta}$ and $La_{1-x}M_xGaO_{3-\delta}$ (where M=Ca, Sr, Ba) were investigated as potential candidates for intermediate temperature range (400-600 ºC) ionic conductors. All the samples were prepared by solid state reaction method. Each composition was characterized for phase formation, thermal stability, microstructural study and analyzed for electrical conductivity. Characterization of the phases was carried by X-ray diffraction (XRD) method and whenever required, by Raman spectroscopy. scanning electron microscopy (SEM) was used to examine the morphological features of the samples. The gold sputtered fractured surfaces were examined to identify grains, their shape, presence of pores and also the nature and distribution of secondary phases. Thermogravimetric analysis (TGA) was performed to analyze the thermal stability of selected samples. Impedance analyzer was used to study the electrical conductivity of the synthesized samples. In this chapter, the materials used and the experimental procedure followed to prepare the sample and their characterization as mentioned above has been described in detail.

3.1. Materials:

The raw powders used for the synthesis of $La_{1-x}M_xInO_{3-\delta}$ and $La_{1-x}M_xGaO_{3-\delta}$ (where M=Ca, Sr, Ba) are: La_2O_3 (Sigma Aldrich), In_2O_3 (Sigma Aldrich), CaO (Sigma Aldrich), SrO (Sigma Aldrich), BaO (Sigma Aldrich), Ga_2O_3 (Sigma Aldrich), and CH_3COCH_3 (Sigma Aldrich). All the raw materials were of high purity (≥99.9%) and are used in as received condition.

3.2. Sample preparation:

As mentioned above, different samples of the $La_{1-x}M_xInO_{3-\delta}$ and $La_{1-x}M_xGaO_{3-\delta}$ (where M=Ca, Sr, Ba) have been prepared using solid-state reaction method. The sample compositions along with their names are given in Table 3.1 and Table 3.2, respectively. The details of sample preparation and adopted characterization techniques are given in the following flow chart (Fig. 3.1).

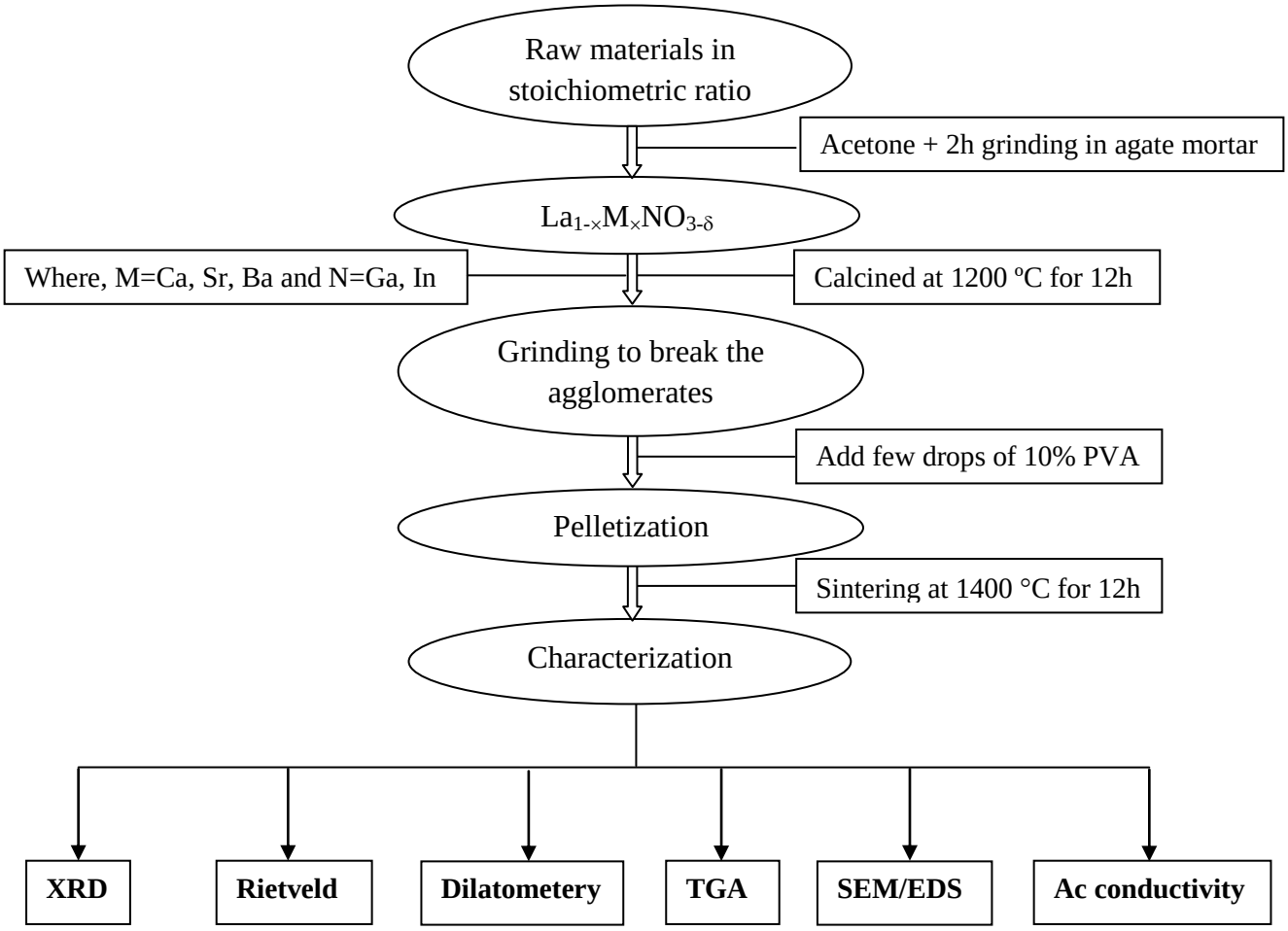

Fig. 3.1: Flow chart showing different stages for sample preparation and characterization.

Table 3.1: $La_{1-x}M_xGaO_{3-\delta}$ series along with their names.

Sample series	Sample Name	Initial stoichiometric ratio
$La_{1-x}Sr_xGaO_{3-\delta}$	LSG-0	$LaGaO_3$
	LSG-5	$La_{0.95}Sr_{0.05}GaO_{3-\delta}$
	LSG-10	$La_{0.90}Sr_{0.10}GaO_{3-\delta}$
	LSG-15	$La_{0.85}Sr_{0.15}GaO_{3-\delta}$
	LSG-20	$La_{0.80}Sr_{0.20}GaO_{3-\delta}$
$La_{1-x}Ca_xGaO_{3-\delta}$	LCG-0	$LaGaO_3$
	LCG-5	$La_{0.95}Ca_{0.05}GaO_{3-\delta}$
	LCG-10	$La_{0.90}Ca_{0.10}GaO_{3-\delta}$
	LCG-15	$La_{0.85}Ca_{0.15}GaO_{3-\delta}$
	LCG-20	$La_{0.80}Ca_{0.20}GaO_{3-\delta}$
$La_{1-x}Ba_xGaO_{3-\delta}$	LBG-0	$LaGaO_3$
	LBG-5	$La_{0.95}Ba_{0.05}GaO_{3-\delta}$
	LBG-10	$La_{0.90}Ba_{0.10}GaO_{3-\delta}$
	LBG-15	$La_{0.85}Ba_{0.15}GaO_{3-\delta}$
	LBG-20	$La_{0.80}Ba_{0.20}GaO_{3-\delta}$

Table 3.2: $La_{1-x}M_xInO_{3-\delta}$ series along with their names.

Sample series	Sample Name	Initial stoichiometric ratio
$La_{1-x}Sr_xInO_{3-\delta}$	LSI-0	$LaInO_3$
	LSI-5	$La_{0.95}Sr_{0.05}InO_{3-\delta}$
	LSI-10	$La_{0.90}Sr_{0.10}InO_{3-\delta}$
	LSI-15	$La_{0.85}Sr_{0.15}InO_{3-\delta}$
	LSI-20	$La_{0.80}Sr_{0.20}InO_{3-\delta}$
	LSI-23	$La_{0.77}Sr_{0.23}InO_{3-\delta}$
	LSI-26	$La_{0.73}Sr_{0.26}InO_{3-\delta}$
	LSI-50	$La_{0.50}Sr_{0.50}InO_{3-\delta}$
$La_{1-x}Ca_xInO_{3-\delta}$	LCI-0	$LaInO_3$
	LCI-5	$La_{0.95}Ca_{0.05}InO_{3-\delta}$
	LCI-10	$La_{0.90}Ca_{0.10}InO_{3-\delta}$
	LCI-15	$La_{0.85}Ca_{0.15}InO_{3-\delta}$
	LCI-20	$La_{0.80}Ca_{0.20}InO_{3-\delta}$
$La_{1-x}Ba_xInO_{3-\delta}$	LBI-0	$LaInO_3$
	LBI-5	$La_{0.95}Ba_{0.05}InO_{3-\delta}$
	LBI-10	$La_{0.90}Ba_{0.10}InO_{3-\delta}$
	LBI-15	$La_{0.85}Ba_{0.15}InO_{3-\delta}$
	LBI-20	$La_{0.80}Ba_{0.20}InO_{3-\delta}$

Pellets of the mentioned series as given in Table 3.1 and 3.2 were prepared by following the steps given in Fig. 3.1. For it, required amount of oxides in a defined stoichiometric ratio were first mixed manually in agate mortar pestle for 2 *h* in acetone medium. The

homogenized mixture so obtained is calcined in alumina crucible at 1200 °C for 12 *h* in air. The heating rate was kept constant (5 °C/min) throughout the heating cycle. The calcined powder was again ground for 2h to break the agglomerates. The calcined powder was pressed into 20 mm of diameter pellets with 1-2 mm of thickness after adding few drops of 10 % polyvinyl alcohol (PVA) as binder in calcined powder. The pressure applied for pelletization was 32 kN/cm^2. The green pellets so obtained were sintered at 1400 °C for 12 *h* with a heating rate of 5 °C/min.

3.3. Characterization of synthesized materials:

The sintered samples were further characterized in order to determine the presence of different phase(s), structural morphology, thermal analysis and ac conductivity. For these analyse, the sintered samples were characterized by X-ray diffraction (XRD), Rietveld refinement, Raman spectroscopy, scanning electron microscopy (SEM), energy dispersive spectroscopy (EDS), thermo-gravimetric analysis (TGA) and uv-vis spectroscopy (UV-Vis). Conductivity was measured by ac-impedance spectroscopy and thermal expansion by dilatometry. The details of these techniques are given below:

3.3.1. Geometric bulk density:

The geometric bulk density of the sintered samples was used to determine quantitatively to know the extent of densification. Initially the sintered samples were polished on emery paper until the parallel surfaces (smooth) were obtained. The dimensions required for the bulk volume in the sintered specimens were measured using a Vernier caliper with least count of 0.02 mm. The mass of the pellet was determined using analytical balance with least count of 0.001g. The bulk density was calculated using equation:

$$\rho = \frac{m}{V} \tag{3.1}$$

here ρ is the bulk density of the specimen, m is the mass and V is the volume of the specimen.

3.3.2. X-ray diffraction:

XRD is one of the primary analytical techniques used to identify the phase formation of the crystalline material and can provide information like lattice parameters, strain, crystallite size etc. The inter-planner spacing was measured using Bragg's law as given below and shown in Fig. 3.2 [1].

$$2d\sin\theta = n\lambda \tag{3.2}$$

Where, d = inter-planner spacing, θ = glancing angle, n = integer, and λ = wavelength of X-rays (1.5406 Å).

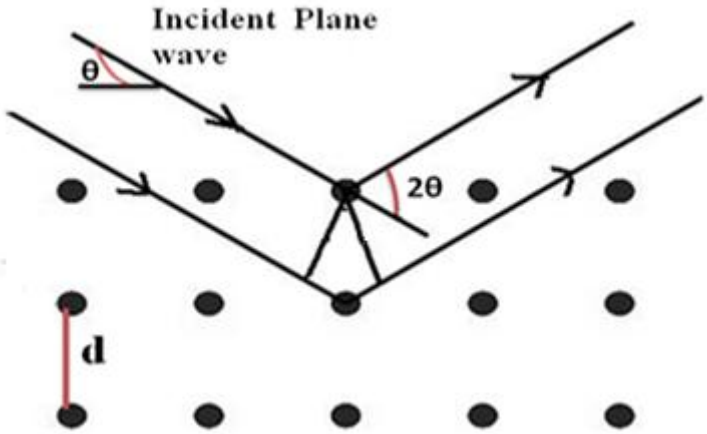

Fig. 3.2: Diagrammatic representation of Bragg's law.

The lattice parameters were calculated using the following equations as:

$$d = \frac{a}{\sqrt{h^2 + k^2 + l^2}} \quad \text{(cubic)} \tag{3.3}$$

$$d = \frac{a}{\sqrt{\frac{h^2}{a^2} + \frac{k}{b^2}^2 + \frac{l^2}{c^2}}} \quad \text{(orthorhombic)} \tag{3.4}$$

Where, h, k and l are the miller indices of crystal planes and a, b and c are the lattice parameters.

3.3.2.1. Indexing of cubic crystals:

A cubic crystal gives diffraction lines whose $\sin^2\theta$ values satisfy the following equation, obtained by combining Bragg's law with inter-planner spacing equation for the cubic system:

$$\frac{\sin^2\theta}{h^2 + k^2 + l^2} = \frac{\sin^2\theta}{s} = \frac{\lambda^2}{4a^2} \tag{3.5}$$

Since, the sum $s = h^2 + k^2 + l^2$ is always an integral and $\frac{\lambda^2}{4a^2}$ is a constant for any one pattern, so to index a cubic system, we have to find a set of integers s, which yield a constant quotient when divided by one into the observed $sin^2\theta$ values. The set of values of *s*, which describes the four common lattice types are:

Simple cubic: 1,2,3,4,5,6,8,9,10,11,12,13,14,16,…..

Body centered cubic: 2,4,6,8,10,12,14,16,……..

Face centered cubic: 3,4,8,11,12,16,……

Diamond cubic: 3,8,11,16,……

In addition, the Bravais lattice for cubic system can also be identified by inspection: there is almost regular sequence of lines in simple cubic and body centered cubic patterns, but the former has almost twice as many lines, while a face centered cubic pattern is characterized by a pair of lines, followed by a single line, etc.

3.3.2.2. Non-cubic systems:

For non-cubic systems, the indexing is not as simple as in cubic. One has to use analytical methods of indexing, which involve arithmetic manipulation of the observed $sin^2\theta$ values in an attempt to find the relationship among them. In orthorhombic systems, the basic equation governing the $sin^2\theta$ values is:

$$\sin^2\theta = Ah^2 + Bk^2 + Cl^2 \qquad (3.6)$$

Where *A*, *B* and *C* are constants and have to be determined. The detailed method of analysis is given by Cullity [1].

3.3.2.3. Phase identifications:

Phase identification in the sample was performed using PANalytical X'Pert PRO X-ray diffractometer with a copper target X-ray tube and a nickel filter. The X-ray tube was operated at 40 kV and 30 mA and the diffraction data was recorded at a scanning rate of 2° min^{-1} with angular range (2θ) of 10-80°. PANalytical X' Pert PRO diffractometer equipped with new fast detector (PIXcel^{1D}), diffracted beam monochromator, and a sample changer was used to detect the diffracted X-rays. Commercial data analysis software X'Pert High Score was used to smooth the data, peak search and match the raw data. Each specimen was mounted on standard sample holder. The well crushed sintered powders were used for XRD analysis. The data was compared with standard ICDD database and matched manually, wherever possible.

3.3.3. Rietveld analysis:

The Rietveld analysis is a powerful technique used to determine quantitatively the crystal structure, phase analysis, %tage of crystallinity, atomistic resolution, unit cell size determination, residual strain etc. Rietveld analysis was used on selective samples to verify

the phases present. For this, *FULLPROF-2009* software was used. The raw data obtained from XRD was used for this analysis. Also, the basic parameters for initial approximation were used from literature.

3.3.4. Raman spectroscopy:

Raman spectroscopy provides information about molecular vibrations that can be used for sample identification and quantitation. The technique involves a monochromatic light source (i.e. laser) on a sample and detecting the scattered light. The majority of the scattered light is of the same frequency as the excitation source; this is known as Rayleigh or elastic scattering. A very small amount of the scattered light (~10^{-5} % of the incident light intensity) is shifted in energy from the laser frequency due to interactions between the incident electromagnetic waves and the vibrational energy levels of the molecules in the sample. Plotting the intensity of this "shifted" light versus frequency results in a Raman spectrum of the sample. Generally, Raman spectra are plotted with respect to the laser frequency such that the Rayleigh band lies at 0 cm^{-1}. On this scale, the band positions lie at frequencies that correspond to the energy levels of different functional group vibrations. The Raman spectrum can thus be interpreted similar to the infrared absorption spectrum.

Raman spectra are clearer than mid-IR spectra, Raman bands are narrower, over tone and combinational bands are generally weak. Further, Raman spectroscopy can be used for both qualitative and quantitative applications. The spectra are very specific, and chemical identifications can be performed by using search algorithms against digital databases. As in infrared spectroscopy, band areas are proportional to concentration, making Raman amenable to quantitative analysis. In fact, because Raman bands are inherently sharper than their infrared counterparts, isolated bands are often present in the spectrum for more straight forward quantitative analysis. Raman spectra were obtained for selective samples using a Renishaw spectrometer coupled with Ar^{+} ion laser having the wavelength of 5145 Å.

3.3.5. Scanning electron microscopy (SEM)/ Energy dispersive spectroscopy (EDS):

The scanning electron microscope uses a focused beam of high-energy electrons to generate a variety of signals at the surface of solid specimens. The signals that derive from electron-sample interactions reveal information about the sample including external morphology (texture), chemical composition, crystalline structure and orientation of materials making up the sample. The sample for SEM analysis is mounted on a conductive substrate such as copper stub and gold sputtered in vacuum. Data is collected over a selected area of the surface of the sample, and a 2-dimensional image is generated that displays spatial variations

in these properties. Areas ranging from approximately 1 cm to 5 microns in width can be imaged in a scanning mode using conventional SEM techniques. The SEM is also capable of performing analyses at selected point locations on the sample; this approach is especially useful in qualitative or semi-quantitative analysis determining chemical compositions (using EDS), crystalline structure and crystal orientation (using EBSD). In the present study, the SEM/EDS were done using JEOL JSM-6510LV (INCA-ACT Energy 200).

3.3.6. Thermo-gravimetric analysis (TGA):

Thermogravimetry (TGA) is a technique that measures the change in weight of a sample as it is heated, cooled or held at constant temperature under controlled atmosphere. It is mainly used to study thermal stability, decomposition and moisture content in a compound. A TGA analysis is performed by gradually raising the temperature of a sample in a furnace. In TGA, weight loss is observed if a thermal event involves loss of a volatile component. From TGA analysis chemical reactions, such as combustion which involves weight losses observed but the physical changes such as melting do not appear. The weight of the sample is plotted against temperature or time to illustrate thermal transitions in the material – such as loss of solvent and plasticizers in polymers, water of hydration in inorganic materials, and finally, decomposition of the material.

The TGA of selected sintered powders of sintered samples was analyzed using Perkin Elmer Model: Diamond Pyris at a heating rate of 10°/min in N_2 atmosphere. Analysis of all the samples was performed using Al_2O_3 powder as reference.

3.3.7. UV-Vis spectroscopy measurements:

UV-Visible spectroscopy involves the reflection/absorption of photons in the UV-Vis region. It uses light in the visible and near UV range. The absorption in the visible range directly affects the color of the chemicals involved. In this region of the electromagnetic spectrum, molecules undergo electronic transitions. UV and visible light are energetic enough to promote outer electrons to higher energy levels. The UV-Vis spectra have broad features that are of limited use for sample identification but are very useful for quantitative measurements. It is often used in physical and analytical chemistry for the identification of substances through the spectrum emitted from or absorbed by them. In the present work, absorption was measured in the wavelength from 1900-9000 Å using a Hitachi's U-3900H double beam spectrophotometer. The instrument is capable of recording the wavelength with an accuracy of 1 Å and the absorption was measured with an accuracy of about 1-3%. The functioning of this instrument is relatively straightforward. A beam of light from a visible and *UV* source is

separated into its component wavelengths by a diffraction grating. Each monochromatic beam is split into two equal intensity beams by a half-mirrored device. One beam out of these two beams passes through the sample, while other passes through the reference. After passing through the sample, the monochromatic beams are converged and converted to electrical signal by a detector (photomultiplier tube). The spectrum is then recorded in the applied wavelength range. Over a short period of time, the spectrophotometer automatically scans all the component wavelengths. The region normally scanned from UV is 1900-4000 Å, and the visible portion from 4000-8000 Å. The light source uses *WI* lamp for visible range and a *D*2 lamp for ultraviolet range that switches wavelength depending on the measurement. Spectra are obtained by scanning the wavelengths for quantitative measurements.

In the present work, this technique has been used on selective samples to calculate the Urbach energy which represent the disorderness in the system. The substitution in the perovskite may lead to distortions/disorderness in the system, which decreases the optical band gap energy as well as increase in Urbach energy. So, by this technique, we can estimate the effect of substitution in the perovskite system.

3.3.8. Conductivity measurement:

Ionic conduction in solid-state materials is due to flow of ions across the material. In ideal crystal, constituent particles are arranged in regular and periodic manner in closed pack form. So, little space is left for ionic movement. In general, this space is sufficient for vibrational motion of ions around its equilibrium position. Since, no crystal is ideal so for non-zero temperature, defect formation takes place in the crystal lattice. The degree of this disorder depends on temperature, pressure, doping or impurity and density of the material.

3.3.8.1. Frenkel and Schottky defects:

Two types of point defects are very common in ionic crystals, i.e., Schottky and Frenkel defects. These defects are also called stoichiometric defects, in which the crystal chemistry, i.e., ratio of the cations to anions does not change [2]. In Schotky defects, a pair of ions (i.e. cation and anion) are absent from its lattice positions, leading to two vacant spaces. In Frenkel defects, a single ion is absent from its regular position and occupying interstitial sites. Both Frenkel and Schottky defects leads to vacant sites, and any ion in the immediate vicinity may jump to occupy the vacant position, thus leads to migration of vacancies. This process can lead to transport of ions across the solid giving rise to ionic conductivity. This mechanism is known as vacancy migration [3].

3.3.8.2. Non-stoichiometric defects:

Non-stoichiometric defects arise by selective addition or loss of one (or more) of the constituent of the crystal and consequently, lead to a change in crystal chemistry. According to thermodynamic argument, the composition of every compound varies within range of its existence regime [2]. For example, if an oxide were annealed in a high oxygen partial pressure, it would be fair to assume that the number of oxygen atoms should be relatively greater than the number of cations. Conversely, if the oxygen partial pressure was very low, one would expect the cation concentration to be higher. The importance of the defects lie in the fact that many physical properties such as colour, density, morphology, electrical conductivity, magnetic susceptibility depend on the amount of non-stoichiometry in the compound.

AC conductivity technique has been used to study the electrical measurement in the present system. In this technique, sinusoidal signals of varying frequencies were applied to sintered pellets and output signals were measured. The real and imaginary impedance at each frequency was measured at constant temperature. Ideally, electrode and electrolyte (grain and grain boundary) should have different time constant. Accordingly, the relaxation frequency range for each process should be different. For well separated bulk and grain boundary contribution, the Nyquist plot is shown in Fig. 3.3.

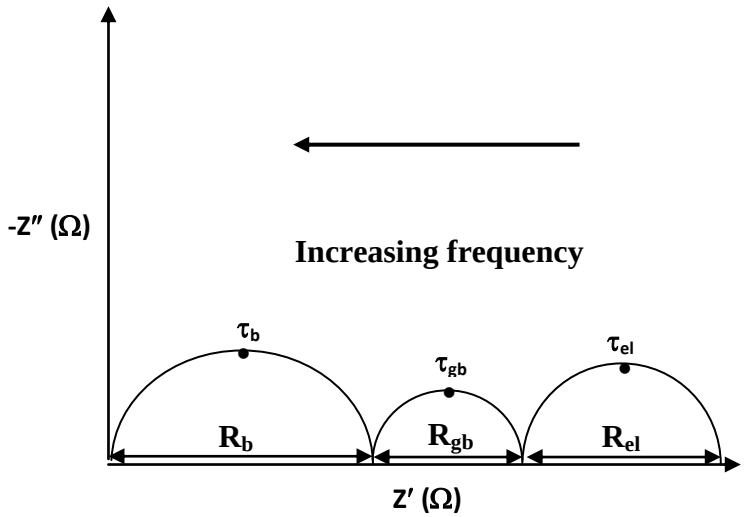

Fig. 3.3: Nyquist plot indicating bulk resistance (R_b), grain boundary (R_{gb}) and electrode (R_{el}) contribution.

From Fig. 3.3, the first semicircle on high frequency region corresponds to bulk region. The second semicircle contributes to grain boundary region. The semicircle at low frequency region represents the electrode contribution. τ_b, τ_{gb}, and τ_{el} corresponds to relaxation times

corresponding to bulk, grain boundary and electrode, respectively. The peak of the semicircle in the complex plane plot enables us to evaluate the relaxation frequency (f_{max}) of the bulk material in accordance with the relation:

$$\omega_{max}\tau = 1, \omega_{max} = \frac{1}{\tau} = \frac{l}{Rc} \tag{3.7}$$

$$\text{or,} \quad f_{max} = \frac{l}{2\pi Rc} \tag{3.8}$$

Where, R and C refers to resistance and capacitance, respectively, τ is relaxation time, and $\omega = 2\pi f$, is the angular frequency. The conductivity (σ) of the material, a thermally activated process obeying Arrhenius behavior, is estimated in terms of resistance (R), evaluated from the impedance spectrum. It is expressed as:

$$\sigma = A_o \exp\left[\frac{-E_a}{kT}\right] \tag{3.9}$$

where A_o= pre-exponential factor, E_a= activation energy, k = Boltzmann constant, and T= absolute temperature. So, by using this technique, the contribution of bulk, grain boundary and electrode can be calculated at suitable temperature range.

In the present study, impedance analyzer, with model: Solartron 1260 was used to analyze the ac conductivity behavior of the sintered samples. The surfaces of sintered sample was initially polished using 600 grid emery papers. The polished samples were then ultrasonically cleaned for 5 min in acetone medium. These surfaces were then gold sputtered to make electrical contacts. Electrical measurements were performed from room temperature to 800 °C with frequency range of 0.1-10^6 Hz in air. Wherever possible, the data was analyzed using *ZSimpWin* software. The ac conductivity was calculated using the equation:

$$\sigma = \frac{1}{\rho} = \frac{l}{RA} \tag{3.10}$$

Where, ρ=electrical resistivity of the material, l=thickness and A = area of the sintered sample.

By using equation (3.10) and (3.11), the Arrhenius plot was drawn. By this, the electrical behavior of the sample was investigated with temperature.

3.3.9. Dilatometric study:

The dilatometry is a thermo-analytical technique used to determine the thermal expansion coefficient (TEC), softening point, phase transition, shrinkage, and stress relaxation. A precise understanding of this behavior can provide insight into firing processes, the influence of additives and raw materials, densification and sintering properties, reaction kinetics, phase transitions, and thermal shock. Dilatometer can be applied not only to solid samples, but also to powders and pastes. It can also be used to carry out rate-controlled sintering studies on reactive powders in fields such as advanced ceramics or powder metallurgy.

Pushrod dilatometer is a method for determining dimensional changes versus temperature or time while the sample undergoes a controlled temperature program. The degree of expansion divided by the change in temperature is called the material's expansion coefficient (α) and generally varies with temperature as given below:

$$\alpha = \frac{1}{L_o}\left(\frac{\Delta l}{\Delta T}\right) \tag{3.11}$$

where, α = thermal expansion coefficient, L_0 = initial sample length, Δl= change in length, ΔT= change in temperature.

In the present work, TEC measurements of the sintered samples was done by dilatometer, NETZSCH (Model DIL 402 PC) in air using alumina kit including alumina push rod at a heating rate of 5°C/min within the range of room temperature to 1000 °C. Thermographs had been taken between temperature and percentage change in length of the sample.

References:

[1] B.D. Cullity, S.R. Stock, Elements of X-Ray Diffraction, Third edition, Addison-Wesley USA (2002).

[2] M.W. Barsoum, Fundamental of Ceramics, Institute of Physics, Bristol (2003).

[3] P.P. Kumar, S. Yashonath, J. Chem. Sci., 118 (2006) 135.

RESULTS AND DISCUSSION

Overview

In this chapter, the experimental results of the synthesized series are presented. In this entire work, the effect of Sr^{2+}, Ca^{2+} and Ba^{2+} substitution in $LaGaO_3$ and $LaInO_3$ systems have been studied to develop electrolyte materials for IT-SOFC applications. The materials were synthesized using solid-state reaction method. In general, Ca^{2+}-substitution improved grain growth and high relative density among all the systems. It was observed that 10 mol% substitutions are ideal substitution in the synthesized series. Moreover, *A*-site substitution in $LaGaO_3$ introduces phase transformation viz. orthorhombic to rhombohedral (at ~150 °C), and also partially stabilize the rhombohedral phase at room temperature. The effect of this phase stability on ionic conductivity is evaluated. Moreover, Ba-substitution in $LaGaO_3$ forms secondary melilite phase ($LaBaGa_3O_7$), whereas, when substituted in $LaInO_3$, it forms polymorphic cubic and orthorhombic perovskite phases. The preferential occupancy of Ca^{2+} at In-site in $LaInO_3$ is specifically analyzed using Raman spectroscopy. Morphology, grain size and their distribution is also analyzed and discussed in this chapter. Thermal expansion behavior with temperature for all the substituted samples has been analyzed. The ionic conductivity of all the samples has been evaluated using impedance spectroscopy technique from room temperature to 800 °C in air. The conductivity behavior is analyzed using Arrhenius plots, and the possible conduction mechanisms have been discussed.

4.1. $La_{1-x}Sr_xGaO_{3-\delta}$ ($0 \leq x \leq 0.20$) systems:

As given in experimental techniques, all samples are synthesized by solid-state reaction method. The as-prepared samples are characterized by various techniques to establish the effect of grain and grain boundary resistance with structural features of the system. The results are discussed in the light of electrical conductivity with structural morphology and order/disorder phase transformations.

4.1.1. X-ray diffraction analysis:

Fig. 4.1 represents the XRD pattern of Sr-substituted $LaGaO_3$ samples. For $La_{1-x}Sr_xGaO_{3-\delta}$ system, the peaks were indexed with $LaGaO_3$ phase (ICDD card number 01-089-7833). The crystal structure is perovskite with space group *pbnm*. The relative density of all the samples is more than 90 % as given in Table 4.1. Moreover, some additional XRD peaks were seen in LSG-15 and LSG-20, which were indexed with secondary phase $LaSrGa_3O_7$ (ICDD card number 00-045-0637).

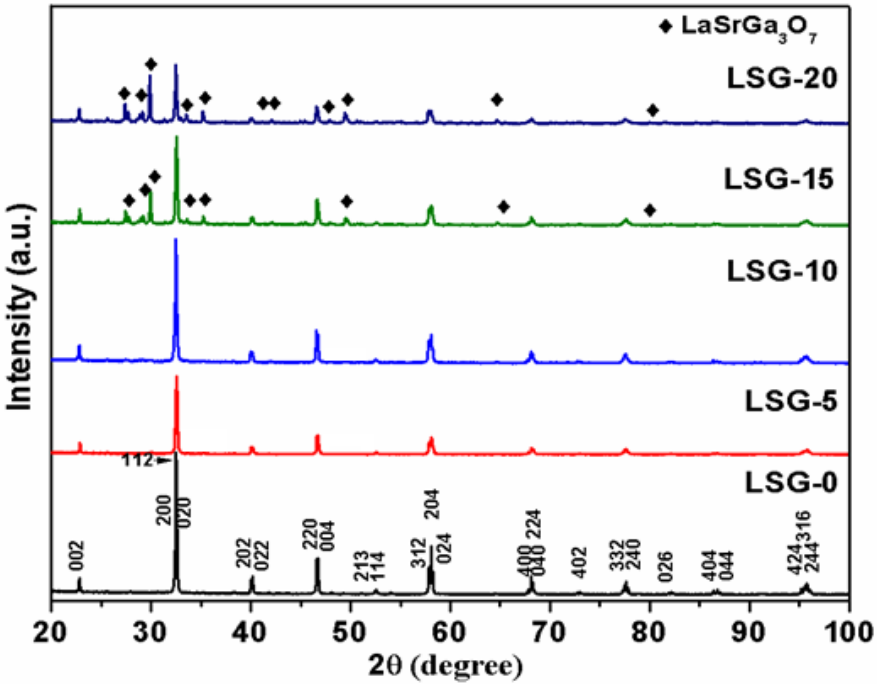

Fig. 4.1: X-ray diffraction pattern of LSG samples.

Lattice parameters, unit cell volume (V_L), occupied volume, i.e., volume occupied by all the ions in unit cell (V_O), cell volume per formula (V_C) and free volume (V_f), which is V_C minus V_O of the sintered samples is given in Table 4.2. The method of calculation of these parameters is well reported [1].

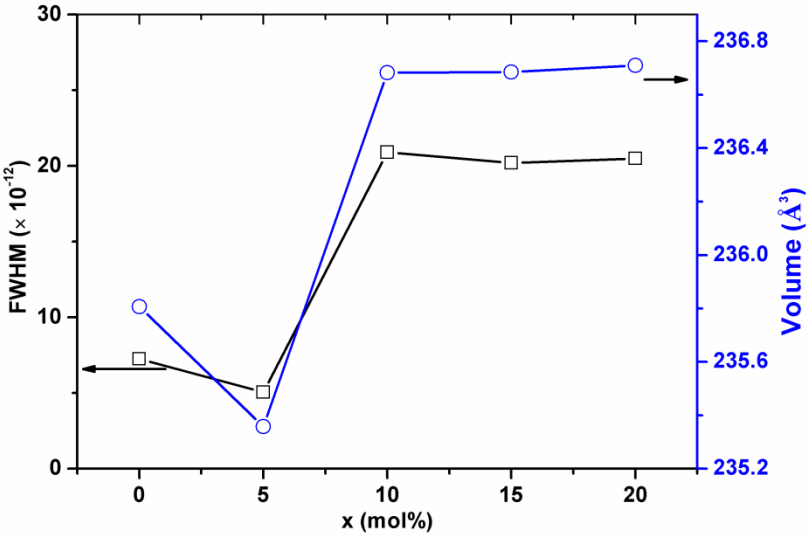

Fig. 4.2: FWHM and lattice volume with composition.

Table 4.1: Strain and density of as-sintered LSG samples.

Sample name	Density of sintered sample (g/cm^3)	Relative density (%)	Strain (ϵ) $\times 10^{-4}$
LSG-0	6.86	95	3.60
LSG-5	6.41	90	7.11
LSG-10	6.48	92	7.13
LSG-15	6.51	93	7.69
LSG-20	6.41	93	10.90

Table 4.2: Calculated lattice parameters and unit cell volume for LSG samples.

Sample name	a (Å)	b (Å)	c (Å)	V_L (Å^3)	V_C (Å^3)	V_O (Å^3)	V_F (Å^3)	t
LSG-0	5.5223	5.4934	7.7731	235.8063	58.95	46.03	12.92	0.9661
LSG-5	5.5176	5.4917	7.7673	235.3576	58.84	45.83	13.01	0.9675
LSG-10	5.556	5.4663	7.7931	236.683	59.17	45.64	13.53	0.9689
LSG-15	5.5253	5.4930	7.7984	236.6851	58.84	45.45	13.39	0.9703
LSG-20	5.5266	5.4959	7.7968	236.8172	59.05	45.26	13.36	0.9716

Further, according to Vegard's law, the lattice parameters should vary linearly with substitution in single phase and remain invariant in the multiphase system [2]. In the present system, the lattice parameter decreases slightly from LSG-0 to LSG-5, then increases up to

LSG-10, and becomes invariant for higher Sr-substitution. This behavior can be explained on the basis of oxygen ordering in the LSG-5 sample. Initially, the substitution of Sr^{2+} (r_{XII} =1.44Å) at La^{3+} (r_{XII} =1.36Å) sites create oxygen vacancies, which affect/reduce the unit cell size slightly. Additionally, it seems that for 5 mol% substitution of Sr^{2+} at La^{3+} site may lead to oxygen vacancy ordering. The decreased full width half maximum (FWHM) in LSG-5 sample is an indication of oxygen ordering as shown in Fig. 4.2. This type of lattice parameter anomaly has also been reported by Xing *et al.* [3]. Furthermore, the ordering in the system could lead to the decrease in overall conductivity of the system which is discussed in conductivity section. With further substitution up to LSG-10, the behavior is in accordance with Vegard's law. However, when the secondary phase formation takes place ($x \geq 0.15$), there is hardly any change in lattice parameters.

The parameters given in Table 4.2 are calculated by using Shanon ionic radii [4]. Table 4.2 shows that up to LSG-10, the V_F increases with Sr-substitution. However, it decreases beyond this substitution. It is further reported that higher the V_F, greater will be the ionic conductivity because of more volume available for conduction [1]. However, higher V_F may decrease the stability within the system. On the other hand, the tolerance factor (t) increases with substitution, which is an indicative of phase stability of perovskite phase [5, 6]. The lattice distortion from the ideal cubic structure is related to the higher degree of anisotropy in oxygen sites, which decreases the ionic conductivity of the compound [6]. The strain in these samples was calculated using Williamson's Hall equation given as [7, 8]:

$$\beta_{hkl} \cos\theta = K\lambda/D + 4\varepsilon \sin\theta \qquad (4.1)$$

Where, β_{hkl} is FWHM of respective XRD peaks; K = shape factor (0.9); λ = wavelength of X-ray, D = crystallite size; ε = strain parameter. Equation (4.1) represents the uniform deformation model (UDM), where the strain is considered to be identical in all crystalline directions, thus assuming the isotropic nature of the crystal. The observed strain for LSG samples is given in Table 4.1. These values indicate that the strain increases uniformly with the increase in Sr-content. It further indicates the effect of Sr-substitution or/and secondary phase in lanthanum gallate perovskite lattice. Since the observed behavior of LSG-15 and LSG-20 are similar, so LSG-20 is not discussed in subsequent sections.

4.1.2. Microstructural analysis:

Fig. 4.3(a-h) shows the morphology at different magnifications obtained from the fractured surface of the samples. The micrographs (Fig. 4.3a-b) show that LSG-0 is denser than other

samples. However, two types of structural features are observed. The entire structure is contained by bigger grains of nearly 12-15 μm having faceted features. However, within a grain and also at triple points, different features are observed. It appears that initially, smaller grain has formed which grows to bigger size. Since, diffusion in ceramic materials is a sluggish process, so some of the smaller grains (~3 μm) within larger grains are retained. Moreover, the entire structure gives distinct bimodal distribution of grains. Because of the presence of these smaller grains, grain boundary contribution towards conductivity may dominate at the low temperature. Fig. 4.3(c-d) shows the micrographs of LSG-5 sample and Fig. 4.3(e-f) is for LSG-10 sample. The average grain size of these substituted samples is almost same with little variation (1-2 μm). In LSG-5 sample, little porosity is also observed.

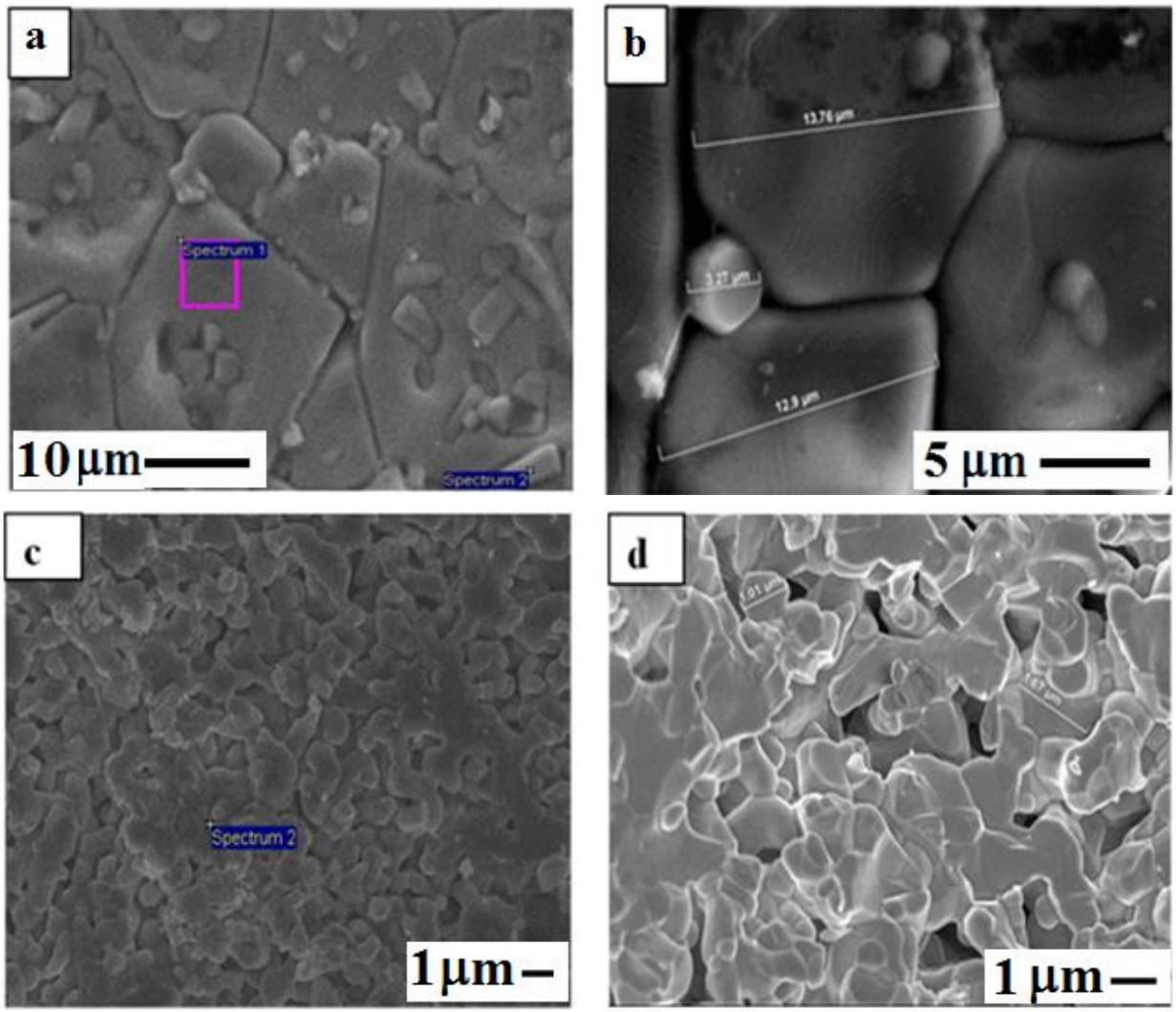

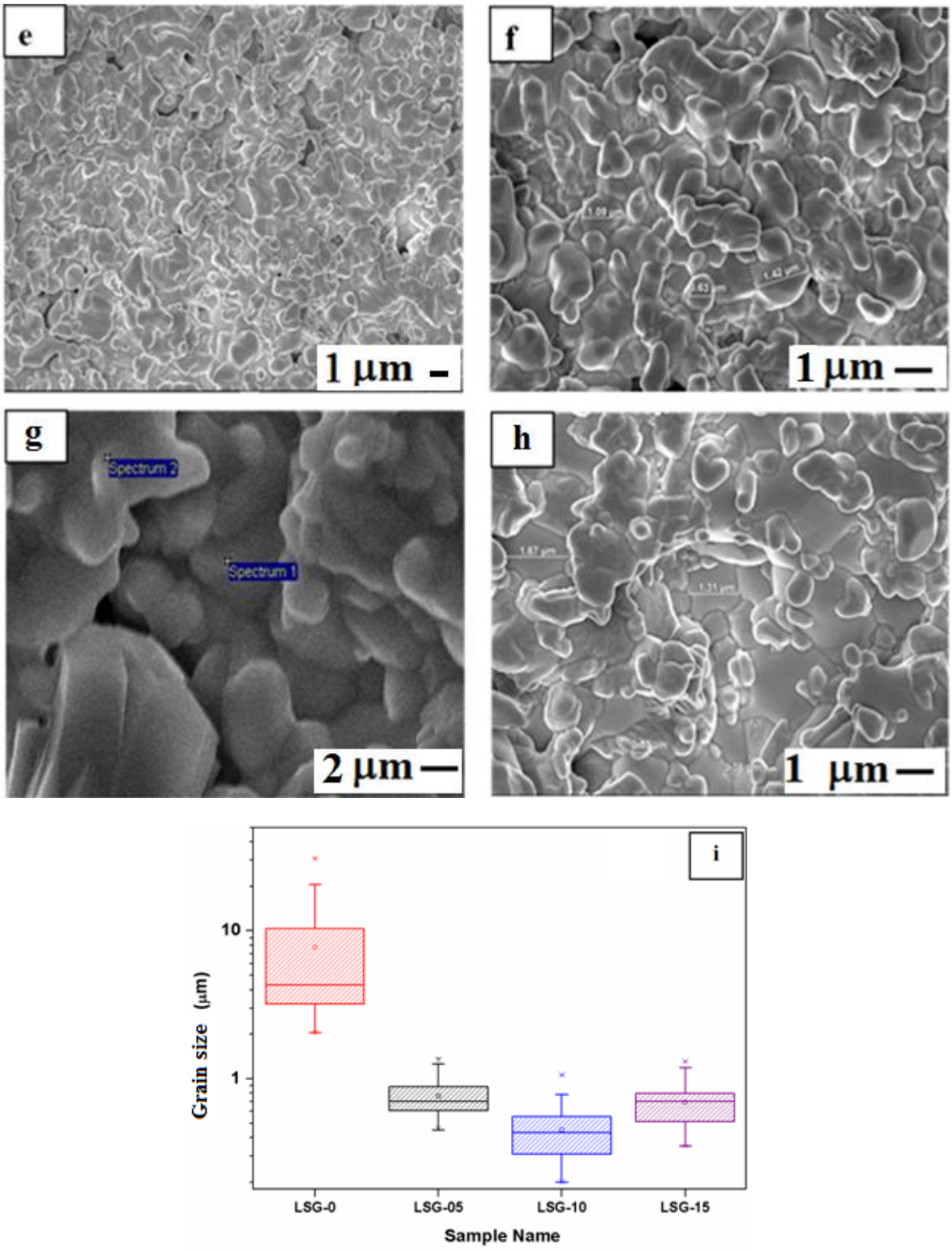

Fig. 4.3: SEM micrographs of fractured surfaces of $La_{1-x}Sr_xGaO_{3-\delta}$ system at different magnifications (a) and (b) LSG-0, (c) and (d) LSG-5, (e) and (f) LSG-10, (g) and (h) LSG-15 and (i) grain size distribution.

Table 4.3: EDS analysis of selected LSG samples.

Sample name	Element	Weight (%)	Atomic (%)	Empirical formula
LSG-0 (spectrum-1)	O K Ga L La L	14.91 32.21 52.88	52.51 26.03 21.45	$LaGa_{1.23}O_{2.448}$ ~$LaGaO_3$
LSG-0 (spectrum-2)	O K Ga L La L	18.81 36.76 44.43	58.13 26.06 15.81	$LaGa_{1.65}O_{3.67}$ ~$LaGaO_3$
LSG-5	O K Ga L Sr L La L	20.15 27.01 0.59 52.25	62.05 19.08 0.33 18.53	$La_{0.98}Sr_{0.018}Ga_{1.01}O_{3.29}$ ~$LaGaO_3$ (solid solution phase)
LSG-15 (spectrum 1)	O K Ga L Sr L La L	18.35 24.51 1.38 55.77	59.87 18.35 0.82 20.96	$La_{0.96}Sr_{0.038}Ga_{0.84}O_{2.75}$ ~$LaGaO_3$ (solid solution phase)
LSG-15 (spectrum 2)	O K Ga L Sr L La L	19.95 38.20 13.56 28.29	57.88 25.45 7.21 9.46	$LaSr_{0.76}Ga_{2.69}O_{6.12}$ ~$LaSrGa_3O_7$

This decrease in grain size and increased grain boundary (as compared to LSG-0), could decrease the overall conductivity in the LSG-5 sample as discussed in conductivity section. For LSG-10 sample (Fig. 4.3e-f), it is observed that amount of porosity is less, and grain size is smaller as compared to LSG-0. Fig. 4.3(g-h) shows the micrographs of LSG-15 sample. The structure clearly shows the presence of two different types of grains having variation in grain shape. Moreover, some porosity with larger grains is also observed. The two different phases in this sample have also been confirmed in the XRD analysis (Fig. 4.1). The grain size distribution with composition is shown in Fig. 4.3(i). In comparison to unsubstituted sample (LSG-0), the average grain size decreased up to LSG-10. It is because Sr^{2+} provides the large number of nucleating sites, which facilitate more grains, thus reducing the average grain size [9]. However, for higher Sr-substitution (LSG-15), the average grain size is slightly increased. It is the effect of secondary phase co-formed in this sample as also discussed in XRD section. To get quantitative idea of phase formed, EDS analyses of selected samples are shown in Fig. 4.3(a, c, g). The corresponding element distributions along with the empirical formula are given in Table 4.3. The EDS analysis for LSG-0 indicates the formation of single perovskite phase as is evident from the empirical formula given in Table 4.3. Fig. 4.3(c) represents the spectra taken for LSG-5 sample, which shows uniform phase formation. The empirical formula for it is closer to $LaGaO_3$ where Sr is dissolved and forms solid solution phase. However, EDS analysis of LSG-15 (Fig. 4.3g) could show two distinct phases (Table

4.3), which is also observed in XRD pattern. Since EDS gives qualitative analysis, so the elemental concentration observed also differs. Moreover, the X-ray analysis along with EDS presents a satisfactory data for phase analysis in the observed microstructures.

4.1.3. TEC analysis:

TEC study of the samples (Fig. 4.4) has been performed to investigate the lattice expansion behavior at higher temperatures (50-800 ºC) in air. The drop in TEC around 150 ºC for LSG-0, corresponds to well reported orthorhombic to rhombohedral phase transition [9-11]. For similar type of LSGM system [9], it has been reported that substitution at A and B-site leads to phase transitions from room temperature (RT) to 800 ºC, where the system is orthorhombic at RT and undergoes orthorhombic→monoclinic (pseudo-orhombohedral) transition at around 150 ºC, from monoclinic (pseudo-orhombohedral)→monoclinic (pseudo-rhombohedral) around 250-500 ºC. The third transition has been reported in the region 500-750 ºC which corresponds with monoclinic (pseudo-rhombohedral)→rhombohedral. In the present system, we have observed two transitions (Fig. 4.4) one, around 150 ºC and another at 500-600 ºC. Moreover, it is seen that the substitution of Sr at the A-site shifts the transition to lower temperature. Furthermore, the depression in the transition curve also decreases with the increase in Sr-substitution. Also, the second transition around 500-600 ºC appear from LSG-0 to LSG-10, and is diminished for mixed phase sample (LSG-15) in Fig. 4.4. It might be ascribed that secondary phase ($LaSrGa_3O_7$) could have obstructed the phase transition around 500-600 °C. Moreover, it is also reported in literature that, A-site substitution in ABO_3 might have stabilized the disordered rhombohedral phase to room temperature [12, 13].

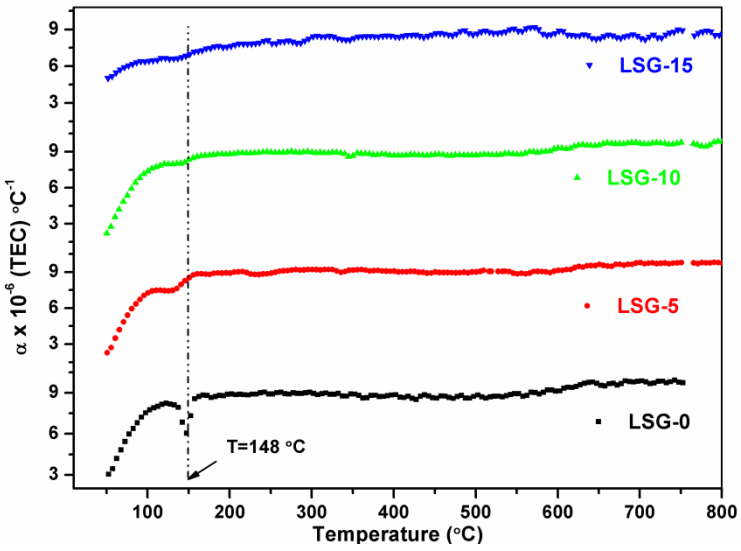

Fig. 4.4: Thermal expansion coefficient for $La_{1-x}Sr_xGaO_{3-\delta}$ system.

This behavior can be further supported on the basis of the tolerance factor (*t*). It is a well-known fact that phase transition temperature decreases with the increase in *t* [11]. Since, *t* increases from 0.966 (LSG-0) to 0.970 (LSG-15) (Table 4.2), which in turn decrease tilting of GaO_6 octahedral [11]. The lesser tilting of GaO_6 octahedral allows the rearrangement of the octrahedral during phase transition and requires lesser thermal energy to make thermally activated phase-transition. For LSG-15, the second transition almost disappears indicating the complete rhombohedral phase formation at temperature around 150 ºC and forms thermally stable system from 150 to 800 ºC which is the desired operating temperature range for IT-solid electrolytes for SOFCs. TEC of all the samples from 600-800 ºC (Table 4.4) are found to be compatible with other reported components of SOFCs [9, 13]. The thermal expansion behavior below 150 °C show that the thermal expansion decreases slightly with Sr^{2+} substitutions. This trend is in accordance with earlier reports that more porous materials have lower TEC [14].

4.1.4. TGA analysis:

Phase stability of as-sintered samples at the higher temperature in N_2 is analyzed using TGA analysis. Fig. 4.5 shows the TGA result for heating cycle. All the samples show regular weight loss with the increase in temperature. The weight loss upto 200 °C is due to water loss incorporated due to hygroscopic nature of these samples [15]. The weight loss from 200 to 800 °C can be due to loss of lattice oxygen at the higher temperature. In addition, the weight loss for unsubstituted sample (LSG-0) is minimum (~0.8 % upto 800 °C) among all synthesized samples.

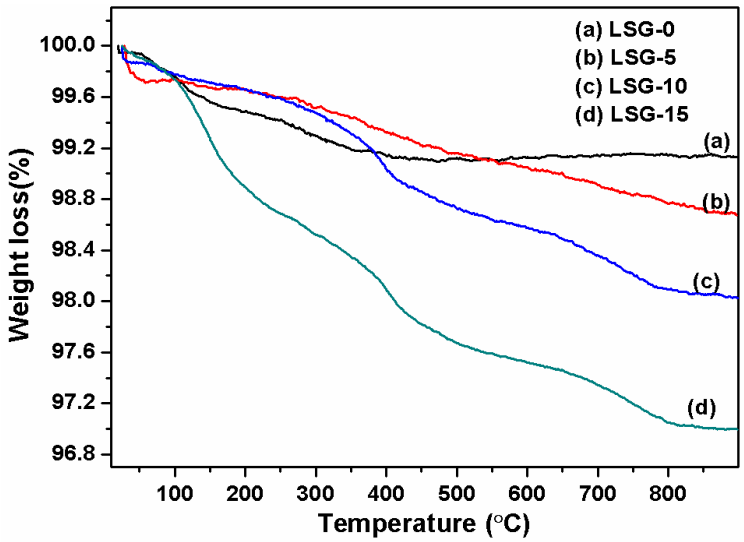

Fig. 4.5: TGA for $La_{1-x}Sr_xGaO_{3-\delta}$ system in N_2.

However, the weight loss gradually increases with the increase in Sr-substitution in these samples. The maximum weight loss occurred for LSG-15 (~3%). This behavior could be due to substitution of larger cation size of Sr^{2+} (r_{XII} = 1.44 Å) at La^{3+} (r_{XII} = 1.36Å) site, which may lead to weakening of cation-oxygen bond strength. It further indicates that higher Sr-content leads to decrease the stability of these samples in the inert atmosphere.

4.1.5. Impedance analysis:

Impedance analysis for all sintered samples has been performed in air and Nyquist plots of LSG-0 and LSG-10 samples at 500 ºC are shown in Fig. 4.6 (a-b). Two consecutive semicircular curves are observed over the measured frequency range.

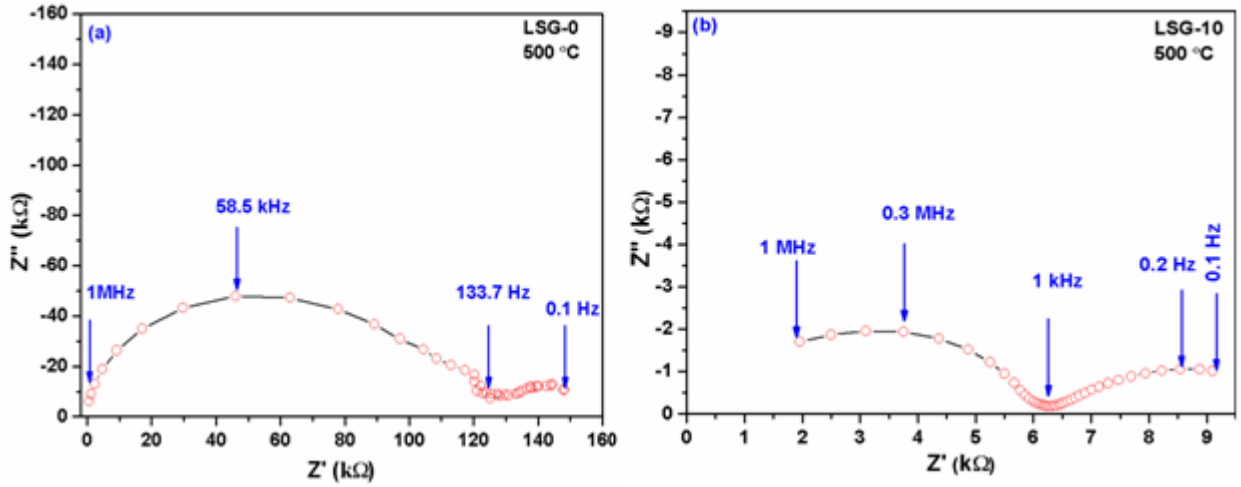

Fig. 4.6: Impedance plots of $La_{1-x}Sr_xGaO_{3-\delta}$ system for (a) LSG-0 and (b) LSG-10 compositions.

The first arc at the high-frequency region represents the bulk response, and the lower frequency region represents the electrode contribution. Within bulk contribution, two ac conduction mechanisms occur: (i) long range ac conductivity, and (ii) localized transport of oxygen vacancies around aliovalent impurity [16]. The long-range ac conductivity occurs due to long range motion of the vacancies introduced by the charge compensation effect as represented by using Kronig-Vink notation as:

$$2SrO \xrightarrow{La_2O_3} 2Sr'_{La} + V_o^{\bullet\bullet} + 2O_o^{x} \qquad (4.2)$$

where, Sr'_{La} means Sr in La site with the apparent unit negative charge (denoted by symbol ') and $V_o^{\bullet\bullet}$ is the vacancy in the oxygen site with double positive charge, O_o^{x} means the lattice oxygen with mean charge zero. The excess of oxygen vacancies so formed are helpful for the hopping mechanism and contributes for the long-range conductivity of the substituted

samples. The contribution of the second mechanism is negligible compared to first and is often ignored [16].

In Fig. 4.6 (a), the Nyquist plot of LSG-0 shows the large bulk resistance and small grain boundary resistance. The capacitance values are calculated by the simple relation $\omega_{max}RC = 1$. Moreover, the capacitance value at higher-frequency semicircle and lower frequency semicircle is 0.6 pF and 0.6 μF respectively, which infer that these semicircles correspond to grain and electrode response. In addition, the total conductivity is mainly due to grain contribution (intra-grain). However, for LSG-10 (Fig. 4.6b), the capacitance for the higher-frequency semicircle is 0.14 pF, and that for lower frequency semicircle is 0.9 μF. The contribution of grain boundary effect to overall resistance is not resolvable and the bulk resistance (R_b) also reduced as shown in Fig. 4.6. Further, the conductivities of all the samples at different temperatures have been calculated from equation (4.3) as:

$$\sigma = \frac{t}{RA} \qquad (4.3)$$

Where, σ is the conductivity, t is the sample thickness, R is the resistance obtained from Nyquist plots (Fig. 4.2a-b) and A is the electrode area of the pellet. The total electrical conductivity values are calculated using ac impedance spectroscopy and are given in Table 4.4. LSG-10 possessed highest electrical conductivity among synthesized samples. This conductivity value at 800 °C is slightly less than the earlier reported value [17], which could be due to slight porosity and grain agglomeration (Fig. 4.3e-f) in LSG-10. High ionic conductivity of LSG-10 among synthesized samples can be explained on the basis of higher disordered phase formed as indicated by FWHM value (Fig. 4.2).

Table 4.4: Overall conductivity, TEC and activation energy values for LSG samples.

Sample name	**σ × 10^{-4} (S/cm) at 800 ºC**	**TEC × 10^{-6} (/ºC)**	**E_a (eV)**	
		(600-800 ºC)	**(200-400 ºC)**	**(600-800 ºC)**
LSG-0	0.06	9.04	1.42	0.87
LSG-5	0.11	9.44	1.36	0.91
LSG-10	23.70	9.46	1.12	0.81
LSG-15	9.21	8.67	1.10	0.73

Moreover, the activation energy of this sample is slightly decreased (Table 4.4). These effects could be responsible for the improvement of overall conductivity of LSG-10. In addition, Sr-substitution in the parent lattice increases the oxygen vacant sites, which enhance the long-range a.c. conductivity as discussed earlier. So, this composition gives the optimum value of Sr-substitution to get maximum conductivity along with single phase. With further Sr-substitution, the solid solubility gets disturbed, and the secondary phase ($LaSrGa_3O_7$) formation takes place as already discussed in XRD section.

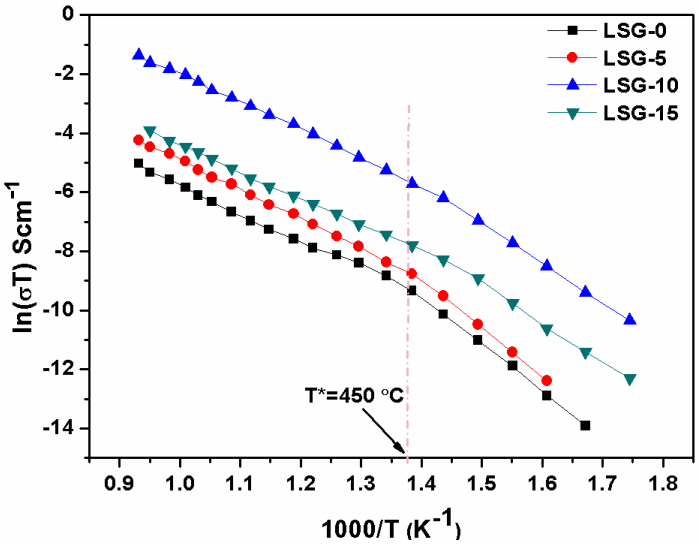

Fig. 4.7: Arrhenius plot of total conductivity for $La_{1-x}Sr_xGaO_{3-\delta}$ system.

This secondary phase hinders the free movement of ions for conduction [18], thus the total conductivity of the sample decreases as given in Table 4.4. Fig. 4.7 shows the Arrhenius plots of the total electrical conductivity ($\sigma_b + \sigma_{gb}$) of the samples. The activation energy (E_a) of the total conductivity (shown in Table 4.4), is calculated using equation 4.4 as:

$$\sigma = \frac{\sigma_0}{T} e^{\frac{-E_a}{k_B T}} \qquad (4.4)$$

Where σ is the ionic conductivity, T is the absolute temperature, σ_0 is pre-exponential term, which is related with the concentration of mobile ions and k_B is Boltzmann's constant. Almost all compositions show the two regions in conductivity plots (Fig. 4.7). It infers that activation energy decreases with increasing temperature. Huang *et al.* [19] reported that the curved behavior might be due to the trapping of oxygen vacancies by the substituted cations or the short range ordering of oxygen vacancies below the critical temperature, and the oxygen vacancies become mobile above the critical temperature [20]. Additionally, below a certain temperature, localization effect is prominent as reported in many disordered metallic systems [21, 22]. Table 4.4 shows the activation energies for the present samples. From the

activation energy values, it is clear that the conductivity in the compound is mainly ionic. Similar variation of activation energies has also been reported in the stabilized zirconia system [12]. Moreover, Anderson *et al.* [18] explained that at the lower temperatures, the activation energy is usually the sum of migration energy (ΔH_m) and an association enthalpy (ΔH_a). However, with increasing temperature, the effect of ΔH_a diminishes due to increase in thermal energy and hence contributes to the curved nature of the activation energy plot (Fig. 4.7).

4.2. $La_{1-x}Ba_xGaO_{3-\delta}$ ($0 \leq x \leq 0.20$) systems:

In the present series, a sequential Ba-substitution and role of secondary phase on ionic conductivity have been investigated in detail. Moreover, a proper co-relation between the morphological features and ionic conductivity of Ba-substituted $LaGaO_3$ electrolyte is studied. This study is important to understand the electrical behavior of substituted $LaGaO_3$ with melilite phase ($LaBaGa_3O_7$).

Ba-substituted lanthanum gallate has been prepared by the solid-state reaction method. The aim is to understand the influence of Ba-substitution on electrical properties and structural morphology of the system. Furthermore, the effect of temperature on conductivity and phase stability has also been investigated.

4.2.1. X-ray diffraction analysis:

Fig. 4.8(a) shows the X-ray diffraction (XRD) pattern of all as-sintered samples. The XRD peaks of Ba-substituted samples are indexed with $LaGaO_3$ (space group *Pbnm*) as a major phase along with $LaBaGa_3O_7$ (ICDD 00-050-1800) as secondary phase. Relative densities of as-sintered samples are summarized in Table 4.5. The relative density of all the samples is more than 90%, which is required for electrolytic applications. The lattice volume and FWHM for $LaGaO_3$ phase are shown in Fig. 4.8(b). The graph indicates an initial increase in lattice parameters with Ba-substitution upto LBG-10. It indicates partial Ba-substitution at La-site in $LaGaO_3$ system. However, higher substitution (LBG-15 and LBG-20) reduces the lattice volume abruptly. It is because Ba-content mainly contributes to $LaBaGa_3O_7$ phase for higher substituted concentration. The decreased FWHM in LBG-5 indicates slight ordering in this sample. However, system becomes more disordered $x \geq 0.10$. Moreover, the structural reports on substituted lanthanum gallate are contradicting [17, 23, 24]. According to Feng and Goodenough [23] Sr- and Mg- substituted lanthanum gallate form cubic unit cell, whereas, the investigations by other groups [17, 24] indicate that system is orthorhombic with a space

group *Pbnm*. However, in this study, some of the reflections, e.g., (120) and (210) coming from *Pbnm* were absent, so to reconfirm the phase formed, the Rietveld refinement of selected samples (x=0.0 and x=0.15) is performed as shown in Fig. 4.9(a-b). It has been observed that the Ba-substituted samples are body centered orthorhombic with a space group *Ibmm* and the refined structural parameters are given in Table 4.6. Kajitani *et al.* [25] reported that $LaGa_{0.8}Mg_{0.2}O_{2.9}$ also crystallized in the orthorhombic phase (*Ibmm*) at room temperature, which is in agreement with our work. Furthermore, a limited solid solubility of Ba in $LaGaO_3$ is observed.

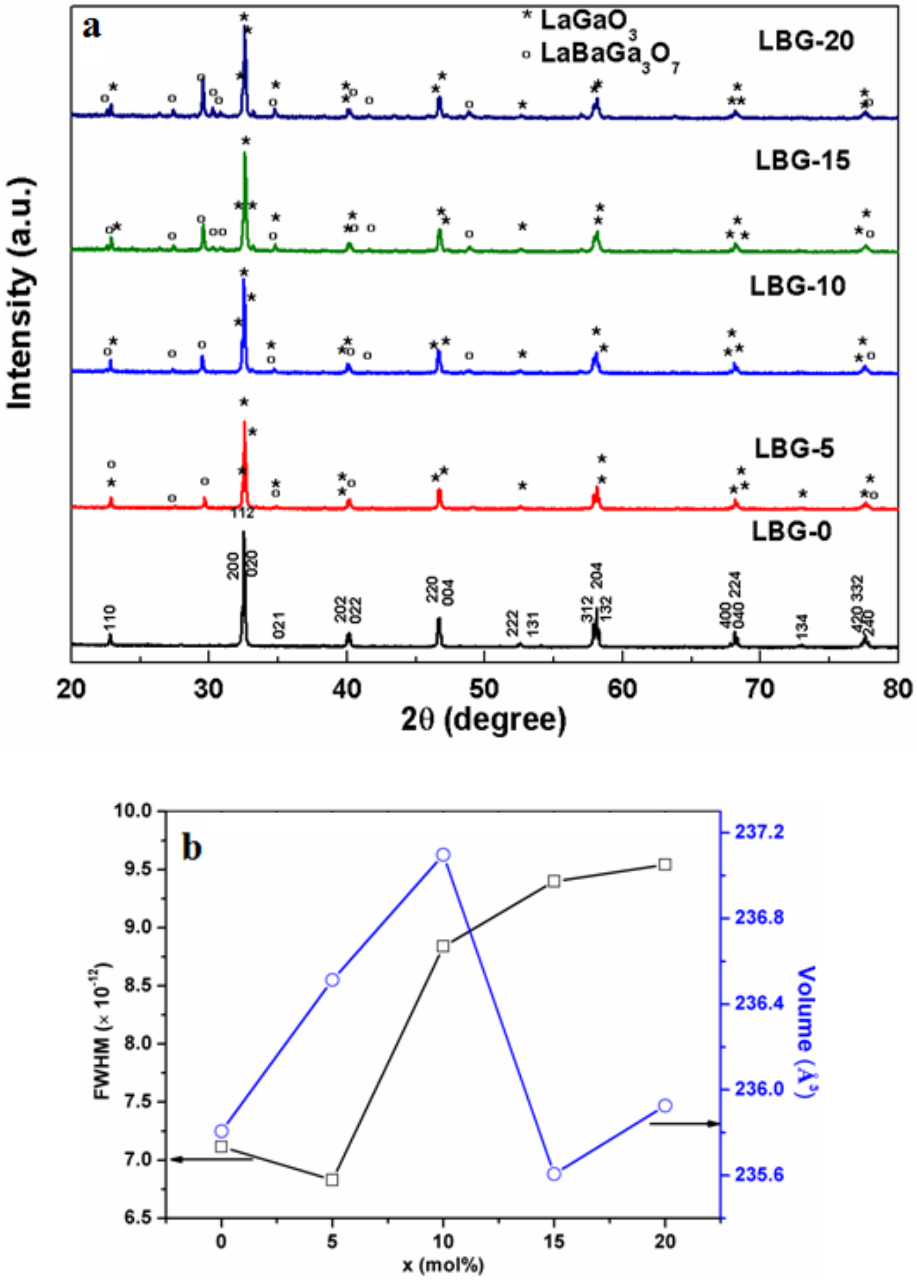

Fig. 4.8: (a) X-ray diffraction pattern of the as-sintered LBG samples and **(b)** FWHM at (112) plane and lattice volume variation with composition.

For x=0.15, besides secondary phase ($LaBaGa_3O_7$), best fitting is obtained when the XRD pattern was refined with two $LaGaO_3$ phases co-existing as orthorhombic and rhombohedral phases (Fig. 4.9b). The formation of orthorhombic phase of $LaGaO_3$ is reported in the literature [17, 24]. However, $LaGaO_3$ as rhombohedral phase is not reported very commonly.

Table 4.5: Relative density, strain and volume fraction values for as-sintered LBG samples.

Sample name	Relative density (%)	Strain for $LaGaO_3$ ($\times10^{-4}$)	Strain for $LaBaGa_3O_7$ ($\times10^{-5}$)	Volume fraction $LaGaO_3$	$LaBaGa_3O_7$	Tolerance factor (t)
LBG-0	95	3.6	-------	100	0.00	0.966
LBG-5	90	12.5	1.49	86.5	13.5	0.971
LBG-10	92	22.3	-0.22	72.5	27.5	0.975
LBG-15	94	22.3	-0.21	67.4	32.6	0.979
LBG-20	95	35.8	-7.62	58.7	41.3	0.984

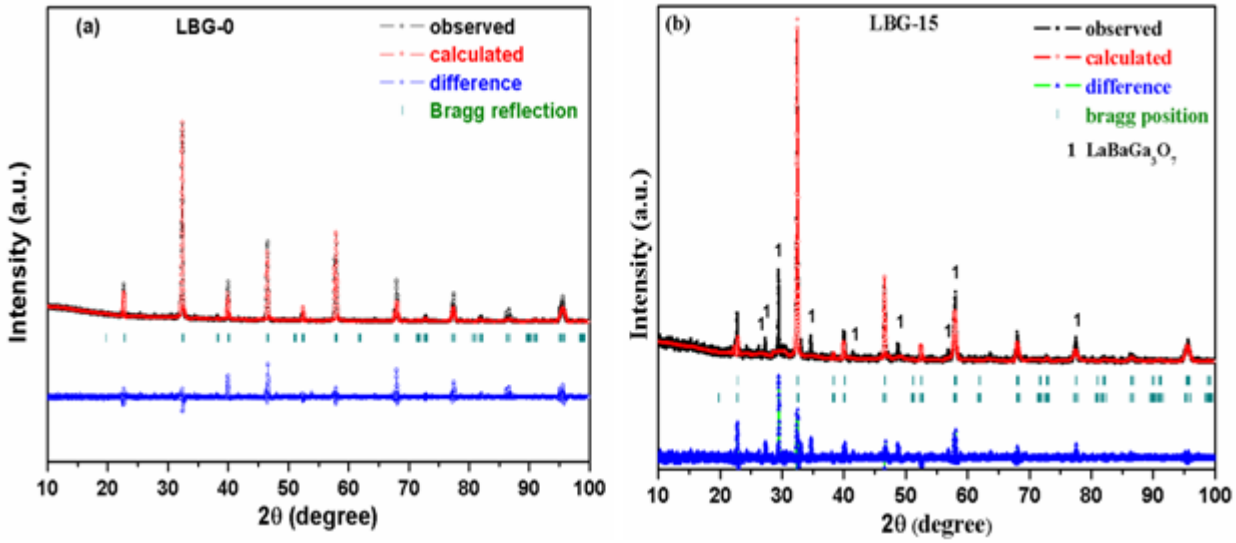

Fig. 4.9: Rietveld refinement of (a) $LaGaO_3$ (b) $La_{0.85}Ba_{0.15}GaO_{3-\delta}$ system.

The disordered rhombohedral phase so formed could be due to partial substitution of Ba^{2+} at La-site in $LaGaO_3$ (in the ratio 1:10 with orthorhombic phase). The formation of a mixture of orthorhombic and rhombohedral phases for similar system ($La_{0.8}Sr_{0.2}Ga_{0.9}Mg_{0.1}O_3$, $La_{0.85}Sr_{0.15}Ga_{0.85}Mg_{0.15}O_3$ and $La_{0.9}Sr_{0.1}Ga_{0.8}Mg_{0.2}O_3$) is reported by Datta *et al.* [1]. Moreover, it is reported that increasing tolerance factor (t) can transform orthorhombic ($LaGaO_3$) to rhombohedral ($LaGaO_3$) phase, and the boundary between these two phases is near t=0.985 [26, 27]. In the present study, the substitution of Ba^{2+} (r=1.61Å) at La^{3+} (r=1.36 Å) site in $La_{1-x}Ba_xGaO_3$ system increases the tolerance factor (Table 4.6) and approaches the earlier reported value (t=0.985) [26, 27].

Table 4.6: Refined structural parameters for LBG-0 and LBG-15.

	LBG-0	**LBG-15**	
Structure	Orthorhombic	Orthorhombic	Rhombohedral
Space group	Ibmm	Ibmm	$R\bar{3}c$
***a*(Å)**	5.4461(20)	4.6949(16)	5.5057(3)
***b*(Å)**	5.5273(3)	6.1549(3)	7.8678(4)
***c*(Å)**	7.7790(4)	7.8678(4)	13.5440(4)
***V*(Å^3)**	236.32	227.35	586.69
La/Ba			
g	1.0	0.85/0.15	0.85/0.15
x	0.5074	0.4945	0.0
y	0.0	0.0	0.0
z	0.7500	0.7500	0.2500
Ga			
g	1.0	1.0	1.0
x	0.0	0.0	0.0
y	0.0	0.0	0.0
z	0.0	0.0	0.0
O1			
g	1.5	1.5	3.0
x	-0.0913	0.0732	0.9652
y	0.0	0.0	0.5384
z	0.2500	0.2500	0.0
O2			
g	1.5	1.5	_____
x	0.7919	0.7500	_____
y	0.2084	0.2500	_____
z	0.0143	0.0261	_____

Furthermore, the formation of rhombohedral phase could be responsible for the increase in ionic conductivity of the system as discussed in conductivity section. These results are also confirmed by TEC measurements as discussed in the respective section. The volume fraction of the formed phases has been calculated using direct comparision method by integrating the area of selective XRD peaks (2θ=29.8° and 32.6°) for respective phases, and results are summarized in Table 4.5. These results indicate that Ba-substitution in perovskite system enhances the formation of secondary phase ($LaBaGa_3O_7$) over $LaGaO_3$. The formed secondary phase ($LaBaGa_3O_7$) possesses a melilite type structure. A similar melilite phase ($La_{1.54}Sr_{0.46}Ga_3O_{7.27}$) has been recently reported as high oxide ionic conducting phase and most suitable as the oxide-ion electrolyte for SOFCs [28, 29]. The theoretical densities of $LaGaO_3$ and $LaBaGa_3O_7$ phases are 7.23 and 5.60 g/cm^3, respectively. The theoretical density for the mixed phase has been calculated using following equation [30].

$$\rho = v_1\rho_1 + v_2\rho_2 \qquad (4.5)$$

Where, v_1 and v_2 are volume fractions of each component with theoretical densities of ρ_1 and ρ_2 respectively. The achieved density of all synthesized samples is more than 90% of theoretical density. Furthermore, the incorporation of Ba at *A*-site in $La_{1-x}Ba_xGaO_{3-\delta}$ system introduces microstrain in the system, which was calculated using Williamson-Hall's equation (4.1). Strain in $LaGaO_3$ increases with increasing Ba-substitution in the present series as given in Table 4.5. It further indicates the partial Ba-substitution in $LaGaO_3$ lattice. Moreover, the strain value abruptly increased for 10 mol% Ba content. This variation could be due to the stabilization of rhombohedral phase as discussed in TEC section.

4.2.2. Microstructural analysis:

Microstructural study was carried out to find the porosity, shape and size of the grains [Fig. 4.10(a-g)]. The dense packing has been observed in all the micrographs. The average grain size of LBG-0 is of the order of 9 µm. With Ba-substitution, the average grain size gets reduced to 1.1 µm. For LBG-5, the presence of secondary phase is not so pronounced, but pores are visible, which indicates lower density of the sample. For $x \geq 0.10$, two distinct grains, corresponding to two phases can be clearly seen. Grain size distribution with composition is shown in Fig. 4.10(h). The decreased grain size in substituted samples is due to the property of alkaline earth metals that provide a large number of nucleating sites and lead to reduced grain size [9]. However, with higher Ba-substitution, marginal grain size variation is observed. It is due to the multiple phase formation in these samples as explained

in XRD analysis. For LBG-10, the EDS analysis at two different points (Fig. 4.10c, Table 4.7) reconfirms the presence of two phases as discussed in XRD section. The atomic weight percent obtained at these points are given in Table 4.7. It gives the qualitative idea about phases formed in this sample. Moreover, from the micrographs, it is observed that the grain growth of secondary phase increases with Ba-substitution, which is in accordance with the volume fraction calculated from the XRD pattern (Table 4.5).

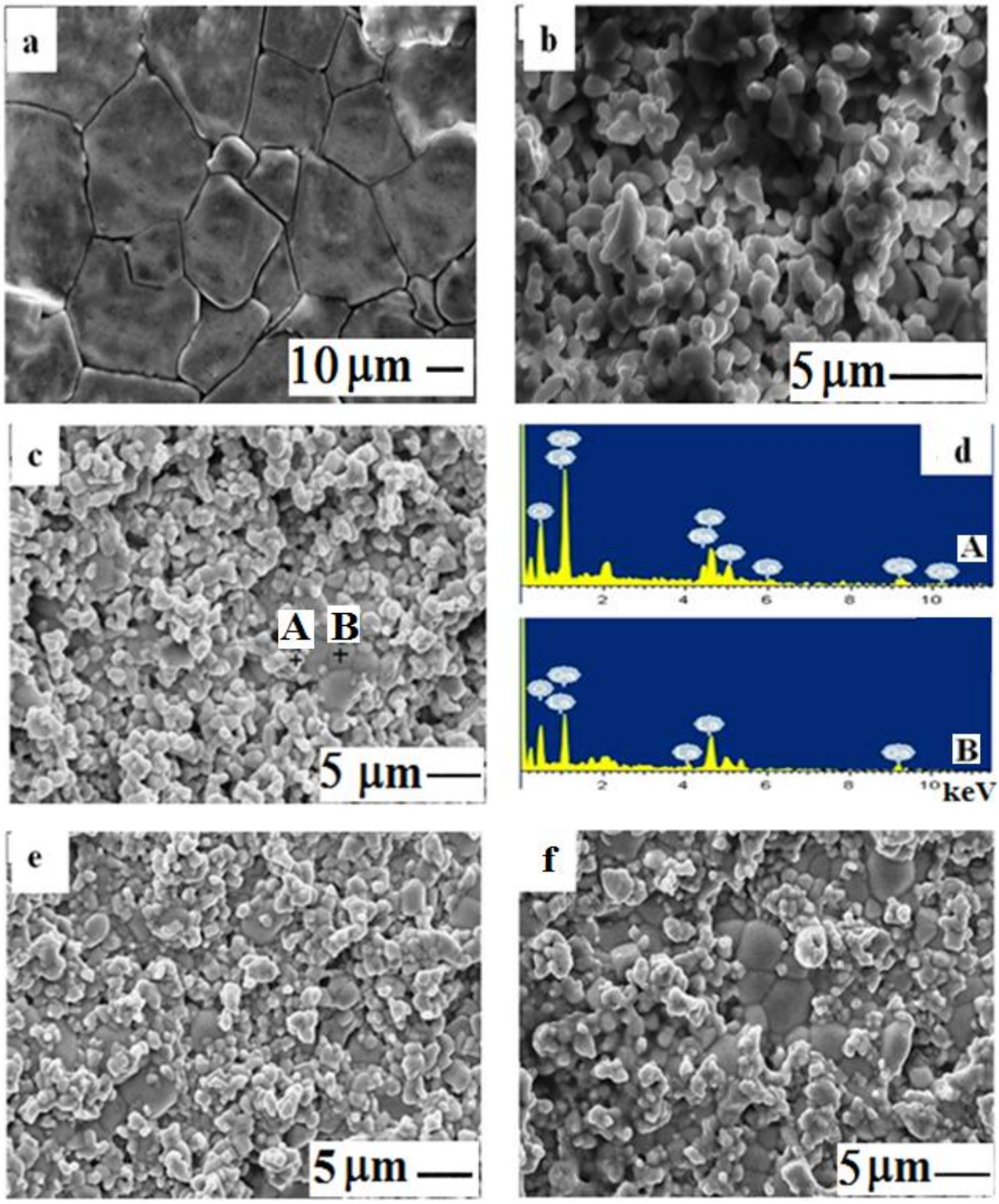

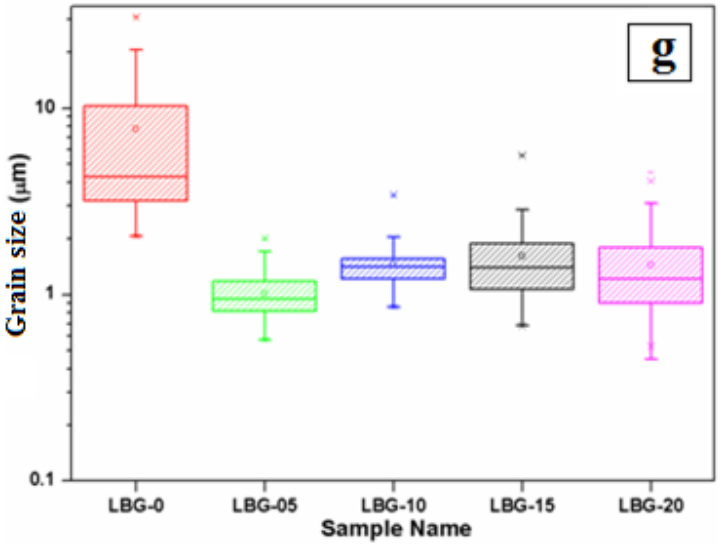

Fig. 4.10: SEM/EDS micrographs of as-sintered samples (a) LBG-0, (b) LBG-5, (c) LBG-10, (d) EDS spectrum of LBG-10, (e) LBG-15, (f) LBG-20 and (g) grain size distribution.

Table 4.7: EDS analysis of LBG-10 sample at two different grains.

Element (Wt%) → / Spot ↓	La	Ba	Ga	O
At A	58.44	0	27.83	13.73
At B	31.87	25.58	26.51	16.04

4.2.3. TEC analysis:

Fig. 4.11 shows the dilatometric studies of the sintered samples. In LBG-0, the sharp kink at temperature ~148 °C is for phase transition from orthorhombic to rhombohedral phase [9, 11, 26]. Furthermore, with Ba-substitution, the transition temperature is slightly decreased, which is in accordance with earlier reported work [11]. Moreover, it is observed that the sharpness in the kink decreases with Ba-substitution in the system. It might be due to the increased disordering with increasing Ba-substitution. It further indicates the stabilization of more disordered rhombohedral phase at room temperature. These results are in accordance with the Rietveld refinement of the LBG-15 system. TEC of all the samples is given in Table 4.8. It is observed that TEC from 600 to 800 °C is almost uniform in all the compositions except LBG-0. Furthermore, Ba-content increased the TEC partially. Apart from this, the slope changes at T^* in the range of 570-670 °C (Fig. 4.11). This change in slope may be due to the prominent effect of order disorder transition or phase transition, which is well reported in literature [26, 15, 31].

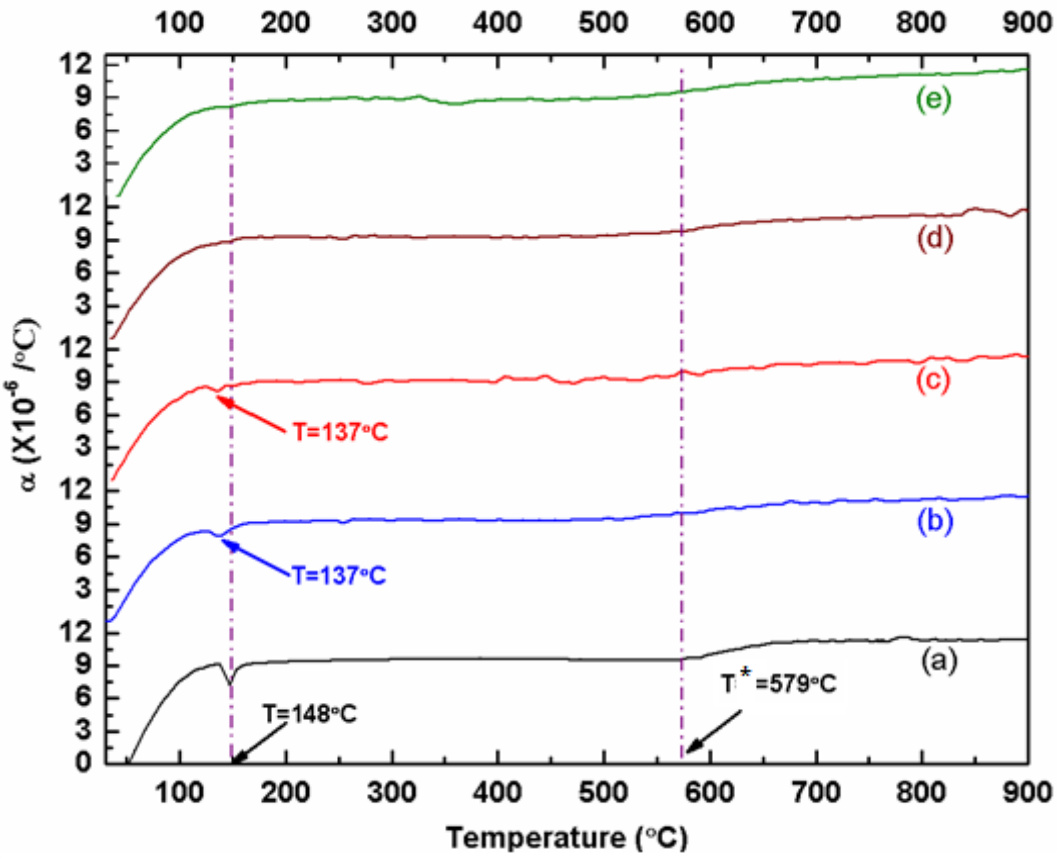

Fig. 4.11: Thermal expansion coefficient of LBG samples (a) LBG-0, (b) LBG-5, (c) LBG-10, (d) LBG-15 & (e) LBG-20.

4.2.4. TGA analysis:

The TGA analysis of the as-sintered samples (from room temperature to 1000 °C) is done in N_2 atmosphere. Fig. 4.12 represents the TGA results for heating cycle. For LBG-0, the obvious weight loss (~1.0%) up to 300 °C is due to loss of absorbed water as reported in literature [15]. The weight loss from 300 to 1000 °C which is ~0.3% could be due to loss of lattice oxygen with increasing temperature. For LBG-5, the overall weight loss up to 1000 °C is ~0.5%. The initial weight loss is less than unsubstituted sample (LBG-0), and seems to be more stable in N_2 atmosphere. Furthermore, the effect of secondary phase for LBG-5 is less due to lower volume fraction (Table 4.5). For LBG-10, there is an initial weight loss up to *T*~110°C, above which there is uniform weight gain throughout the investigated temperature range. The observed weight gain (~2.6%) from 110 to 1000 °C indicated the absorption of oxygen by oxygen deficient perovskite phase ($La_{1-x}Ba_xGaO_{3-\delta}$) from the N_2 as residual oxygen is always present in commercially available N_2. The maximum weight gain in LBG-10 could be due to presence of higher oxygen vacancies in LBG-10 sample [33]. However, in

case of LBG-15 and LBG-20, the average weight gain decreases. It is due to decreasing volume fraction of perovskite phase and hence lesser oxygen vacancies in this sample. Also, the porosity affects the weight change due to the H_2O adsorption on the porous sites of this type of perovskite system, which is also reported in literature [34, 35].

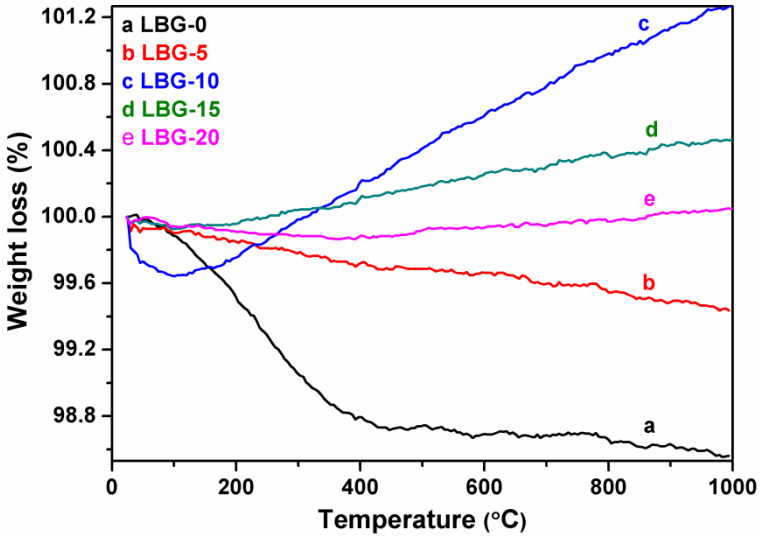

Fig. 4.12: TGA plots of LBG samples in N_2 atmosphere.

4.2.5. Impedance analysis:

Nyquist plots of the sintered LBG samples, at 450 ºC in air are shown in Fig. 4.13(a-b). The plots mainly consist of two well defined semicircular arcs. It is a well-known fact that with decreasing frequencies, contribution of bulk, grain boundary and electrode polarization appear, as is clear from Fig. 4.13. Such complete semicircle appears only in a narrow temperature range.

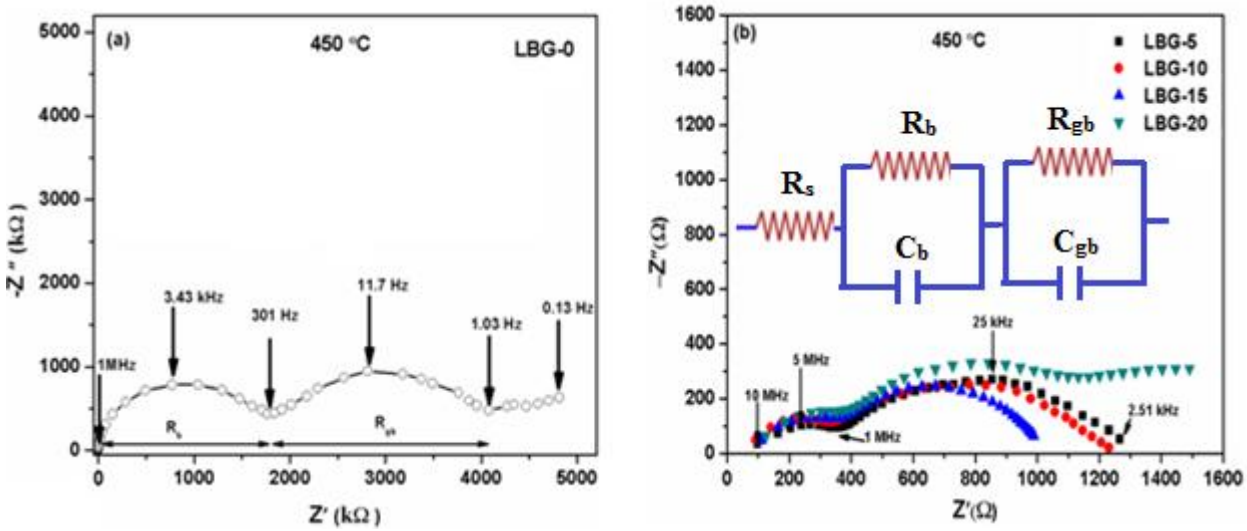

Fig. 4.13: Nyquist plot of (a) LBG-0 sample and (b) LBG-5, 10, 15 & 20 samples.

At the higher temperatures (600-900ºC), the relaxation frequency of bulk response is too high to be measured using conventional instrument. Furthermore, at the lower temperatures (<150ºC), the bulk impedance is too high and only a small portion of the semicircular plot is observed [36]. The relaxation time for the oxide ion transfer through bulk, grain boundary and electrode interface should be well separated and hence distinct arcs for each process at 450°C is observed in Fig. 4.13(a-b). Fig. 4.13a indicates the well separated bulk, grain boundary and electrode response of unsubstituted sample. However, for substituted samples, the impedance spectrum (Fig. 4.13b) indicates that the bulk resistance hardly depends on Ba-content. It means that increasing Ba-substitution has less effect on bulk conductivity of the system. However, the grain boundary contribution is higher in the overall resistance of the samples. It may be because of the large grain boundary area which leads to higher contribution in the overall conductivity of the system. Moreover, with Ba-substitution, the grain boundary resistance initially decreases up to LBG-15. It may be because of the formation of more disordered rhombohedral phase (as discussed in Rietveld analysis) that has segregated along grain boundaries and could enhance the overall conductivity of the system. The equivalent circuit diagram separating the bulk and grain boundary response is represented by a series of parallel resister-capacitor (*R*-*C*) elements, is shown in the inset of Fig. 4.13(b).The fitted values for LBG system at 450 °C are given in Table 4.9. These values indicate that except LBG-0, all the samples possessed higher grain boundary resistance (R_{gb}) than bulk resistance (R_b). Further, the conductivities of all the samples at different temperatures have been calculated using equation (4.2). The values so obtained are given in Table 4.8. LBG-15 exhibited the highest ionic conductivity among all the synthesized samples. However, for LBG-20, the total conductivity is slightly decreased. It could be due to the effect of the higher volume fractions of melilite phase ($LaBaGa_3O_7$), which might segregate along grain boundary and decrease the overall conductivity of LBG-20 [37]. So, LBG-15 could be the optimum substitution for achieving better electrolyte system. Fig. 4.14 represents the Arrhenius plots of the total conductivity in air for LBG samples. The activation energy (E_a) of the total conductivity (shown in Table 4.8), is calculated using equation 4.3. The activation energy values (Table 4.8) indicate that the conductivity is mainly due to the oxide-ion hopping mechanism in the investigated samples. Arrhenius plots exhibit two linear regions with a slope change within 500-600 ºC. This transition temperature is consistent with the slope change at *T**, as shown in TEC analysis (Fig. 4.11). This change of slope could be due to ordering-disordering vacancy clusters or due to phase transition [15, 39-40].

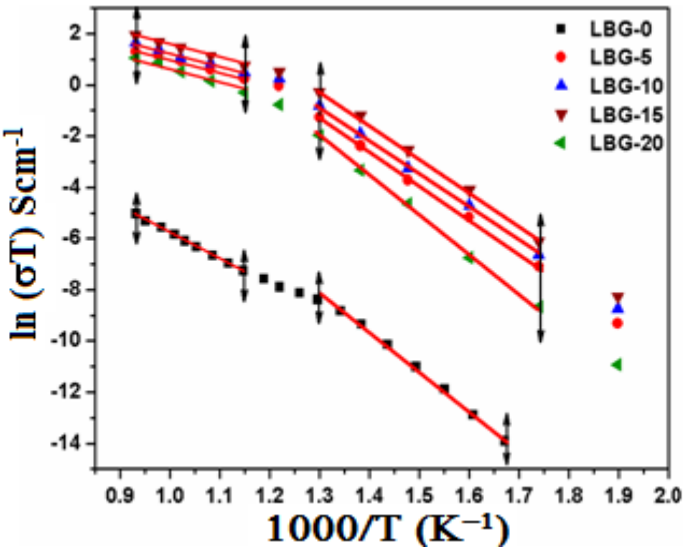

Fig. 4.14: Arrhenius plots of LBG samples.

Table 4.8: Conductivity and activation energy of as-sintered LBG samples.

Sample name	σ (mS/cm) at 800 ºC	E_a (eV) (600-800 ºC)	$TEC \times 10^{-6}$ (/°C) (600-800 °C)
LBG-0	0.006	0.87	9.72
LBG-5	3.35	0.62	10.9
LBG-10	4.61	0.65	10.6
LBG-15	5.99	0.66	10.8
LBG-20	2.35	0.63	10.7

Table 4.9: Fitting parameters for LBG samples at 450 °C: bulk resistance R_b, bulk capacitance C_b, *GB* resistance R_{gb} and *GB* capacitance C_{gb}.

Sample name	R_s (Ω)	R_b (Ω)	R_{gb} (Ω)	C_b (F) $\times 10^{-11}$	C_{gb} (F) $\times 10^{-9}$
LBG-0	154.0	1.8×10^6	2.3×10^6	2.6	59.0
LBG-5	96.0	265.0	911.0	15.0	69.0
LBG-10	88.0	257.0	891.0	15.0	45.0
LBG-15	80.0	254.0	634.0	15.0	25.0
LBG-20	90.0	256.0	773.0	15.0	20.5

Accordingly, the activation energy (E_{grain}) at the higher temperatures (>570ºC) is the migration energy ($E_{grain,m}$), while at the lower temperatures (<500 ºC), it is the sum of the

migration ($E_{grain,m}$) and the association energy ($E_{grain,a}$). Here, $E_{grain,m}$ is ~0.65eV, which is close to the earlier reported values (0.6-0.7eV) for the oxide ion conduction through a hopping mechanism [20, 33, 40]. Moreover, it is reported that Ba-substitution can promote water incorporation and related to protonic conductivity in the substituted lanthanum gallate system [37]. So, the slight change in slope could be due to uncontrolled changes in air humidity under measurement.

4.3. $La_{1-x}Ca_xGaO_{3-\delta}$ ($0 \leq x \leq 0.20$) systems:

The effects of Ca-substitution at La-site of $LaGaO_3$ on crystal structure, ionic conductivity, lattice expansion and microstructure have not been explored much. In this work, Ca-substituted $LaGaO_3$ has been thoroughly investigated. Also, the solid solubility, optical band gap study, Urbach energy and morphological features of substituted system have been reported.

4.3.1. X-ray diffraction analysis:

X-ray diffraction patterns of the synthesized samples are presented in Fig. 4.15 (a-b). All peaks of unsubstituted sample were matched with $LaGaO_3$ perovskite phase (ICDD no. 089-01-7833). The solid solubility limit is achieved upto 10 mol%, above which secondary phase ($LaCaGa_3O_7$) formation takes place (Fig. 4.15a-b). Also, uniform XRD peak shifting towards the higher angle (2θ) with substitution is observed. This shifting could be due to the uniform strain in the synthesized system with Ca-substitution. The lattice parameters and relative density of these samples are given in Table 4.10. The density of as-sintered samples is more than 90% of theoretical density, which is essential for electrolyte applications.

The variation of lattice volume with composition is shown in Fig. 4.15(c). The lattice volume initially decreases upto LCG-10, and becomes constant for LCG-15 and LCG-20. This decrease of lattice volume is due to ionic radii mismatch between host cation, La^{3+} (r_{XII} =1.36Å) and substituted ion, Ca^{2+} (r_{XII} =1.34Å). Moreover, with higher substitution, (LCG-15 and LCG-20), the behavior is according to Vigard's law. According to it, the lattice parameters change untill the solid solubility limit is not achieved and become invariant with the formation of secondary phases [2]. Moreover, Ca-substituted samples possess higher FWHM value in comparison to unsubstituted sample (Fig. 4.15c). It indicated high disorderness in Ca-substituted system. Fig. 4.15(b) indicates the changes observed in (200) and (020) planes with Ca-substitution. It is observed that the peaks corresponding to these planes are sharp in the unsubstituted sample; however, with substitution, both the reflections

diminished. This effect can be explained on the basis of vacancy formation in the oxygen deficient perovskite unit-cell as shown in Fig. 4.16. The Ca-substitution at La-site introduces the oxygen vacancies, which occupy one of the face centre positions as shown in Fig. 4.16. These oxygen vacancies so formed affect the reflection from the planes associated with oxygen sites for $LaInO_3$ system [41]. Since (200) and (020) planes are directly affected with the formation of vacant sites, so, the reflection from these planes would not be sharp as observed in Fig. 4.15(b).

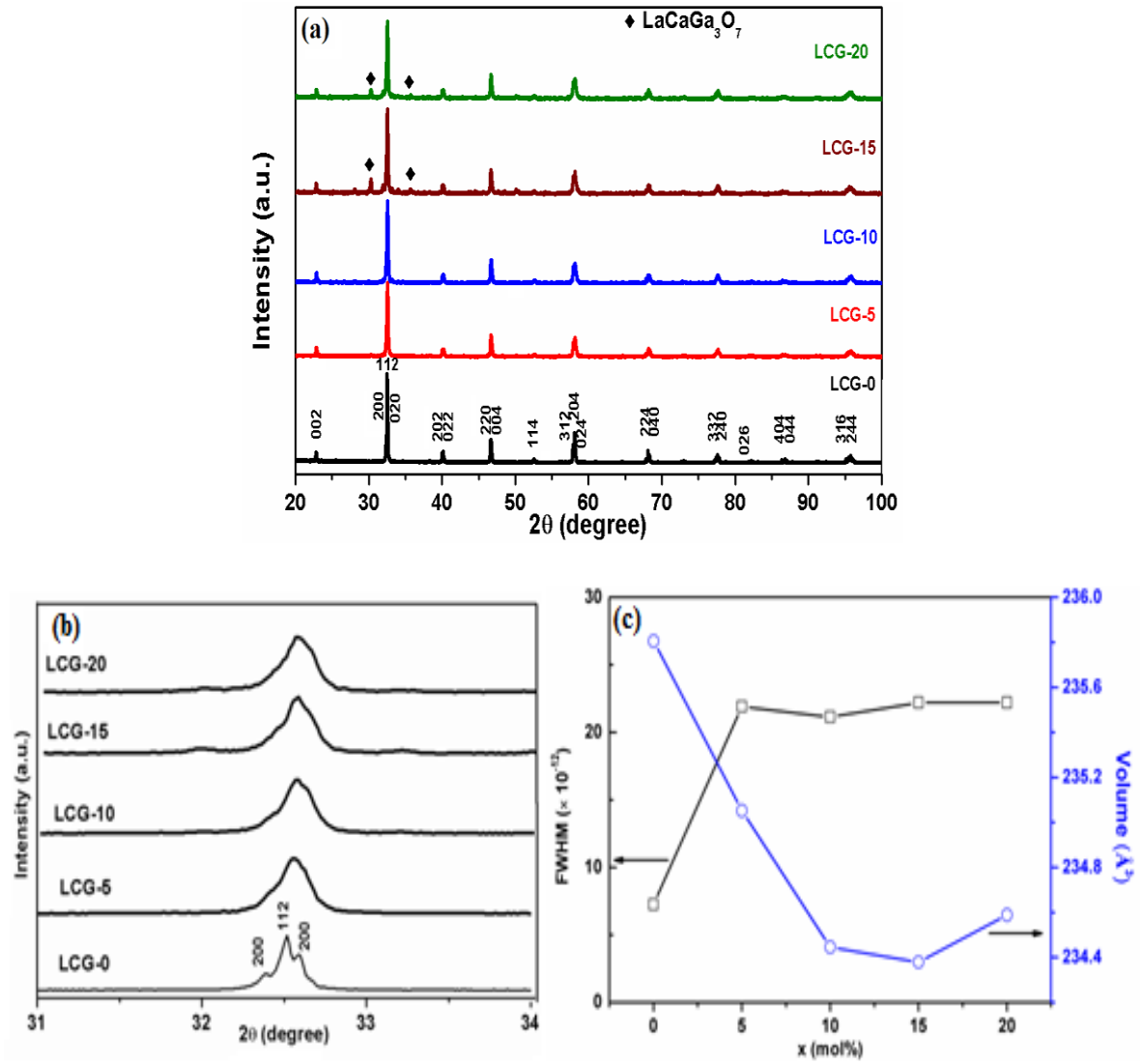

Fig. 4.15: (a) X-ray diffraction pattern of $La_{1-x}Ca_xGaO_{3-\delta}$ at ×=0, 0.05, 0.10, 0.15 and 0.20, (b) Magnified view of (200), (112) and (020) planes of $La_{1-x}Ca_xGaO_{3-\delta}$ system and (c) FWHM and lattice volume with composition.

Also, these oxygen vacancies are helpful for ion-hopping mechanism, which is discussed in conductivity section. Furthermore, the incorporation of Ca-content in $LaGaO_3$ introduces strain in the system, which is calculated using Williamson-Hall's equation (4.1). The strain

for these samples is given in Table 4.10. It indicates that higher Ca-substitution increases strain in these samples.

Table 4.10: Lattice parameters, density and strain of as-sintered LCG samples.

Sample name	a (Å)	b (Å)	c (Å)	V (Å^3)	Relative density (%)	Strain (ϵ) $\times 10^{-4}$
LCG-0	5.5223	5.4934	7.7731	235.8063	95	3.6
LCG-5	5.5182	5.4852	7.7656	235.0525	93	15.8
LCG-10	5.5120	5.4806	7.7608	234.4465	94	26.8
LCG-15	5.5110	5.4820	7.7580	234.3793	95	27.9
LCG-20	5.5112	5.4860	7.7590	234.5890	91	33.0

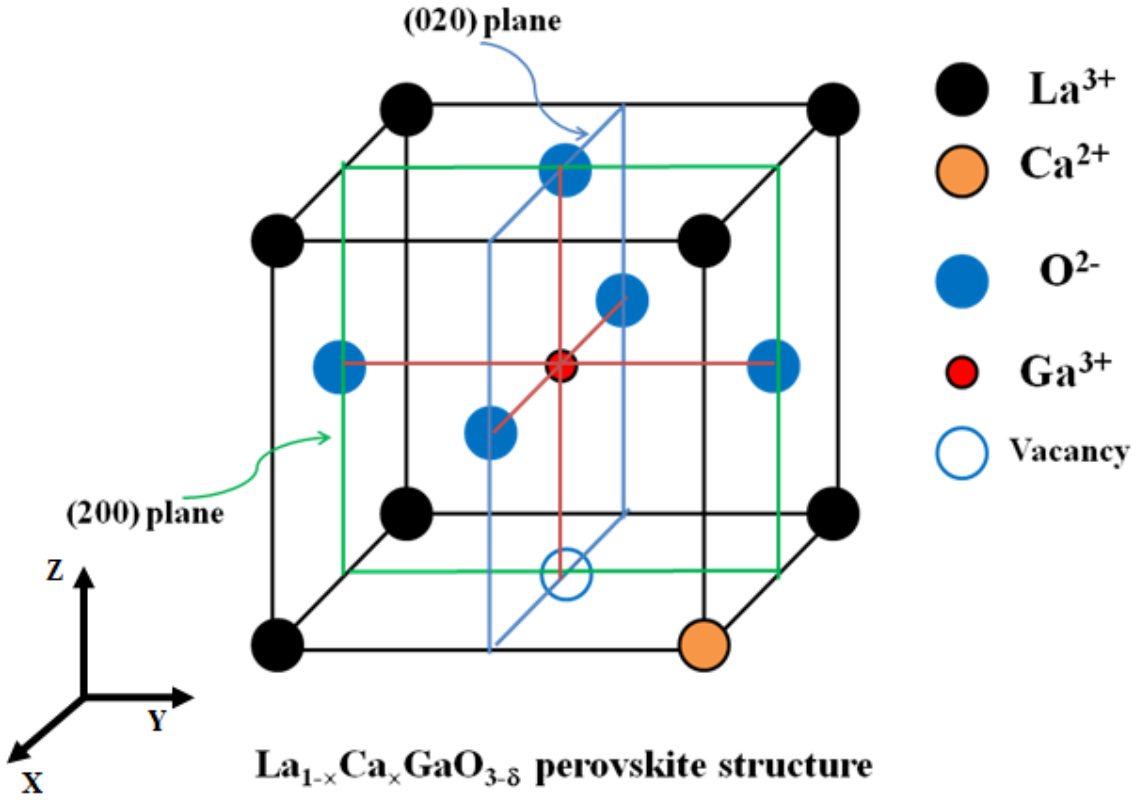

Fig. 4.16: The oxygen deficient $La_{1-x}Ca_xGaO_{3-\delta}$ perovskite structure.

This strain is mainly due to the cation size mismatch between substitution (Ca^{2+}) and host ion (La^{3+}). The idea of the disordering/defects and oxygen vacancies in a system can be estimated by optical analysis, particularly, Urbach energy.

4.3.2. Optical analysis:

The UV-vis diffuse reflectance spectra of the as-sintered samples are shown in Fig. 4.17. The optical absorption behavior is sensitive to the type of substitution and its amount in $LaGaO_3$

system. The value of the band gap decreases with substitution concentration in the present system. This change in the band gap is attributed to the structural changes due to Ca^{2+} substitution and generation of oxygen vacancies [42, 43]. Moreover, the generation of defects also led to decrease in the band gap [44]. Additionally, there is a slight electronegativity difference between Ca (1.0) and La (1.1). This difference in the electronegativity value may shift valence band towards the conduction band [45] and lead to decrease in the band gap with substitution. Fig. 4.17 shows the exponential increase in the absorption coefficient which was first explained by Urbach in his work on AgBr crystal [46].

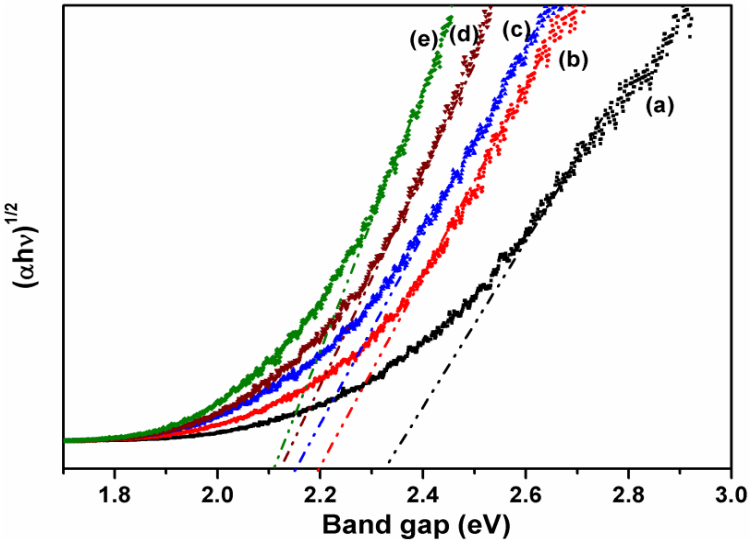

Fig. 4.17: Plot of $(\alpha h\nu)^{1/n}$ versus hν for the calculation of band gap (in eV) where (a) LCG-0, (b) LCG-5, (c) LCG-10, (d) LCG-15 and (e) LCG-20.

Table 4.11: Band gap, Urbach energy, and TEC of LCG samples.

Sample name	**Optical band gap (eV)**	**Urbach energy (eV)**	**TEC×10^6 (/°C) 600-800 °C**
LCG-0	2.33	0.204	9.04
LCG-5	2.20	0.224	8.86
LCG-10	2.15	0.268	8.56
LCG-15	2.12	0.249	8.82
LCG-20	2.11	0.249	9.01

According to Urbach, the dependence of an absorption coefficient on the photon energy and temperature is given by following equation:

$$\alpha(h\nu, T) = \alpha_0 \exp\left[\frac{h\nu - E_0}{E_U(T)}\right] \quad (4.6)$$

where, E_U is the Urbach energy, which is dependent on the absorption edge energy width (Fig. 4.17) and is calculated by following equation:

$$E_U^{-1} = \frac{\Delta(ln\alpha)}{\Delta(h\nu)} \quad (4.7)$$

In the present work, E_U increases uniformly with Ca-substitution up to LCG-10. However, with higher substitution (LCG-15 and LCG-20), E_U is slightly decreased (Table 4.12). It is well reported that E_U indicates the extent of disordering caused by structural, temperature and other external features of the samples [47]. Therefore, in the present study, the increase in Urbach energy with substitution (up to solid solubility limit) is due to increase in structural disorder, particularly oxygen vacancies created to maintain the charge neutrality of the system with Ca-substitution. However, with higher substitution (LCG-15 and LCG-20), the secondary phase gets formed, which prevent further disorderness in the parent phase. In addition, the structural disordering arises mainly due to intrinsic as well as extrinsic defects, such as vacancies, dislocations, non-stoichiometry, substitution [48-51] etc. This feature further supports our XRD results.

4.3.3. Microstructural analysis:

The micrographs of the selective as-sintered samples are shown in Fig. 4.18(a-d). These micrographs indicate the formation of densely packed grains. As compared to unsubstituted sample (LCG-0), the grain size reduced drastically with Ca-substitution [Fig. 4.18(a-b)]. Also, the shape of grains of substituted samples varies significantly as compared to unsubstituted sample (LCG-0). Moreover, the microstructures confirm that among substituted samples, higher Ca-content promotes better grain growth, and separation of well defined grain boundaries. In LCG-5, the grains are uniformly distributed, and the average grain size is ~1 μm. The grains are well intact with slight porosity. For LCG-20, the average grain size is 2 μm. Moreover, in this sample the morphology is composed of large grains surrounded by small grains. These two different grains might represent two different phases as discussed in XRD section. This feature may enhance the porosity in the sample. Grain size distributions with compositions are shown in Fig. 4.18(d). It is clear that average grain size of substituted

samples is less than unsubstituted sample. However, increase in Ca-content enhances the average grain size in substituted samples. This phenomenon can be explained on the basis of liquid phase sintering, which may enhance the grain growth with substitution concentration.

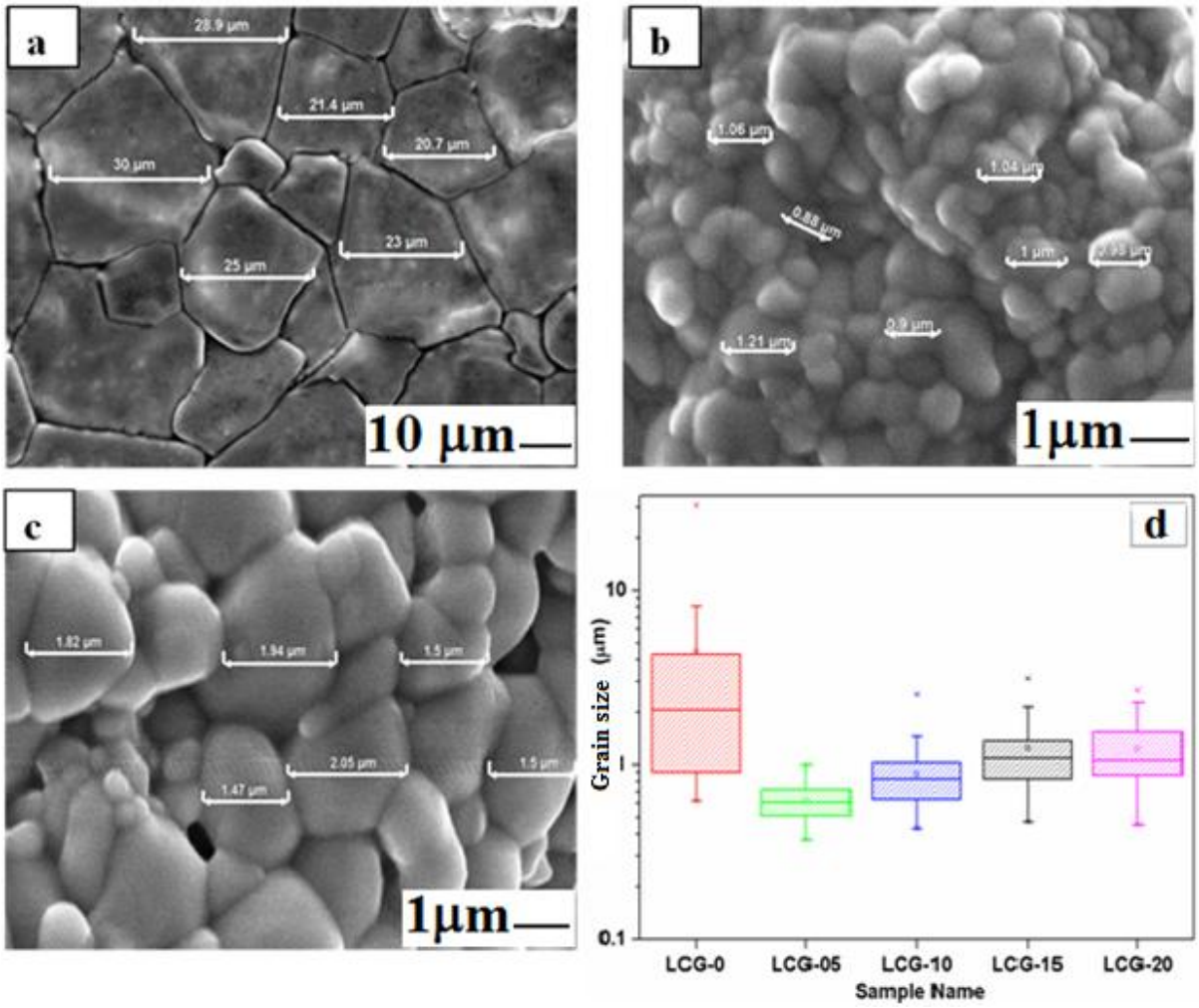

Fig. 4.18: The SEM micrographs of (a) LCG-0, (b) LCG-5, (c) LCG-20 and (d) grain size distribution.

4.3.4. TEC analysis:

Thermal expansion for a given system is small for strongly bonded materials in comparison to weekly bonded materials. Thermal expansion coefficients of the as-sintered samples were measured from room temperature to 1000 °C in air and shown in Fig. 4.19. The TEC value for unsubstituted sample (LCG-0) is similar to earlier reported value [11]. In addition, it is observed that the TEC values decrease with Ca-substitution upto LCG-10. The substitution in the present system causes two-fold effects; firstly, the formation of oxygen vacancies due to aliovalent ion substitution and secondly, the increase in bond strength between the substitution (Ca^{2+}) and the cation (O^{2-}).

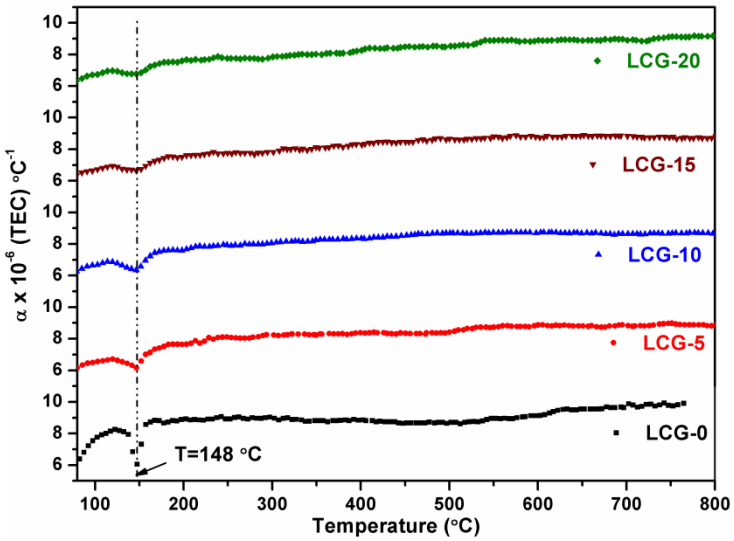

Fig. 4.19: The differential of lattice expansion coefficient with temperature in air.

The oxygen vacancies lead to weakening of lattice bonding, which may increase the TEC of the system [52]. However, the substitution of Ca-ion at La-site may increase the cation-anion bond strength due to smaller ionic radii and higher electronegativity value of Ca as compared to La, which results in decrease of overall TEC values. Therefore, in the present samples, the dominating factor is the second one. Moreover, TEC values are also affected with the presence of secondary phase ($LaCaGa_3O_7$). Higher TEC values of mixed phase could be due to the effect of secondary melilite phase ($LaCaGa_3O_7$), which may lead to increase the overall lattice expansion.

On the other hand, for LCG-0, the sharp kink at 148 °C is well reported phase transition from orthorhombic to rhombohedral [9, 11, 26]. In addition, the increasing Ca-content led to an increase in broadness in this kink. This change in sharpness might be attributed due to increased disordering with increasing Ca-substitution as discussed in UV-section.

4.3.5. TGA analysis:

Fig. 4.20 shows the TGA graphs of as-sintered samples in N_2 atmosphere. From these graphs, the weight loss is maximum (0.8% loss up to 1000 C) for unsubstituted sample (LCG-0) in the studied samples. However, marginal weight loss is observed for Ca-substituted samples. The weight loss up to 300 °C is mainly attributed due to hygroscopic nature of these samples [15]. It indicated that Ca-substitution in this series promoted the stability of these samples in the inert atmosphere. Among substituted samples, LCG-10 exhibits higher weight loss (0.5% loss up to 1000 C). This marginal weight loss could be due to the loss of lattice oxygen at temperature range.

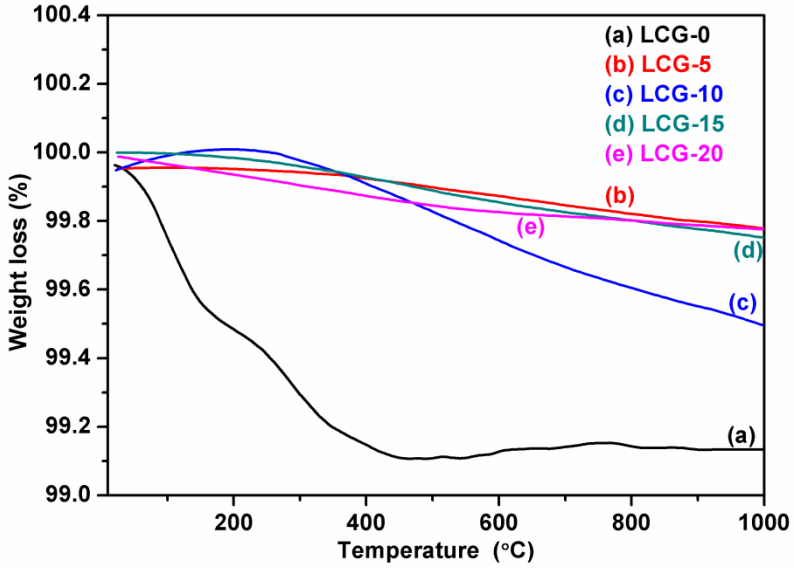

Fig. 4.20: TGA for $La_{1-x}Ca_xGaO_{3-\delta}$ system in N_2.

4.3.6. Impedance analysis:

The contribution of bulk, grain boundary and total conductivity for each substituted sample were estimated using Nyquist plots (Fig 4.21). The impedance spectra were fitted using the software *ZSimpWin*, and the best fit was obtained with the equivalent circuit shown in the inset of Fig. 4.21. At 200 °C, the high-frequency arc represents the bulk contribution, and the low-frequency region represents the depressed grain boundary arc, indicating its lower contribution for total conductivity. However, the electrode contribution is not observed at this temperature due to limited frequency range of the instrument.

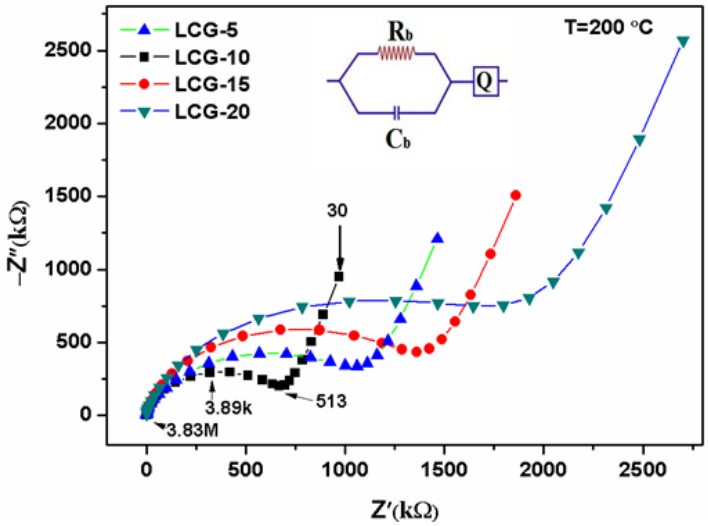

Fig. 4.21: Nyquist plots of the substituted samples, where numerical values for LCG-5 indicated the frequency points in Hz.

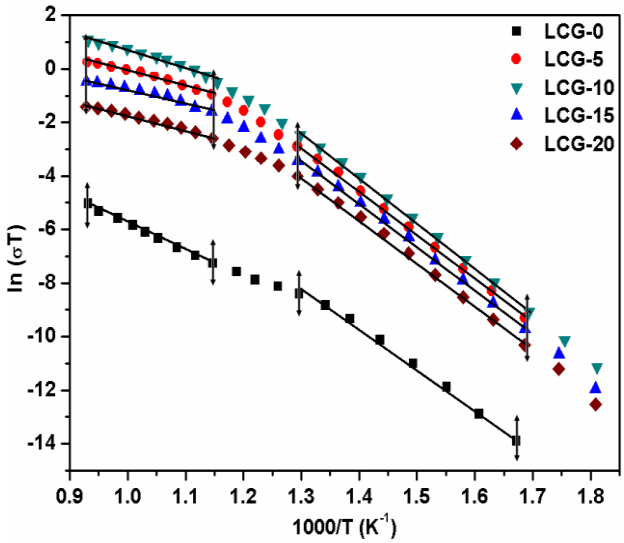

Fig. 4.22: The Arrhenius plot of the total conductivity with temperature in air.

The impedance spectra were fitted with a series of two electrical circuits (RC)Q, having a resistance (R) and a capacitor (C) coupled in parallel indicating bulk contribution, whereas the constant phase element (Q) was used to calculate the grain boundary contribution. It is observed that the bulk resistance decreases with Ca substitution upto LCG-10 and increases for LCG-15 and LCG-20. Since, the Ca substitution creates oxygen vacancies, which can be represented by Kronig-Vink notation as follows:

$$2CaO \xrightarrow{La_2O_3} 2Ca'_{La} + 2O_o^x + V_o^{\cdot\cdot} \qquad (4.8)$$

The formation of these vacancies is helpful to enhance the bulk conductivity of the system. However, the bulk resistance is increased for LCG-15 and LCG-20 samples. This could be due to the formation of secondary phase ($LaCaGa_3O_7$), which may obstruct the ion-hopping mechanism, thus lead to increase the resistance of the system. It is also reported that the minor secondary phase segregates along the grain boundaries and block ion flow across grains [37]. The electrical conductivity of these samples is calculated using the equation (4.2). The conductivity values obtained at 800 °C is given in Table 4.12. LCG-10 exhibited the highest ionic conductivity, which decreases further with increasing amount of the Ca-substitution. The ionic conductivity of LCG-10 is slightly less than $La(Sr)Ga(Mg)O_{3-\delta}$ system [17, 52], but comparable to $La_{0.9}Ba_{0.1}Ga_{0.8}Mg_{0.2}O_{3-\delta}$ [20] and higher than YSZ at the intermediate temperature (600-800 °C) range [53]. From Fig. 4.22, the conductivity curves clearly show non-linearity at the higher temperatures. Similar behavior of Arrhenius plot is also observed in $La_{0.9}Ba_{0.1}Ga_{0.8}Mg_{0.2}O_{3-\delta}$ system [20].

Table 4.12: Conductivity and activation energy of LCG samples at selective temperatures.

Sample name	σ (mS/cm) 800 °C	E_a (eV) (600-800 °C)
LCG-0	0.006	1.20
LCG-5	1.95	1.15
LCG-10	3.77	1.10
LCG-15	1.26	1.18
LCG-20	0.44	1.01

Huang *et al.* [19] reported that this bending is due to trapping of oxygen vacancies by substitution cations and/or the short range ordering-disordering transformation in the system. Another hypothesis was the effect of the grain boundary region that may obstruct the ion-hopping mechanism at the lower temperature region (T<600 °C) [12]. The activation energy values for this system are calculated using equation (4.3) at selective temperature range, and are given in Table 4.12. These activation energies are comparable to the La(Sr)Ga(Mg)$O_{3-\delta}$ and La(Ca)Ga(Mg)$O_{3-\delta}$ systems [52].

4.4. Synthesis of $La_{1-x}Sr_xInO_{3-\delta}$ ($0 \leq x \leq 0.50$) systems:

Sr^{2+} substitution for La^{3+} in $LaInO_3$ is considered as one of the best substitutions to achieve high conductivity and other properties required for solid electrolytes. This system has been widely explored on the electrical properties required for SOFC applications. In the present study, the correlation between conductivity with structural morphology, thermogravimetric analysis (TGA), thermal expansion coefficient (TEC) of the prepared samples of Sr^{2+} substituted $LaInO_3$ compound in the less explored compositional region is done. The results are discussed in the light of disordering oxygen vacancies and presence of secondary phase.

4.4.1. X-ray diffraction analysis:

The X-ray diffraction patterns of the synthesized series are shown in Fig. 4.23. It is observed that the samples from LSI-0 to LSI-5 are indexed with $LaInO_3$ phase (ICDD card number 01-072-3823). However, samples from LSI-10 to LSI-20 also exhibits single phase and matched with $La_{0.9}Sr_{0.1}InO_{2.95}$ phase (ICDD card number 01-074-3333). Contrary to this, other three samples (LSI-23, 26 and 50) show $La_{0.9}Sr_{0.1}InO_{2.95}$ as major phase along with $SrIn_2O_4$ as minor phase (ICDD card no. 01-072-3823) (Fig. 4.23). Since, the series from LSI-0 to LSI-20 is already reported in literature [54], so, in this study, we have reported the results from LSI-

20 to LSI-50 samples. The solubility of Sr^{2+} in the $LaInO_3$ perovskite structure is limited to LSI-20 and the substitution of $x \geq 0.23$ for La^{3+} leads to formation of a secondary phase which has been identified as $SrIn_2O_4$.

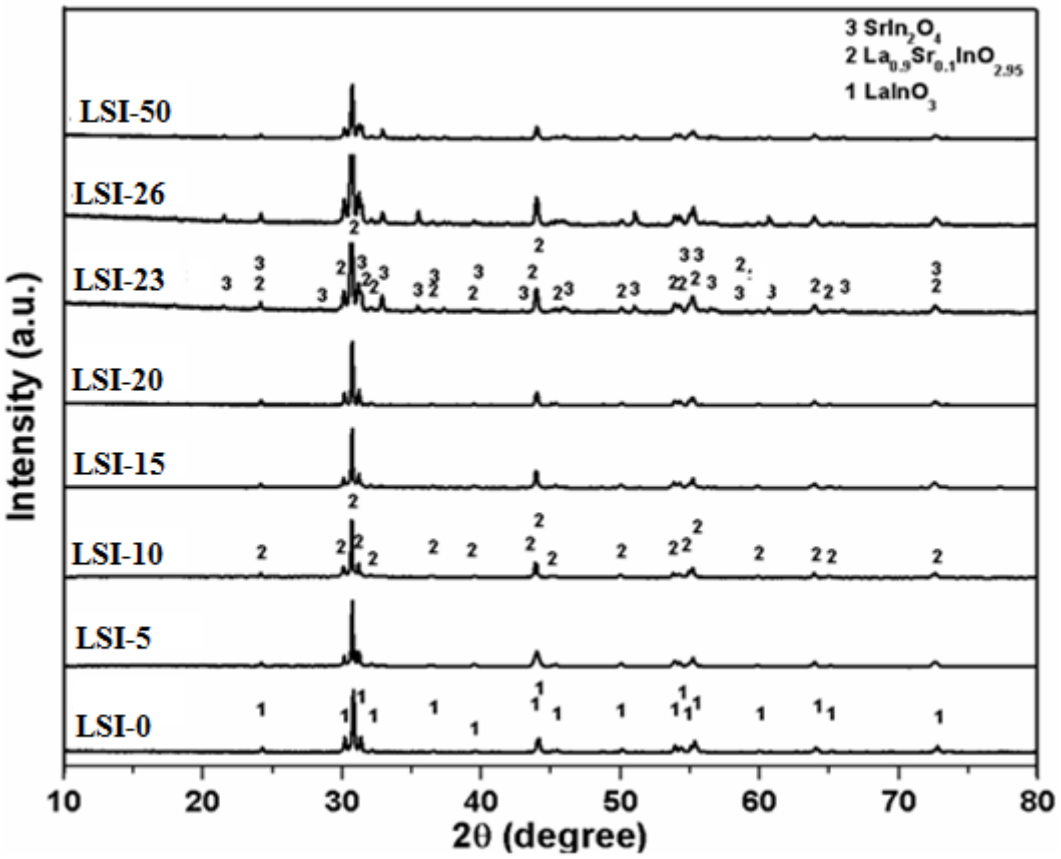

Fig. 4.23: XRD powder diffraction pattern of as-sintered Sr-substituted $LaInO_3$ samples.

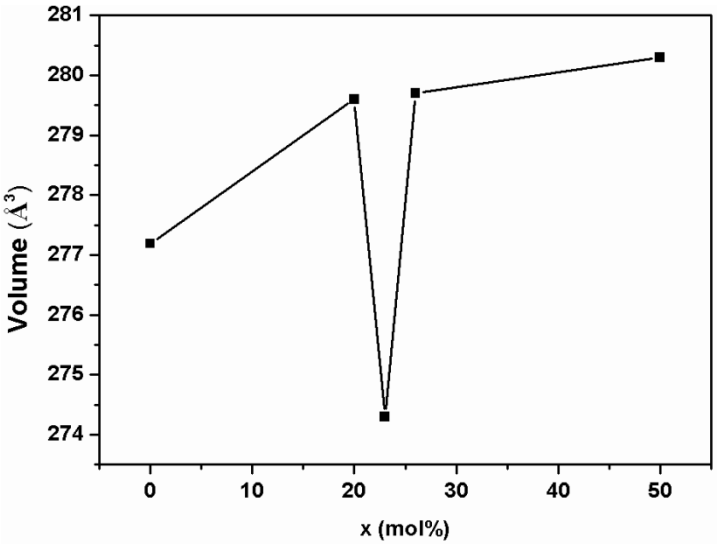

Fig. 4.24: Lattice volume with composition ($La_{1-x}Sr_xInO_{3-\delta}$).

The volume fraction of the secondary phase increases with increasing Sr-content. The lattice parameters were calculated using the observed inter-planar spacing (d-values for single

$La_{0.9}Sr_{0.1}InO_{2.95}$ peaks) obtained from the diffractogram. In comparison to reported $La_{0.9}Sr_{0.1}InO_{2.95}$ phase [55], the lattice parameters are marginally increased for LSI-20 sample. Interestingly, the lattice volume is decreased, when concentration of substitution increased from LSI-20 to LSI-23 (Table 4.13 and Fig. 4.24). On the other hand, the lattice parameters are almost invariant with increase in Sr-substitution above LSI-26.

Table 4.13: Lattice parameters and density for LSI-20, 23, 26 and 50 samples.

Sample name	*a* (Å)		*b* (Å)		*c* (Å)		Volume (Å^3)		Relative density
	Calculated	Rietveld refined	Calculated	Rietveld refined	Calculated	Rietveld refined	Calculated	Rietveld refined	
LSI-20	5.91	5.92	8.25	8.22	5.73	5.73	279.60	279.00	93
LSI-23	5.87	5.87	8.21	8.20	5.69	5.70	274.30	274.40	88
LSI-26	5.93	5.92	8.23	8.21	5.73	5.74	279.70	278.98	85
LSI-50	5.93	5.92	8.24	8.22	5.74	5.73	280.30	278.96	83

According to Vegard's law, the lattice parameters should vary linearly with substitution concentration in single phase region, but remains invariant in the multiphase region [2]. Although, the radius of Sr^{2+} (r_{VIII} = 1.26 Å) is slightly larger than that of La^{3+} (r_{VIII} = 1.16 Å), so its substitution should increase the unit cell volume. Whereas, in the present case, LSI-23 sample shows the shrinkage in lattice parameters. It can be explained on the basis of La coordination with oxygen. The coordination number of La^{3+} (r_{VIII} = 1.16 Å) might have changed from VIII to VI (r_{VI} = 1.03 Å) due to change in its position in lattice. Secondly, the oxygen vacancy defects occur after Sr substitution in $LaInO_3$ systems, which could also results in shrinkage of the crystal cells. The vacancy defect may also lead to shrinkage in lattice parameters as reported by Xing *et al.* [3]. In the present study, it seems that for lower concentrations of Sr^{2+} in the LSI-23 sample, the more disordered $SrIn_2O_4$ phase is formed as indicated by its FWHM (Fig. 4.25). As the percentage of substitution (Sr^{2+}) increases, the disordering in $SrIn_2O_4$ phase increases up to LSI-26. Higher concentration of Sr^{2+} leads to formation of more ordered $SrIn_2O_4$ phase in LSI-50 sample as indicated (Fig. 4.25). This result is also supported by our TGA data in N_2 atmosphere for this particular sample (discussed in TGA analysis). On the other hand, LSI-23 and LSI-26 shows higher disordering in $La_{0.9}Sr_{0.1}In_{2.95}$ phase (Fig. 4.25). Obviously, some Sr^{2+} might have occupied the La-site of $La_{0.9}Sr_{0.1}InO_{2.95}$ phase, which has created the local strain in the lattice.

The strains for La0.9Sr0.1InO3 is also calculated using Willianson-Hall's equation (4.1) and are given in Table 4.14. These values further support Sr-substitution in the parent phase. All the XRD data were further used for Rietveld refinement to understand these complicated systems in a better way.

Table 4.14: Strain and Volume fraction of phases present in as-sintered LSI samples.

Sample name	Volume fraction of $Ls_{0.9}Sr_{0.1}InO_{2.95}$ (%)	Volume fraction of $SrIn_2O_4$ (%)	Strain (∈)× 10^{-5} for perovskite phase
LSI-20	100	0	2.7
LSI-23	63	37	2.9
LSI-26	73	27	2.9
LSI-50	75	25	3.2

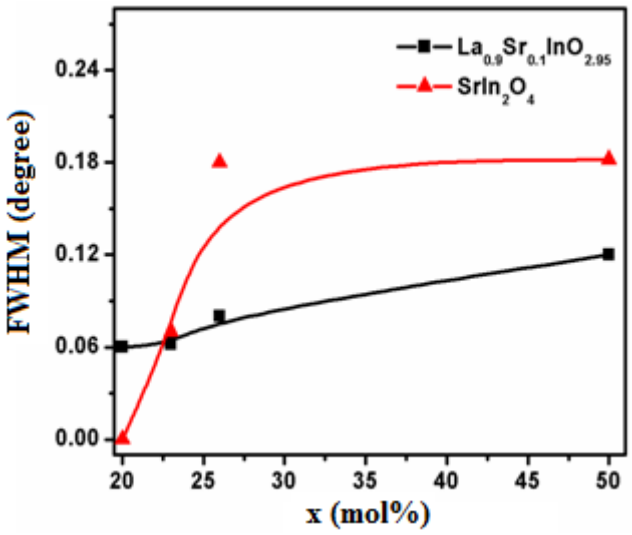

Fig. 4.25: Variation of FWHM with composition.

Rietveld analysis results are shown in Fig. 4.26(a-d). The space group and initial lattice parameters were presumed to be those of the earlier reported work [56]. The refined parameters are shown in Table 4.13. The refinement clearly matches with the orthorhombic phase in the LSI-20 sample. However, in case of LSI-23 sample, it shows some shifting and best fitted with the monoclinic phase of $La_{0.9}Sr_{0.1}In_{2.95}$. Interestingly; this sample exhibits better conductivity. On the other hand, LSI-26 sample again was best fitted with orthorhombic structure. However, the space group of this sample is different than LSI-20 sample, i.e., *pmmm*. Conventional Rietveld R-factors (R_p, R_{wp}, Rexp, Chi^2) is close to 1 in all samples.

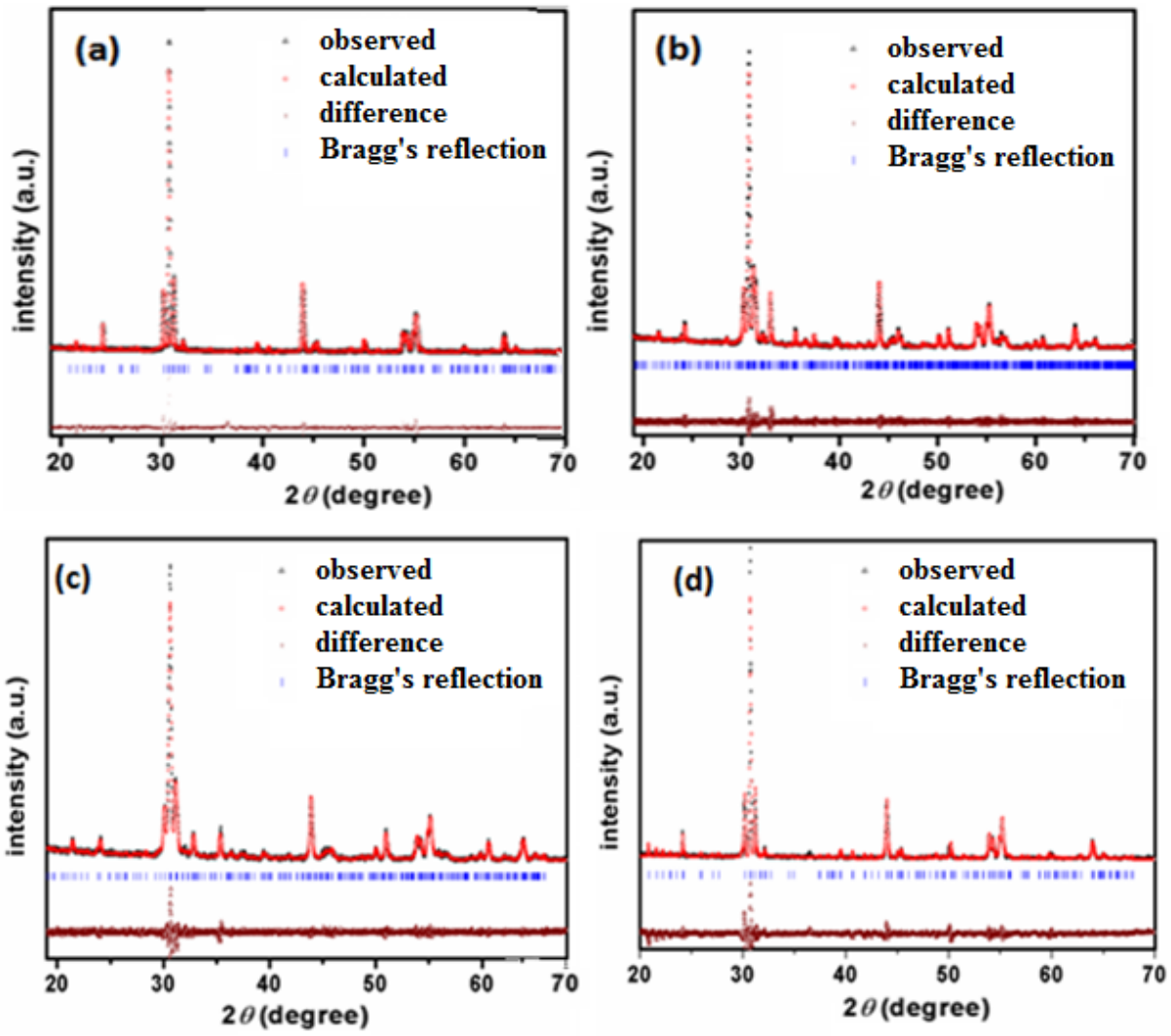

Fig. 4.26: Rietveld refinement of (a) LSI-20 (b) LSI-23 (c) LSI-26 (d) LSI-50 samples.

4.4.2. Microstructural analysis:

For microstructural analysis, fracture surfaces of the specimens were analyzed under SEM, which are given in Fig. 4.27 (a-f). The microstructure seems to be homogenous. Fig. 4.27 (a-b) presents the low and high magnification micrographs of LSI-20 sample, respectively. The low magnification micrograph shows the cleavage plane where the layered structure can be seen. The cleavage has occurred along the areas containing porosity. The river bed pattern which is typical characteristic of brittle material can be seen in Fig. 4.27(a) (marked as an arrow). The grain size varies from 1-4 μm. It seems that structure has developed in a layered form. As diffusion proceeds, these features become denser, which can be clearly seen in Fig. 4.27(b) (marked as an arrow). The structural features have become more pronounced because of pulling out action of grain.

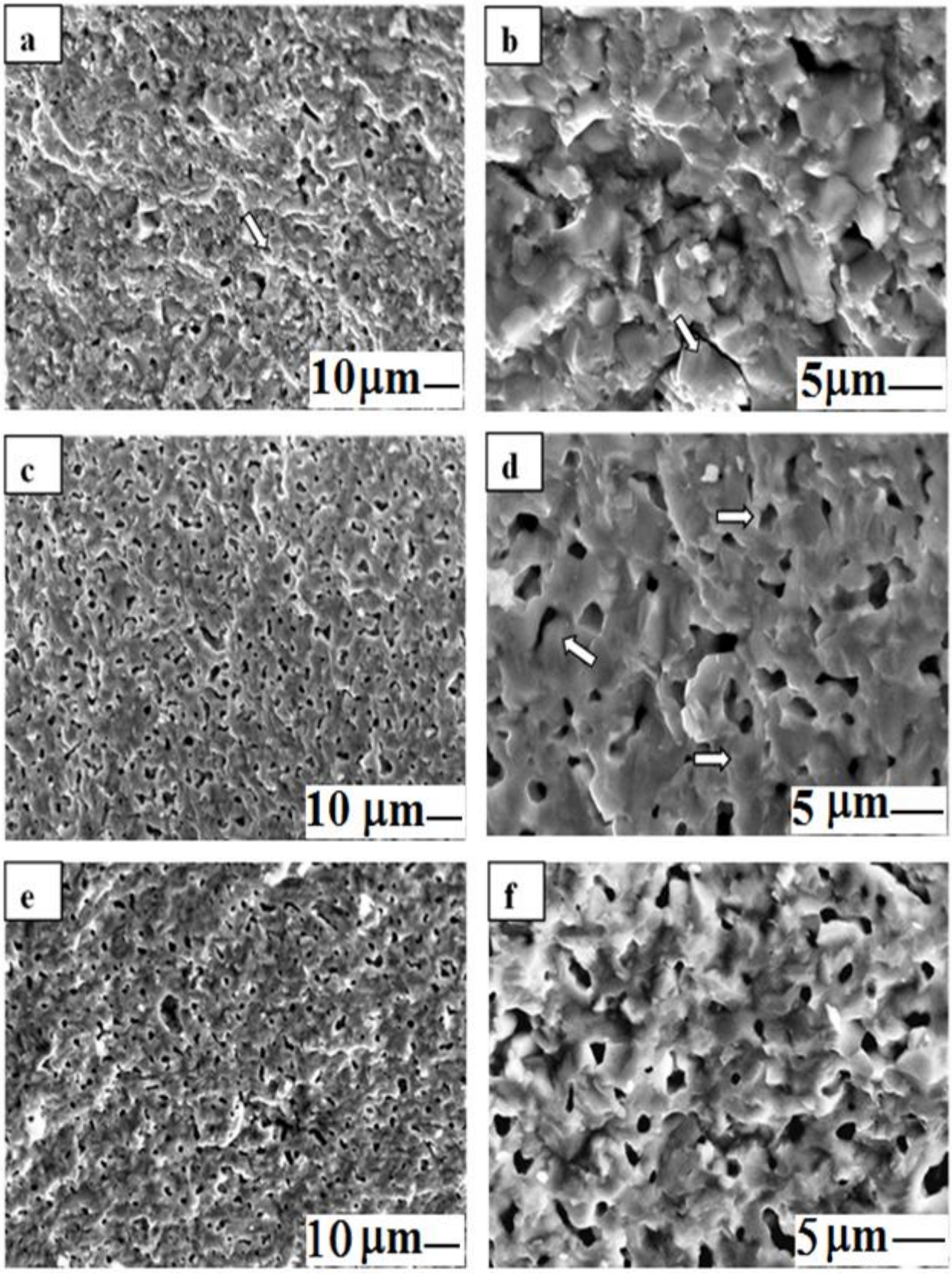
a
10µm
b
5µm
c
10 µm
d
5 µm
e
10 µm
f
5 µm

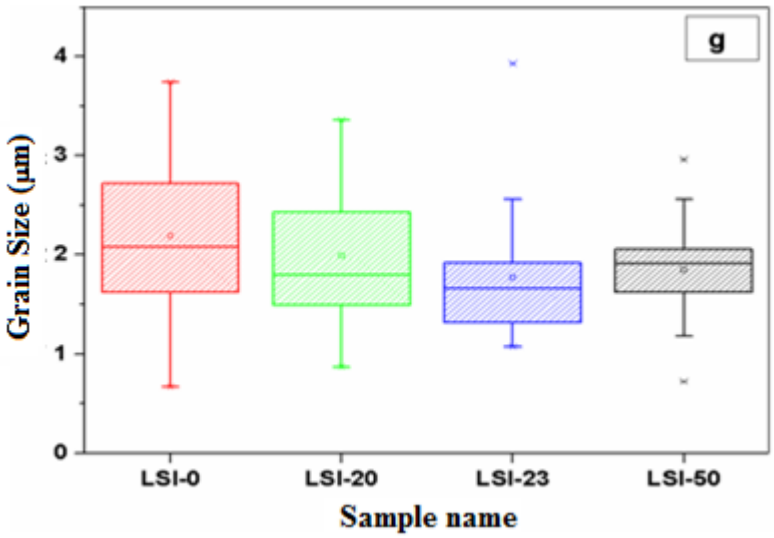

Fig. 4.27: (a) LSI-20 SEM (× 1,000) (b) LSI-20 SEM (× 3,000) (c) LSI-23 SEM (× 1,000) (d) LSI-23 SEM (× 3,000) LSI-50 SEM (× 1,000), (f) LSI-50 SEM (× 3,000) and (g) grain size distribution.

Moreover, because of the relatively higher volume fractions of interconnecting pores as can be seen in the higher magnification micrograph (Fig. 4.27b), this could become visible. Since LSI-20 is single phase compound having perovskite type of structure, so such structural features are possible. Fig. 4.27 (c, d) shows the micrographs of LSI-23 sample. The low magnification micrograph exhibits the structure of compound having compact grains where grain size varies from 1-3 μm. The pores are uniformly distributed, and structure is denser as compared to LSI-20. The pores have developed due to shrinkage of liquid phase which further ease the diffusion process. The higher magnification micrograph does not exhibit the features of interconnected pores. Besides this, the LSI-23 sample shows well connected fully grown grains as compared to LSI-20 sample. The interesting feature observed was the presence of different phases (white one, marked arrow) near the pores. As also discussed in XRD analysis, this sample has two phases. The second phase which is minor phase ($SrIn_2O_4$) was also confirmed by EDS analysis (discussed in EDS analysis). This minor phase gets segregated at triple points and has come out like volcano eruption when fractured.

Fig. 4.27 (e-f) shows the morphology of the LSI-50 sample. The structure is uniform in nature with compact grains. However, at certain places interconnected pores can be seen (Fig. 4.27e). However, pore size also varies from one area to another area. The most important feature observed in LSI-50 sample is the presence of second phase near the pores which can be easily visualized (white one) and is present throughout the sample (Fig. 4.27f). Though the volume fraction of this phase is low but is clearly observable. The grain size distribution with substitution concentration is shown in Fig. 4.27(g). This behavior is similar to the trend

observed for Sr-substituted $LaGaO_3$ system. Sr^{2+} suppresses the necking of grains due to reduced grain boundary mobility, which leads to decrease in average grain size.

4.4.3. EDS analysis:

In order to confirm the presence of two different phases, the elemental analysis was done on the LSI-23 sample to further verify the composition of formed phases. The area exhibiting different contrast was selected for EDS analysis for LSI-23 sample and is marked as *A* and *B* (Fig. 4.28). The atomic percentage of these two phases taken from areas *A* and *B* is shown in Table 4.15. Considering the entire compositional range of atomic percentage of the elements present in phase *A* (white one), the composition comes out to be $SrIn_{2.01}O_{3.99}$ which is for $SrIn_2O_4$ compound. For phase *B*, it comes out to be $La_{0.8}Sr_{0.1}InO_{2.6}$ which is close to $La_{0.9}Sr_{0.1}InO_{2.95}$ compound as also observed in X-ray analysis. Since X-ray analysis has confirmed the presence of $SrIn_2O_4$ and $La_{0.9}Sr_{0.1}InO_{2.95}$ phases and moreover, the EDS analysis which gives approximation only, the white phase (minor) visible in the microstructure designates the presence of $SrIn_2O_4$ phase and other one (major) is for $La_{0.9}Sr_{0.1}InO_{2.95}$ phase.

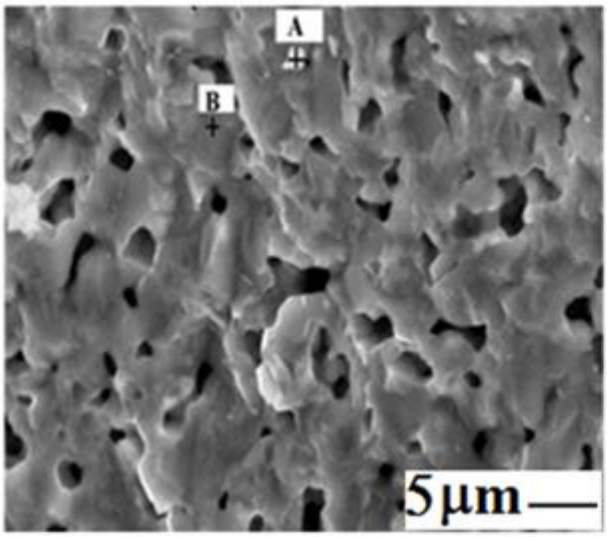

Table 4.15: Elemental composition in LSI-23 sample.

Element	Atomic % (A)	Atomic % (B)
O K	57.02	58.31
Sr L	14.28	2.02
In L	28.70	22.64
La L	0.00	17.03
Total	100.0	100.0

Fig. 4.28: EDS of LSI-23 sample.

4.4.4. TEC analysis:

Fig. 4.29 shows the graphs of thermal expansion measurements in air. All compositions show linear change in relative length along the entire temperature range. The relative change in length is linear with slight variation in slope. The higher temperature slopes are larger compared to lower temperature slope in all samples as given in Table 4.16. An increase of the thermal expansion at elevated temperatures could be due to the loss of lattice oxygen. Similar

changes have also been observed in TGA analysis. Due to stoichiometric reasons, the formation of oxygen vacancies at elevated temperatures may decrease the valence of cations thus increasing cationic radii, which finally lead to an expansion of the lattice [57]. For oxygen release, this chemical expansion also contributes to the regular thermal expansion. Interestingly, increasing content of strontium increases the thermal expansion. But for LSI-50, there is a sharp decrease in TEC. It may be because of increasing amount of secondary phase ($SrIn_2O_4$) which suppresses the overall thermal expansion [57, 58, 59].

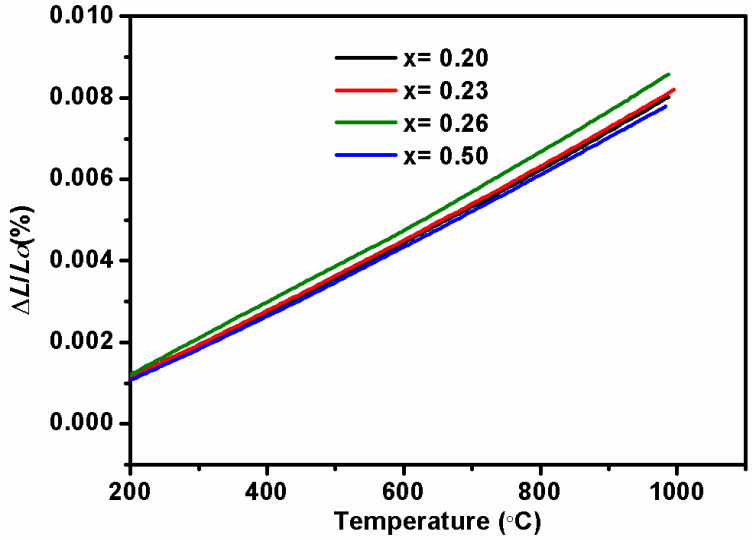

Fig. 4.29: Thermal expansion coefficient plots of as-sintered samples.

Table 4.16: Thermal Expansion Coefficient (TEC) for as-sintered LSI samples.

Sample name	TEC × 10^{-6} /°C (150-400 °C)	TEC × 10^{-6} /°C (600-800 °C)
LSI-20	7.82	9.60
LSI-23	8.01	9.15
LSI-26	8.96	9.71
LSI-50	7.71	8.82

4.4.5. TGA analysis:

The stability of the material at reducing atmosphere can be found out by comparing the TGA results in N_2 atmosphere [57]. Therefore, TGA measurements of all the prepared samples were performed in N_2 atmosphere to observe the phase stability in the temperature range of 50 to 1000 °C. TGA curve of all the samples show weight gain in nitrogen above 400 °C. This phenomenon can be explained on the basis of Sr^{2+} substitutions in the present series of samples.

Due to increase in Sr-substitution, the samples become oxygen deficient. In commercial nitrogen atmosphere (Fig. 4.30), all the samples show small weight loss below 200 ºC (up to region indicated by I) is due to water loss from the samples. The minimum weight loss observed (~ 0.02%) was in LSI-23 sample.

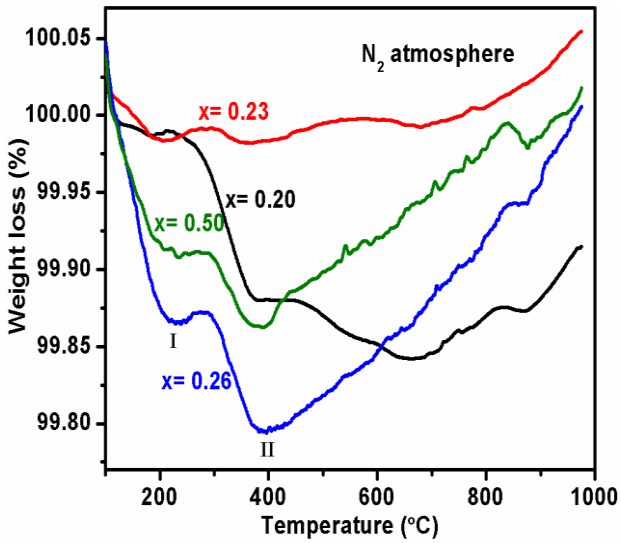

Fig. 4.30: TGA plots of as-sintered $La_{1-x}Sr_xInO_{3-\delta}$ system in N_2.

This can be ascribed due to less porosity and minimum hygroscopic tendency of the sample. The second weight loss (indicated by II) in TGA is observed in all the samples below 400 ºC. It belongs to the relaxation process within materials and sometimes due to loss of volatile species. Since, the system has sufficient activation energy to acquire 1/2 O_2 (g) from the atmosphere (since N_2 was not ultrapure in present case) to fill the oxygen vacancy, which may lead to weight gain above 400 ºC. Among all samples, LSI-23 is the most stable showing minimum weight change, hence maximum thermal stability. The reason for this is that, LSI-23 is optimized with an appropriate mixed stoichiometric ratio, which leads to minimum unreacted phase. This may be the possible reason to exhibit highest thermal stability as compared to other samples. The weight change taking place in this sample can be correlated to higher oxygen vacancy/defects as reported by He *et al.* [54]. Similar observations can also be seen in TGA curve of this particular sample, which shows the higher weight gains as compared to the other samples.

4.4.6. Impedance analysis:

Impedance spectroscopy (IS) was used to analyze the conductivity behavior of the samples from room temperature to 900 ºC. Fig. 4.31 shows Nyquist plot of the best conductive sample (LSI-23) at 290 ºC. Here, the measuring cell has geometrical capacitance (C_g) and bulk

resistance (R_b) in parallel with it. These elements lead to the time constant $\tau = C_g R_b$, the dielectric relaxation time of the basic materials. Fig. 4.32, shows the variation of real part (Z') vs. frequency of LSI-23, at different temperatures. It is observed that the magnitude of real impedance decreases with the increase in frequency and temperature. It shows an increase in a.c. conductivity with the rise in temperature and frequency. The values of Z' merge at frequency above 80 kHz. This may be due to release of space charges as a result of reduction in barrier properties of material with the rise in temperature. It is also responsible for the increase in ionic conductivity at higher frequencies in the sample [60]. Also, at low frequencies, the values of Z' decreases with the increase in temperature showing negative temperature coefficient type behavior. Further, at low frequencies, Z' values reach a maxima peak at temperature above 350 ºC [61]. A typical peak broadening also takes place with increasing temperature. The broadening of peak suggests that, there is spread of the relaxation time. This phenomenon has also been reported by Sahoo *et al.* [60]. Similar transition is observed in all samples. It is clear that with the increase in temperature, slope of the curves decrease and curves bend towards lesser values of Z'. Single semicircle arcs in the complex plane reveal that the conduction in the material is grains dominated than grain boundaries.

Fig. 4.33 shows the electrical conductivity of these samples in air as a function of temperature. The corresponding values of activation energy (E_a) calculated from Arrhenius plots are listed in Table 4.13. It has been reported earlier that, in unsubstituted $LaInO_3$, lattice defects arise from intrinsic (Schottky and Frenkel) defects [55]. These thermodynamic effects are distributed randomly, and contribution is not sufficient for appreciable conductivity, whereas, substitution ions with valency lower than the parent ion tend to introduce oxygen vacancy concentration ($V^{\bullet\bullet}_O$) as shown by Kronig-Vink notation (4.8) as:

$$2SrO \xrightarrow{La_2O_3} 2Sr'_{La} + 2O^x_O + V^{\bullet\bullet}_O \qquad (4.8)$$

Where, Sr'_{La} means Sr in La site with the apparent unit negative charge (denoted by symbol ') and $V^{\bullet\bullet}_O$ is the vacancy in an oxygen site with double positive charge, O^x_O means the lattice oxygen with mean charge zero. The excess of oxygen vacancies so formed are helpful for the hopping mechanism which increases the ionic conductivity of the substituted samples. When Sr^{2+} substitutes at La-site ($La_{1-x}Sr_xInO_{3-\delta}$), an increase the oxygen vacancies as shown in equation (4.8), may result in an increase of net electrical conductivity. The conductivities of all the samples at different temperatures have been compared in Table 4.17.

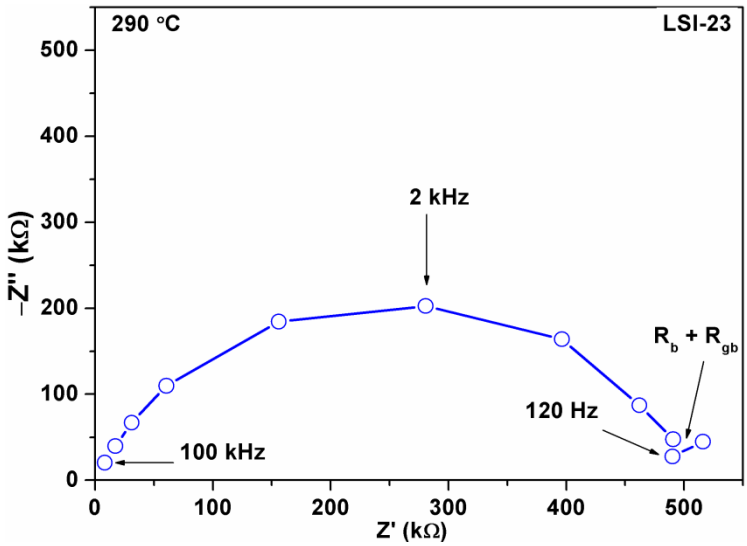

Fig.4.31: Nyquist plot of LSI-23 at 290 ºC.

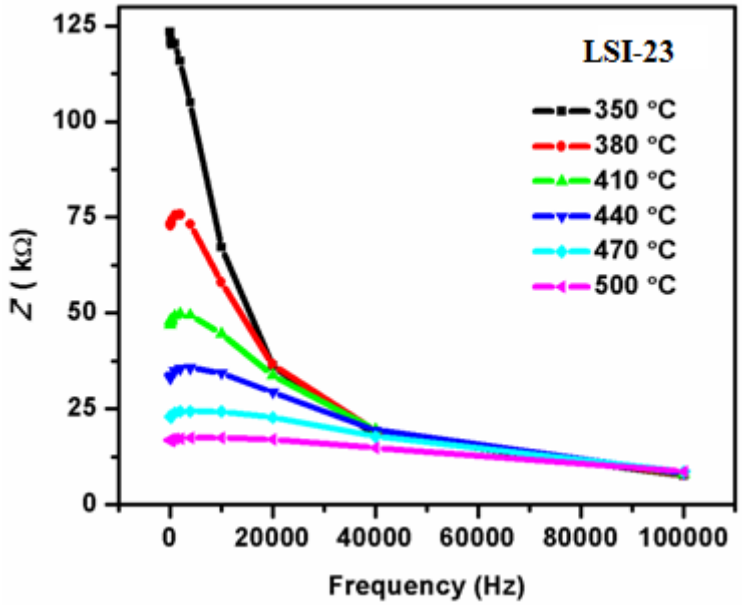

Fig.4.32: Freq. vs. Real Impedance plot of LSI-23.

At intermediate temperature range (250-750 ºC), the conductivity of LSI-23 is highest among all investigated samples. Also, the activation energy decreases from LSI-20 to LSI-23. It is minimum than earlier reported work on $La_{0.9}Sr_{0.1}InO_{2.95}$ [55] as given in Table 4.17. Since $LaYO_3$ as reported earlier is predominantly a proton conductor, while $LaGaO_3$ is mainly an oxygen conductor [41, 62], the activation energies of the present investigated samples are close to $LaYO_3$, than to $LaGaO_3$, so the effect of protonic conduction dominates at intermediate temperature range. It is further seen that all the samples show gradual increase in slope above 680 ºC.

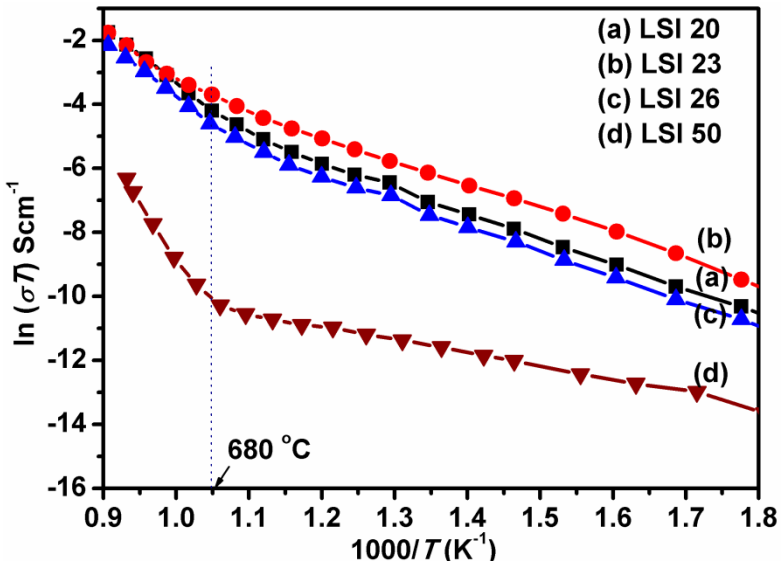

Fig. 4.33: Arrhenius plots of as-sintered LSI samples.

Table 4.17: Conductivity and activation energy values for as-sintered LSI samples at different temperatures.

Sample name	$\sigma \times 10^{-7}$ (S/cm) at 350 °C	$\sigma \times 10^{-6}$ (S/cm) at 500 °C	$\sigma \times 10^{-4}$ (S/cm) at 800 °C	E_a (eV) 370-550 °C	E_a (eV) 700-800 °C
LSI-20	2.21	2.11	1.20	0.68	1.52
LSI-23	5.53	4.03	1.59	0.63	1.04
LSI-26	1.96	2.05	1.12	0.69	1.52
LSI-50	0.058	0.019	0.017	0.37	2.60

This gradual transition reflects the transition in the behavior of material, which might be due to change of the predominant charge carrier from proton to oxide ion conduction with increasing temperature [63]. At high temperature (T > 750 °C), Arrhenius plots superimpose to each other. Also, with the further increase in Sr-substitution, a decrease in overall conductivity is observed, which suggests the formation of less-conducting $SrIn_2O_4$ secondary phase [54]. As the secondary phase is not present in the significant amount, so it will be distributed randomly throughout the sample (mostly at triple points with smaller grain size or along grain boundaries) and may act as scattering centre causing obstruction in the conduction path, which may lead to decrease in overall conductivity [62].

4.5. $La_{1-x}Ba_xInO_{3-\delta}$ ($0 \leq x \leq 0.20$) systems:

The effect of Ba-substitution on $La_{1-x}Ba_xInO_3$ system and their effects on thermal stability and conductivity have been studied in this series. TEC analysis is performed to study the lattice expansion at operating temperature range of SOFCs.

4.5.1. X-ray diffraction analysis:

Fig. 4.34(a) shows the XRD results of sintered samples of $La_{1-x}Ba_xInO_{3-\delta}$ (x=0.0-0.20). The sample names along with their volume fraction are given in Table 4.18. All the XRD peaks of LBI-0 sample were indexed with orthorhombic structure (ICDD card no. 01-072-3823). The XRD data confirmed the solid solubility limit upto 5 mol%. Further addition of Ba^{2+} (LBI-10), leads to a shoulder at 30.4°. As substitution concentration increases from LBI-10 to LBI-20, some low-intensity peaks at 43.5°, 43.6° and 63.2° were observed (Fig. 4.34, LBI-15 and LBI-20). These XRD peaks were indexed with cubic phase. The cubic phase formation could be explained on the basis of the tolerance factor. The substitution of Ba ion (r_{XII} =1.61Å) on La site (r_{XII} =1.36Å) increases the tolerance factor close to 1, which leads to the formation of cubic perovskite lattice. These results are in good agreement with the earlier reports [64, 65]. Also, Fig. 4.34(b) shows the variation of lattice volume of parent phase with Ba-content. The lattice volume uniformly increases upto 10 mol% Ba-content. However, slight variation is observed for LBI-15 and LBI-20 samples. It also indicates the effect of secondary phase for these compositions. Since, secondary phase is formed for $x \geq 0.10$. So, LBI-20 is not included in further analysis and discussion. The incorporation of Ba-content in $LaInO_3$ also introduces microstrain, which is calculated using Williamson-Hall equation (4.1). The calculated values for the synthesized samples are given in Table 4.18. These values indicate an increase in microstrain with Ba-content for all substituted samples.

The existence of cubic phase along with orthorhombic phase was further verified by Rietveld refinement. The generated peaks and data are shown in Fig. 4.35(a-d), and Table 4.19, respectively. The space group and initial parameters used for the refinement were taken from the literature [41]. Goodness of fit (Chi^2) for the refined data was less than 1.8. LBI-0 was refined with space group *pnma* and solid solubility limit was extended to 5 mol%. For LBI-10, the solid solubility limit gets disturbed, and the system was refined with secondary phase having the cubic lattice with space group *pm3m*. The volume fraction of cubic phase formed in LBI-10 and LBI-15 is 2.34% and 4%, respectively. Lattice parameters increase up to x=0.05 due to larger ionic radii of Ba^{2+} (r_{Ba}=1.61Å) than La^{3+} (r_{La}=1.36Å). For LBI-10 and LBI-15, the solid solubility gets disturbed and results in the formation of orthorhombic and

cubic phases (Fig. 4.35c-d). The unit cell volume of orthorhombic phase is nearly same in this substitution region (Table 4.19). These results are in accordance with Vegard's law [2]. Surprisingly, the formation of cubic phase is highly unlike. Usually, lower valence substitutions lead to increase in the oxygen vacancies in the system to maintain the charge neutrality and leads to secondary phase above solid-solubility limits. In the present case, both the crystalline phases have the similar chemical formula with a different space group. The only reason seems to be that Ba ion at A-site of ABO_3 provides better symmetry and forms the cubic structure. The theoretical density of all the samples has been calculated using the following equation:

$$d_{th} = z\frac{M}{V \times 0.6023} \tag{4.9}$$

where, *z* is the number of chemical units per unit cell of the crystal, *M* is the atomic weight of one unit of the chemical formula and *V* is the unit cell volume calculated by XRD results.

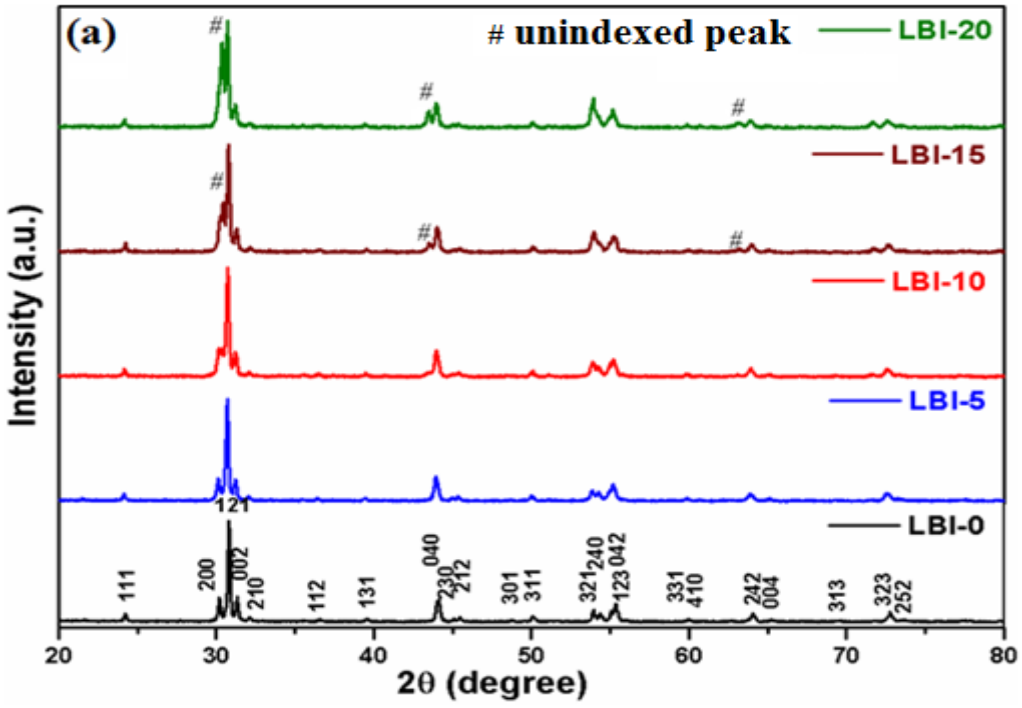

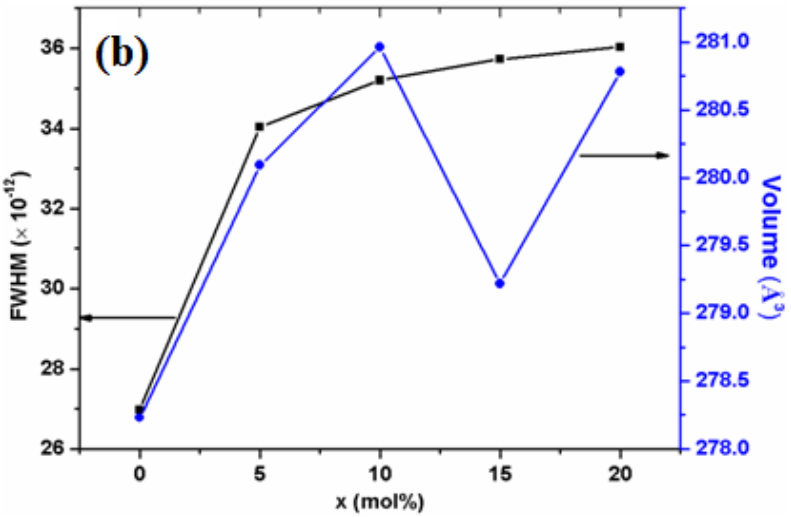

Fig. 4.34: (a) XRD pattern of as-sintered LBI samples and (b) FWHM and lattice volume with composition.

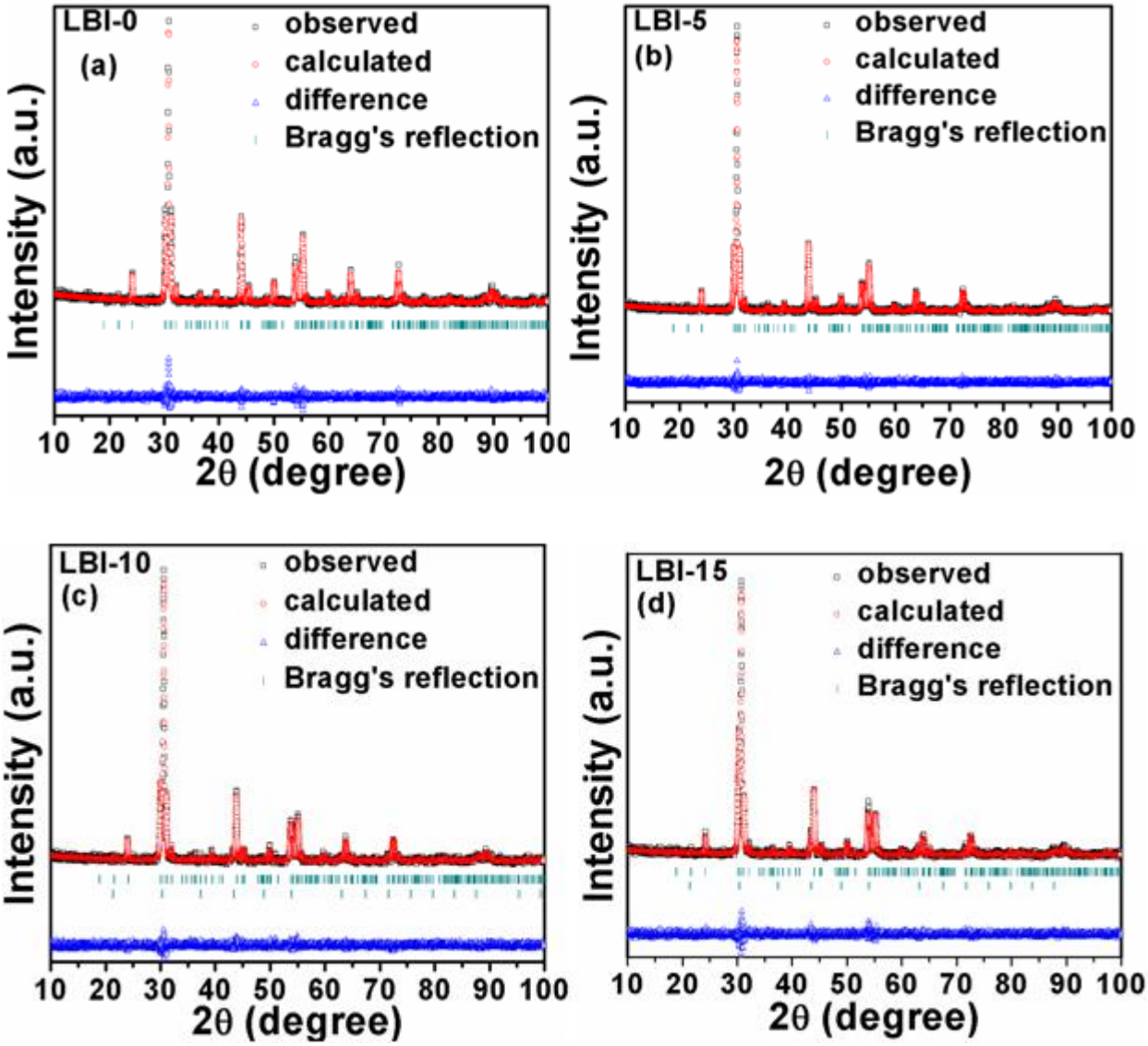

Fig.4 35: Rietveld refinement of (a) LBI-0 (b) LBI-5 (c) LBI-10 & (d) LBI-15 samples.

Table 4.18: Volume fraction, strain and TEC values of LBI samples.

Sample names	Volume fraction (wt. %)		Strain (∈) $\times 10^{-5}$	TEC $\times 10^{-6}$ (/°C) (400-800°C)
	Orthorhombic	Cubic		
LBI-0	100.00	0.00	2.12	8.72
LBI-5	100.00	0.00	2.17	9.88
LBI-10	97.66	2.34	2.23	9.90
LBI-15	96.00	4.00	2.57	9.90

Table 4.19: Refined structural parameters for LBI samples.

	LBI-0	LBI-5	LBI-10		LBI-15	
Structure	Orthorhombic	Orthorhombic	Orthorhombic	Cubic	Orthorhombic	Cubic
Space group	Pnma	Pnma	pnma	pm3m	Pnma	pm3m
***a*(Å)**	5.9271	5.9349	5.9408	4.1723	5.9249	4.1627
***b*(Å)**	8.2093	8.2314	8.2396	-	8.2254	-
***c*(Å)**	5.7181	5.7335	5.7398	-	5.7295	
***V*(Å^3)**	278.228	280.096	280.962	72.632	279.225	72.132
La/Ba						
g	1.10	0.97/0.33	1.13/0.10	0.85/0.15	0.85/0.15	0.75/0.15
x	0.0542	0.0512	0.0534	0.0	0.402	0.0
y	0.25	0.25	0.25	0.0	0.25	0.0
z	0.5149	0.5121	0.5187	0.0	0.5148	0.0
In						
g	1.14	1.32	1.40	1.0	1.35	1.0
x	0.0	0.0	0.0	0.5	0.0	0.5
y	0.0	0.0	0.0	0.5	0.0	0.5
z	0.0	0.0	0.0	0.5	0.0	0.5
O1						
g	1.17	1.35	1.91	3.0	1.46	3.0
x	0.9564	0.9566	0.8387	0.5	0.8855	0.5
y	0.25	0.25	0.25	0.5	0.25	0.5
z	0.1130	0.1342	0.1776	0.0	0.1372	0.0
O2						
g	1.99	2.96	1.57	-	1.91	-
x	0.2904	0.2995	0.3616	-	0.3295	-
y	0.4292	0.4452	-0.0141	-	0.4697	-
z	0.7963	0.7969	0.4994	-	0.8141	-

Table 4.20: Relative density and average grain size of LBI samples.

Sample name	Relative density (%)	Average grain size (μm)
LBI-0	95.5	2.2
LBI-5	92.1	0.6
LBI-10	91.4	0.7
LBI-15	91.8	0.7

The experimental density was calculated using Archimedes method, and the percentage of relative density is given in Table 4.20. The relative density for all the synthesized samples is above 90%.

4.5.2. Raman analysis:

Raman analysis of the present series was investigated to verify the Ba-substitution and vacancy formation in lanthanum indate. For the perovskite type structure, the total number of optical vibrations (Γ_{op}) and the acoustic modes (Γ_{ac}) are given by following equation:

$$\Gamma_{op} = \underset{(R)}{7A_g} + \underset{(R)}{7B_{1g}} + \underset{(R)}{5B_{2g}} + \underset{(R)}{5B_{3g}} + \underset{(i)}{8A_u} + \underset{(ir)}{7B_{1u}} + \underset{(ir)}{9B_{2u}} + \underset{(ir)}{9B_{3u,}} \qquad (4.10)$$

$\Gamma_{ac} = B_{1u} + B_{2u} + B_{3u}$.

These representations show that there are 24 Raman active modes, ($7A_g + 7B_g + 5B_{2g} + 5B_{3g}$) and 25 infrared active modes ($7B_{1u} + 9B_{2u} + 9B_{3u}$), while the $8A_u$ modes are inactive modes in both Raman and infrared [66, 67]. These Raman modes can be divided into two symmetric, four antisymmetric stretching mode, four bending modes and six rotational/tilt modes of the BO_6 octahedra. The last Raman active eight modes are related to the motion of A-site cation in ABO_3 [68]. These modes appear due to four lattice distortions from ideal perovskite structure, which are rotation of BO_6 octahedra around cubic [001] and [110] axis, Jahn-Teller distortion and La/Ba shift from its position from ideal positions [69-71]. In the present system, the Raman active modes are present in the range 100-450 /cm (Fig. 4.36(a)). The observed Raman peaks for un-substituted sample (LBI-0) are at the positions 122, 142, 180, 200, 232, 263, 308, 351 and 386 /cm. These spectral bands are in accordance with earlier reported work for similar system [67, 69]. The spectral band at 200 cm^{-1} is due to InO_6 structural unit [72], while the mode at 263 cm^{-1} is assigned to the oxygen octahedron tilt [68], and the highest intensity peak at 386 cm^{-1} is attributed due to stretching mode of InO_6 [2].

Further, the Raman bands in 300-600 cm^{-1} region are assigned to vibration motion due to cation-oxygen-cation (In-O-In) groups [73].

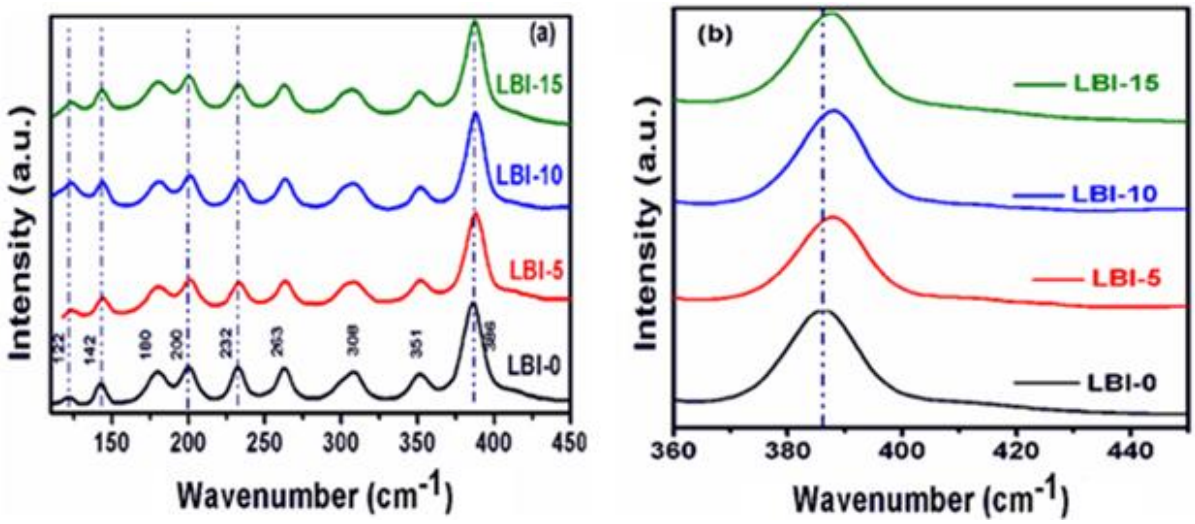

Fig. 4.36: (a) Raman spectra of LBI samples, **(b)** Blue shift observed in most intense peak at 386 cm^{-1}.

Moreover, selective Raman bands (122, 142, 200, 232 and 386 cm^{-1}) shows the change in the peak position with respect to un-substituted sample (LBI-0). This change can be explained on the basis of three factors: change in average atomic mass, mixed valency of A-site cation [68], and formation of oxygen vacancies due to aliovalent impurity substitution [74, 75]. In the present case, the difference in atomic mass of substitution ion with respect to host ion is insignificant. However, the valency of substitution ion (Ba^{2+}) at La^{3+} sites lead to mixed valency of A-site cation. Therefore, with Ba-content, the average valency of A-site ion will decrease and may lead to elongation of bonds, which results in shifting of bands to higher frequency (blue shift). This shift indicates the A-site substitution of Ba at La-site in $LaInO_3$ [76].

Moreover, the blue shift is most prominent for highest intense Raman band at 386 cm^{-1} (Fig. 4.36b). This shift is clear for $\times$=0.05; however, it is almost invariant with further substitution up to LBI-15. This interesting anomaly is consistent with XRD results. As discussed in XRD analysis, single orthorhombic phase is formed for LBI-5, and a mixture of orthorhombic and cubic phases co-exist for LBI-10 and LBI-15 samples. Since, the cubic phase is more ordered, which leads to lesser tilting of InO_6 octahedra. However, the orthorhombic phase is more distorted in nature. The Ba-substitution further increases the lattice distortions and may lead to stress in the perovskite phase. It is reported in literature that compressive stress results in the blue shift of the Raman band [77]. So, distorted orthorhombic phase leads to the

observed shift in LBI-5. However, the formation of symmetric cubic phase at higher substitution prevents further shifting of the Raman band (Fig. 4.36b).

4.5.3. Microstructural analysis:

The microstructural features and grain size distribution of the sintered samples are shown in Fig. 4.37(a-e). Microstructure of LBI-0 (Fig. 4.37a) shows the well sintered structure with negligible porosity. The grain size for LBI-0 sample varies from 2 to 3 μm having well-developed faceted structure. However, at triple points where three grains meet, some porosity is observed. Ba-substitution causes the distortion in structure and round grains having average grain size less than 1μm can be seen. When substituted with 5 mol% Ba, the faceted morphology starts to acquire round shape where both types of faceted and round features are observed. Moreover, with further increase in Ba-substitution to 10 mol%, the grain size increases slightly and structure becomes more uniform. When the Ba content is increased to 15 mol%, the grain size is almost invariant (Fig. 4.37e).

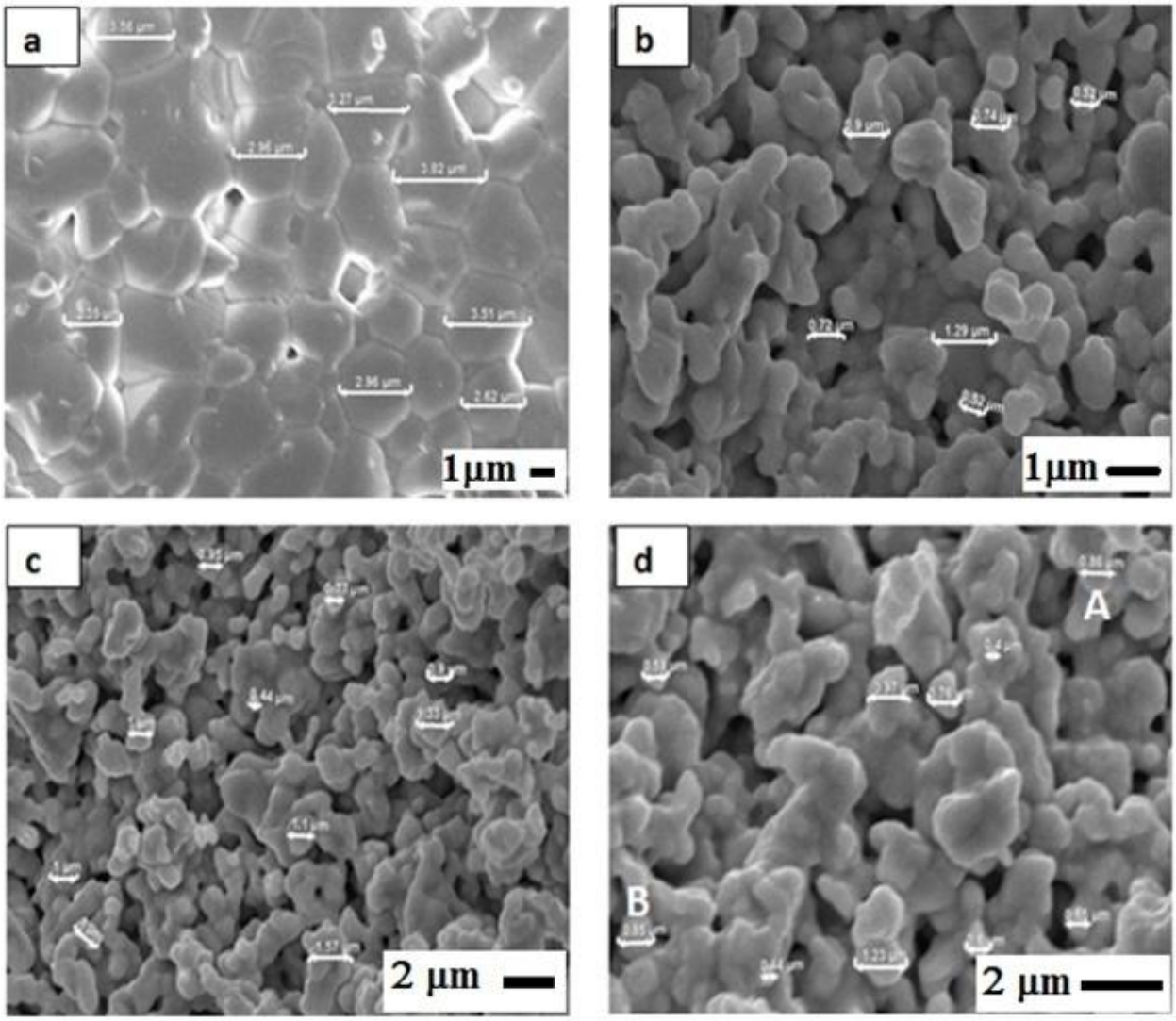

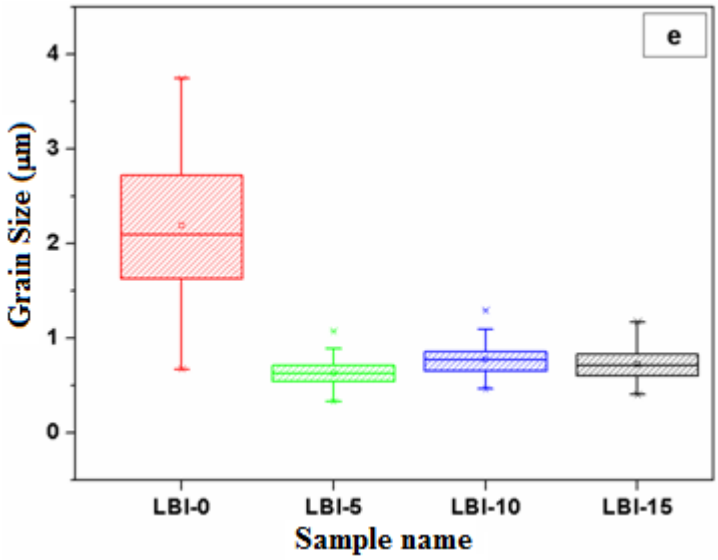

Fig. 4.37: SEM images of as-sintered samples of (a) LBI-0, (b) LBI-5, (c) LBI-10, (d) LBI-15 and (e) grain size distribution.

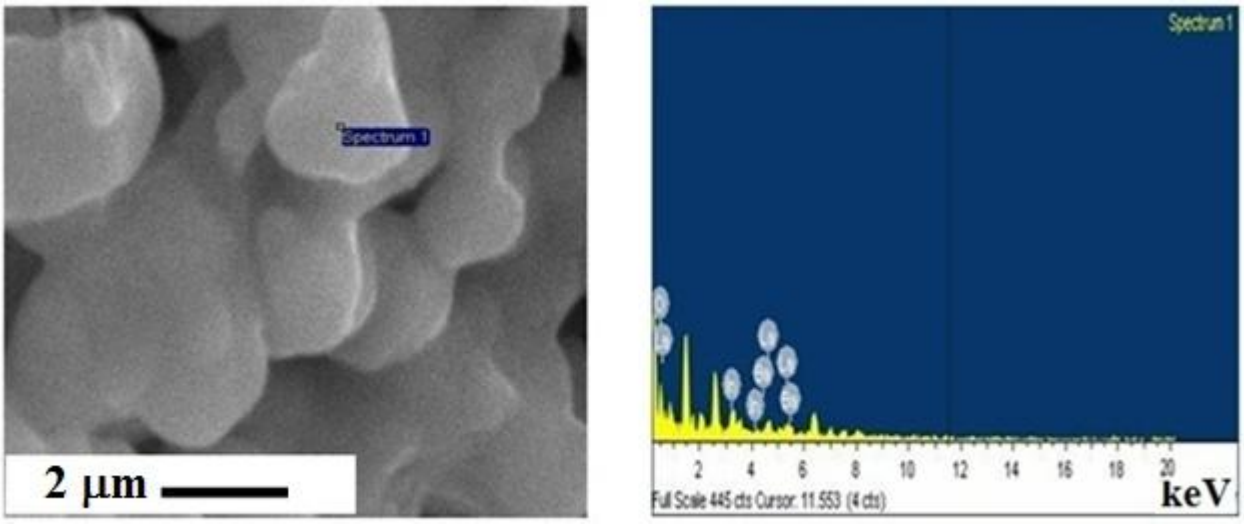

Fig. 4.38: EDS analysis of LBI-10 sample.

Table 4.21: Elemental composition of LBI-10 sample.

Element	Weight %	Atomic %
O K	64.75	93.75
In L	10.36	2.09
Ba L	7.47	1.26
La L	17.42	2.90
Total	100.0	100.0

Considering the entire structure, Ba substitution has caused distortion in structure and a transition from faceted to non-faceted is observed. The average grain size of the as-sintered samples is given in Table 4.20, which indicated the uniform decrease of grain size with Ba-substitution. The grain size is minimum for LBI-15 sample. Moreover, the porosity of substituted samples is slightly increased. As discussed in XRD section, LBI-10 and LBI-15 samples contain cubic phase along with orthorhombic lattice, the signatures of any other secondary phase are not observed. Furthermore, grains of uniform spheres with average size ~0.7 μm as shown in Fig. 4.37(d) and marked as *A* and *B* could be the cubic phase in this particular sample. To get the qualitative idea about elemental compositions, EDS analysis was performed on the LBI-10 sample (Fig. 4.38 and Table 4.21). The result indicates the formation of desired phase in the present sample. Also, higher atomic percentage of oxygen is observed in EDS analysis. It could be mainly due to the H_2O adsorption in the vacant sites of this type of perovskite systems, which is also reported in literature [34, 35].

4.5.4. TEC analysis:

Thermal expansion behaviors of all the investigated samples as a function of temperature are shown in Fig. 4.39, and their values at particular temperature range is given in Table 4.18. The plots are non-linear, with the TEC tending to increase with increasing temperature. It is evident that LBI-0 sample exhibited the smallest expansion behavior, whereas, Ba-substituted lanthanum indate showed a slight increase in thermal expansion. Since, the ionic radius of Ba^{2+} (r_{XII}=1.61Å) is higher than that of La^{3+} (r_{XII}=1.36Å), so expansion increases with Ba^{2+} substitution. Similar trend in thermal expansion has also been observed in other alkaline earth–substituted perovskite systems [52].

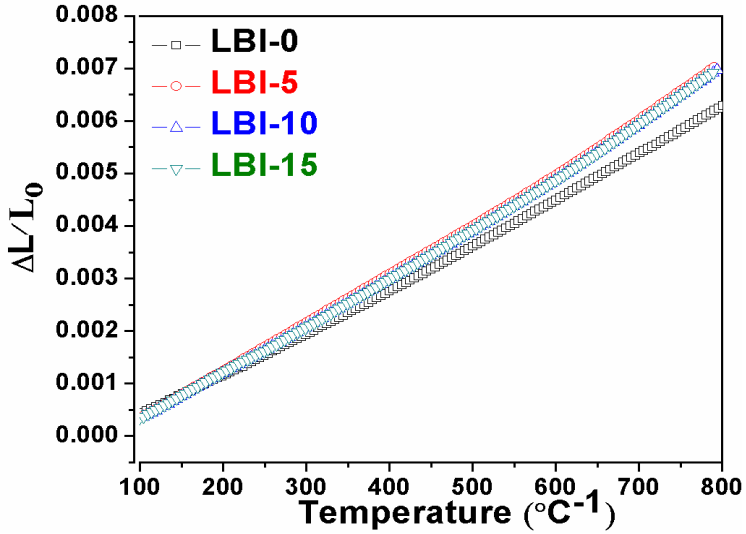

Fig. 4.39: Linear thermal expansion for $La_{1-x}Ba_xInO_{3-\delta}$ as function of Ba content in air.

LBI-5 showed the highest thermal expansion coefficient among all the investigated samples. Furthermore, in LBI-10, the value of TEC is slightly decreased and then remains same for LBI-15. It is also observed that there is a uniform increase in lattice expansion with temperature in all the samples. The thermal expansion increases when the attraction forces decrease. Also, for fixed metal-oxygen stoichiometric ratio, the TEC increases only due to increase in lattice vibrations [11, 78]. However, if there is a loss of oxygen lattice at the higher temperatures, then increase in lattice expansion is expected [79, 80]. The Ba-substitution at La-site introduced the oxygen vacancies (Eqn. 4.14) in LBI samples, which leads to an initial increase in lattice expansion with substitution. Furthermore, for LBI-10 and LBI-15, cubic phase is co-formed along with orthorhombic phase, which could lead to decrease in overall thermal expansion in these samples due to higher crystal ordering than orthorhombic phase. The TEC value for this system is in the required range for SOFC applications.

4.5.5. TGA analysis:

Fig. 4.40 shows the TGA of as-sintered samples in N_2 atmosphere. Except, unsubstituted sample (LBI-0), all the samples show regular weight loss with temperature. The maximum weight loss occurs up to 300 °C, which is mainly due to hygroscopic nature of these samples [15]. Moreover, the weight loss increases uniformly with substitution. This phenomenon can be explained on the basis of Ba-substitution at La-site, which could decreases the cation-oxygen bond strength, and leads to release of lattice oxygen a higher temperature. It indicates that higher Ba-substitution also decreases the stability of these samples at intermediate temperature range.

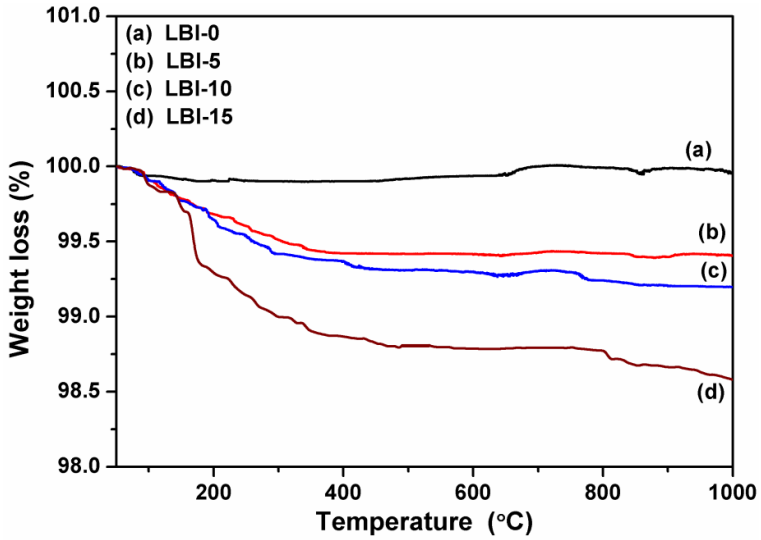

Fig. 4.40: TGA of as-sintered LBI samples in N_2 atmosphere.

4.5.6. Impedance analysis:

Impedance spectroscopy is used to analyze the conductivity behavior of the synthesized samples in a frequency range 30-10^6 Hz and from RT to 700 °C. Fig. 4.41(a-b) represents the Nyquist plots of LBI-0 and LBI-5 samples at 500 °C in air. The equivalent circuit diagram representing the bulk response is represented by a parallel resister-constant phase element (R-Q), as shown in an inset of Fig. 4.41(a). Constant phase element (Q) is characterized by two parameters, C_Q and n. Corresponding capacitance can be calculated from the equation given below [81]:

$$C = (R^{1-n}C_Q)^{1/n} \qquad (4.11)$$

here, the measuring cell has the bulk capacitance (C_b) and bulk interior resistance (R_b) in parallel. The capacitance (C_Q) values for LBI-0 (Fig. 4.41a) and LBI-5 (Fig. 4.41b) comes out to be 0.5×10^{-11} and 8.2×10^{-11} F, respectively.

It indicates that the nature of the semicircle is due to the grain interior (bulk property) [82]. Moreover, from Fig. 4.41(a-b), it is observed that the values of R_b reduced from 1000 k-4.58 kΩ. This sudden fall in grain interior resistance with Ba substitution, is due to the formation of oxygen vacancies in the lattice site as shown by Kroger-Vink notation [79].

$$2BaO \xrightarrow{La_2O_3} 2Ba'_{La} + 2O_o^x + V_o^{\bullet\bullet} \qquad (4.12)$$

Moreover, the effect of grain boundary contribution of LBI-5 cannot be resolved at this temperature range.

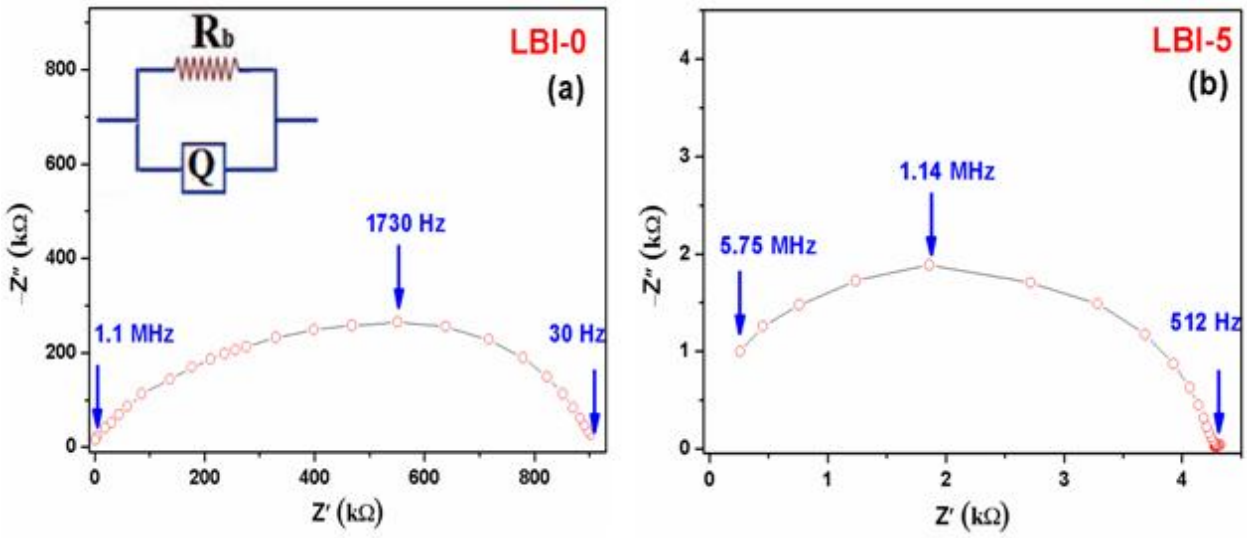

Fig. 4.41: Nyquist plots of (a) LBI-0 and (b) LBI-5 sample at 500 °C.

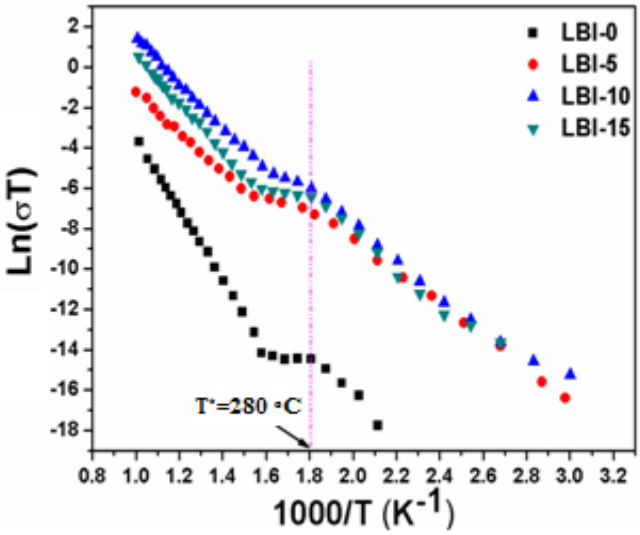

Fig. 4.42: Arrhenius plots for $La_{1-x}Ba_xInO_{3-\delta}$ samples.

Fig. 4.42 shows the electrical conductivity of these samples as a function of temperature in air. The oxide ion transport number of $La_{1-x}Ba_xInO_{3-\delta}$ system is already reported to be unity in air [65, 83]. The conductivity values and activation energy (E_a) calculated from Arrhenius plot are listed in Table 4.22.

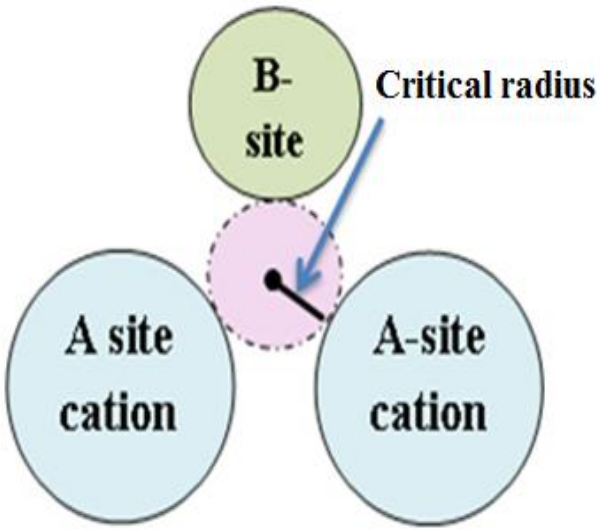

Fig. 4.43: Critical radius at the bottleneck of ABO_3.

The two regions are clearly distinguishable in Arrhenius plot, which indicates the change of the conduction mechanism with the increase in temperature in all the samples. Moreover, H_2O incorporation below 300 °C in the vacancy site has already been reported in literature for similar orthorhombic perovskites [35, 64]. Therefore, release of these water contents at 280 °C could lead to non-linear nature of present Arrhenius plot (Fig. 4.42). The conductivity

behavior can be explained in two temperature regions, i.e. region I; 50-280 °C and region II; 400-700 °C. Region I represent $La_{1-x}Ba_xInO_{3-\delta}.nH_2O$, where LBI is reported as mixed ionic conductor [64], i.e., oxide ion and hole conduction takes place in this region. Moreover, the ionic conductivity increases with substitution up to LBI-10 and decreased slightly for LBI-15 sample. The X-ray analysis exhibits the single orthorhombic phase in LBI-5, and a mixture of cubic and orthorhombic phases were observed for LBG-10 and LBG-15. So, the abrupt increase of ionic conductivity from LBI-0 to LBI-5 is due to Ba substitution at La site, which produces oxygen vacancies (Eqn. 4.14), and enhanced the overall conductivity of the system. With further substitution, a cubic phase formation occurs, which further enhances the overall ionic conductivity up to x=0.10 (LBI-10). For LBI-15, the conductivity lies between LBI-5 and LBI-10.

Table 4.22: Conductivity and activation energy of as-sintered LBI samples.

Sample name	$\sigma \times 10^{-3}$ (S/cm) at 700 °C	E_a (eV)	
		200-300°C	600-700 °C
LBI-0	0.002	0.98	1.21
LBI-5	0.013	0.76	0.82
LBI-10	3.00	0.78	0.88
LBI-15	0.05	0.77	0.84

This slight decrease of conductivity can be explained on the basis of the amount of oxygen vacancies, which increases with Ba-substitution, but effective mobile oxide ions, which are acting as the charge carrier decreases. This behavior with higher Ba-substitution is well reported in literature [34, 64, 65]. Moreover, in perovskite structure (ABO_3), *A*-cation occupies the corner position, *O* at face centre positions and *B*-lies in the body centre position of the cubic structure. A circle inscribing two *A*-site cations and one *B*-site cation leads to the formation of the critical circle (Fig. 4.43). In the present case, Ba-substitution at La-site decreases the critical radius of this circle. This decrease in critical radius acts as an obstacle to the diffusion of oxide ions. So, the ionic conductivity decreases for 15 mol% Ba substituted $LaInO_3$. In region II, which is speculated to be anhydrous Ba-substituted $LaInO_3$, follow the similar trend in all samples. The increase in activation energy in region II could be due to the dehydration above 280°C. So, above 280°C, the available charge carriers are oxide ion vacancies, and these trapped oxygen vacancies become mobile above transition temperature T^* (Fig. 4.42). The release of the trapped oxygen vacancy hypotheses has been

already reported for oxide ion conductors such as Ba-substituted $LaGaO_3$ and stabilized zirconia [20, 84]. The activation energy calculated for all these samples is given in Table 4.22. It is found that, the activation energy is invariant with Ba-substitution in all substituted samples and is of same order as that of other reported high oxide ion conductors [34, 64]. These results indicate that the present system is an oxide ion conductor and thermally stable in intermediate temperature range of SOFCs.

4.6. $La_{1-x}Ca_xInO_{3-\delta}$ ($0 \leq x \leq 0.20$) systems:

In this series, a systematic study of Ca-substituted $LaInO_3$ perovskites has been done. Effect of Ca^{2+} substitution on conductivity has been analyzed. The structural features as well as their co-relation with ionic conductivity, morphology has been investigated in detail.

4.6.1. X-ray diffraction analysis:

Structural features of Ca-substituted $LaInO_3$ were investigated using X-ray diffraction (XRD). The XRD patterns of $La_xCa_{1-x}InO_{3-\delta}$ at x= 0.0, 0.05, 0.10, 0.15 and 0.20 are shown in Fig. 4.44(a). The XRD peaks were indexed with orthorhombic structure (ICDD card no. 01-072-3823). The calculated lattice parameters are given in Table 4.23. The XRD data confirmed that samples $La_{1-x}Ca_xInO_{3-\delta}$ ($0.0 \leq x \leq 0.10$) are single phase. Furthermore, for LBI-15 and LBI-20, the solid solubility limit of $La_{1-x}Ca_xInO_{3-\delta}$ system gets disturbed and some low-intensity additional peaks due to secondary phase, i.e. $CaIn_2O_4$ (ICDD card no. 00-017-0643) have also appeared in Fig. 4.44(a). It indicated that the solubility of Ca^{2+} in the $LaInO_3$ perovskite structure lies in the range of $0.0 < x \leq 0.10$. The lattice volume trend justifies the solid solubility limit upto LCI-10 as shown in Fig. 4.44(b). From FWHM values, LCI-10 possesses highest disorderness in this system. In addition, the microstrain in the parent system is calculated by Williamson-Hall's equation (4.1). The calculated values are given in Table 4.23. These values indicate the uniform increase in microstrain with the increase in Ca-substitution for all the synthesized samples. Interestingly, it is observed that the the lattice volume increases with Ca-concentration up to LCI-10. The initial increase in lattice volume can be explained on the basis of energy of solution of Ca^{2+} into the La^{3+} or In^{3+} sites. The reaction of solution of CaO in $LaInO_3$ on La(A) or In(B) site is:

$$CaO + \frac{1}{2}O_{O_2}^{x} + La_{La}^{x} \rightarrow Ca'_{La} + \frac{1}{2}V_{\ddot{O}_2} + \frac{1}{2}La_2O_3 \qquad (4.13)$$

It is already reported that CaO can substitute for both La and In site in $LaInO_3$ [41, 85-86]. The probability of Ca to occupy La- or In-site depend upon the energy of solution. Lesser the energy of solution, higher will be the tendency to occupy the respective site. Trezo *et al.* [41]

have reported the energy of solution values of Ca^{2+} in La- and In-site of $LaInO_3$. Moreover, the samples were sintered at 1400 °C for 12 h, so there is likely probability of vaporization of In, which may be the cause of larger substitution of Ca-ion at In-site. Also, there is considerable ionic radii difference between Ca^{2+} (r_{VIII} =1.12Å) and In^{3+} (r_{VIII} =0.94Å). So, the resultant unit cell should expand with Ca-substitution. Between 15 to 20 mol% Ca (i.e. LCI-15-LCI-20), the behavior of change in lattice volume (Table 4.23) could be due to formation of secondary phase ($CaIn_2O_4$). These results are in accordance earlier reported work for similar perovskite system [54].

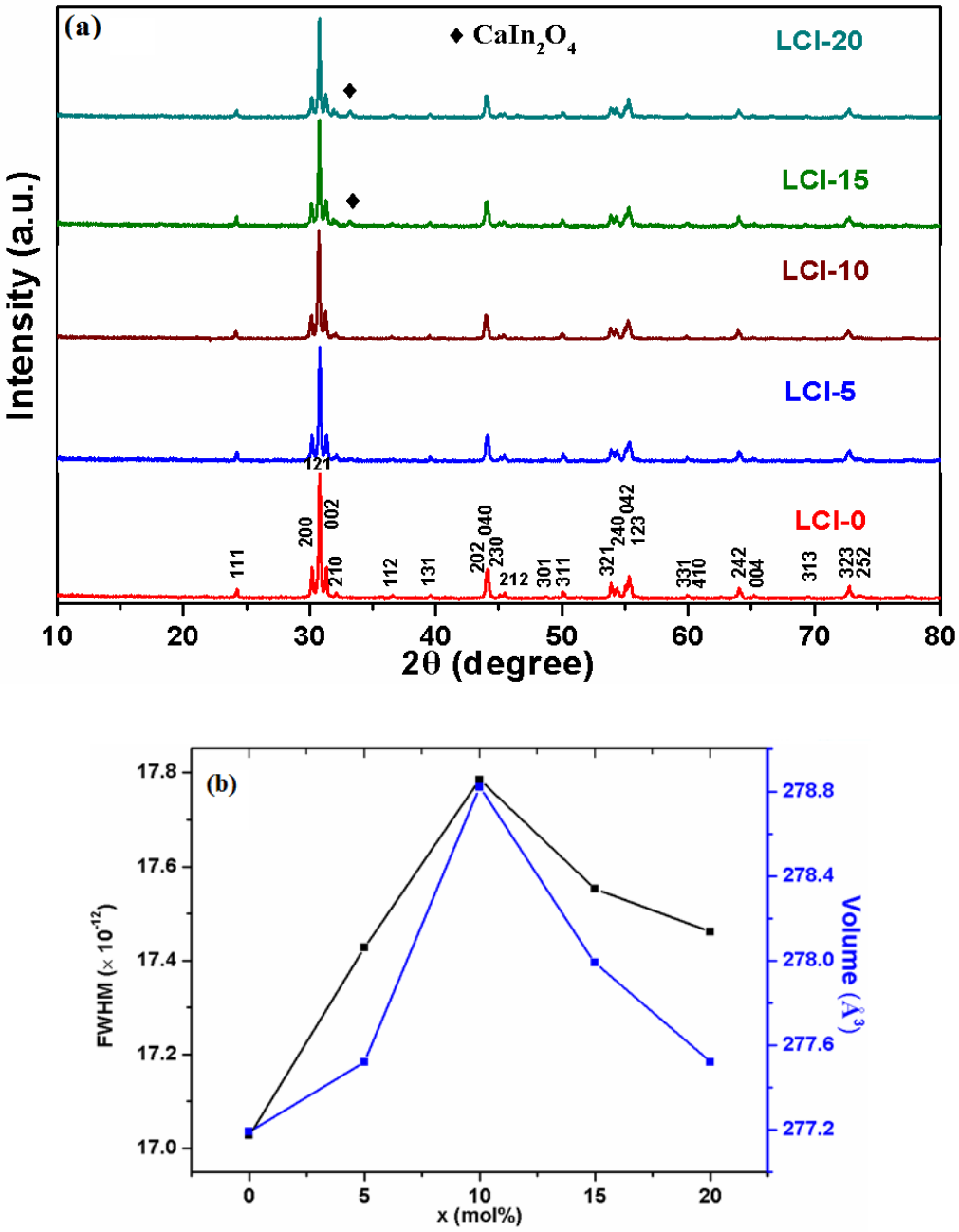

Fig. 4.44: (a) X-ray diffraction pattern of $La_{1-x}Ca_xInO_{3-\delta}$ at LCI-0,LCI-5, LCI-10, LCI-15 and LCI-20, **(b)** FWHM and lattice volume with substituent concentration.

Moreover, it has been observed that for LCI-0 (unsubstituted), the peaks have shifted by ~0.1° to higher angle with respect to the standard $LaInO_3$ (ICDD card no. 01-072-3823). It could be due to the presence of macro-strain in the sample during the sintering process.

Table 4.23: Lattice parameters, strain, density and FWHM of LCI samples.

Sample name	**Lattice parameters**			**Lattice volume**	**Strain (ϵ) $\times 10^{-5}$**	**Relative density (%)**	**Raman band 386 /cm (FWHM)**
	a (Å)	b (Å)	c (Å)	V ($Å^3$)			
LCI-0	5.92	8.20	5.71	277.19	2.12	95	15.60
LCI-5	5.92	8.21	5.71	277.52	2.29	97	16.00
LCI-10	5.93	8.22	5.72	278.82	2.83	98	16.87
LCI-15	5.93	8.21	5.71	277.99	3.17	98	18.76
LCI-20	5.92	8.21	5.71	277.52	3.17	96	18.25

4.6.2. Raman analysis:

Raman spectra of Ca-substituted $LaInO_3$ sintered samples are shown in Fig. 4.45. In LCI system, all the Raman active modes are located in the 100-600 /cm spectral range. The Raman spectrum of $LaInO_3$ shows 11 bands at 109, 122, 142, 180, 200, 232, 263, 308, 351, 386 and 526 /cm as shown in Fig. 4.45. These spectral bands so obtained are in accordance with bands reported earlier for similar perovskite system [66, 87]. The Raman bands in the range 180-300 /cm correspond to tilt modes of InO_6. Similar type of tilt in FeO_6 octahedra have been reported by Thakur *et al.* [88] for $BiFeO_3$ systems. The spectral band at 200 /cm is due to InO_6 structural unit [72]. Moreover, the highest intensity peak at 386 /cm is attributed due to stretching mode [2]. Further, the Raman bands in 300-600 /cm region are assigned to vibration motion due to cation-oxygen-cation (In-O-In) groups [73].

On Ca-substitution, the Raman band from 180-300 cm^{-1} shows the red shift for single phase substituted samples, whereas, the partial shift is observed for samples containing secondary phase (Fig. 4.45). The red shift is most prominent in 200 cm^{-1} mode (inset of Fig. 4.45), which could be due to B-site substitution in perovskite lattice that leads to induced chemical pressure and changes the bond lengths of In-O bonds [89, 90]. In $LaInO_3$ structures, La occupies the corner positions, oxygen at the face centre and In at the body centre forming InO_6 octahedra in the cuboids. It is reported that red shift in Raman bands is obtained if there

is tensile stress in the unit cell [68, 91, 92], which leads to increase in lattice volume. In the present study, few percentages of Ca^{2+} (r_{VIII}=1.12Å) have replaced In^{3+} (r_{VIII}=0.94Å), that leads to softening of Raman bands (Fig. 4.45 inset).

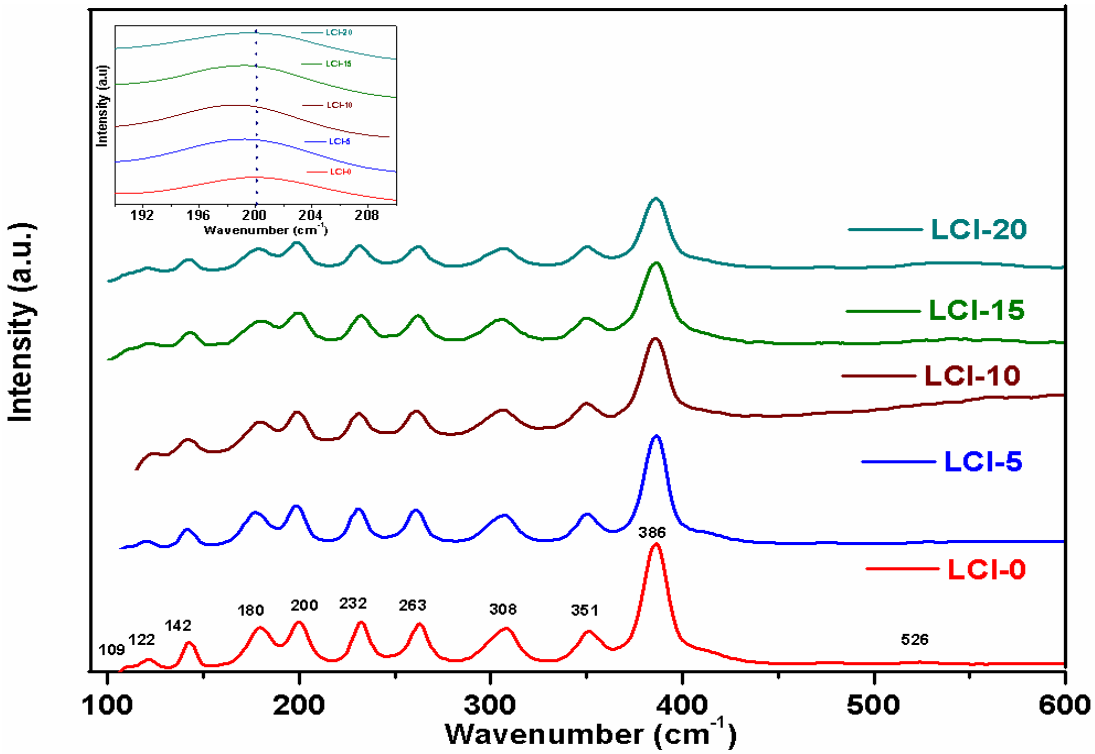

Fig. 4.45: Raman spectra of $La_{1-x}Ca_xInO_{3-\delta}$ at ×=0, 0.05, 0.10, 0.15 and 0.20.

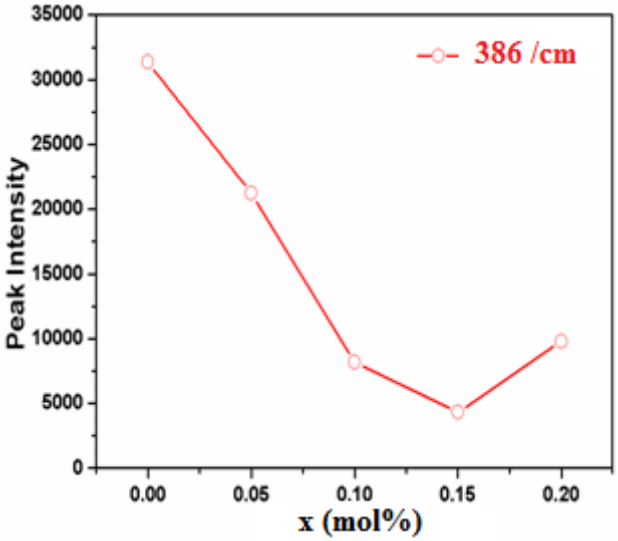

Fig. 4.46: Variation of Raman peak intensity (386 /cm) with composition (x).

Similar observation is also obtained in our XRD results as discussed in previous section. So, it can be concluded that for ×=0.0-0.10, Ca have mainly occupied In-site. With further Ca substitution (15-20 mol%), the red shift is decreased, which could be related to decreasing occupancy of Ca-substitution in In-site due to formation of secondary phase (Fig. 4.44a).

Moreover, the uniform decrease in intensity with Ca-substitution is also observed for almost all Raman bands. The decrease in intensity for highest intensity Raman band (386 cm^{-1}) is shown in Fig. 4.46. The decrease in intensity is due to interaction between oxygen vacancies created by Ca substitution, resulting a change in the local environment as reported earlier [2]. Moreover, the increase of FWHM (Table 4.23) with Ca-substitution suggests the weakening of cation-oxygen-cation (In-O-In) group in InO_6 octahedra [93]. Furthermore, it suggests the increase in oxygen disorder with substitution in the present system. The small hump in 500-600 cm^{-1} region is due to disorder induced Raman feature and expect its origin to reside in a lattice defect due to an existing oxygen deficit [94]. This type of phenomena is also reported by Xia *et al.* [38].

4.6.3. Microstructural analysis:

To study the morphology of the synthesized samples, the microstructures of the selected samples were further analyzed.

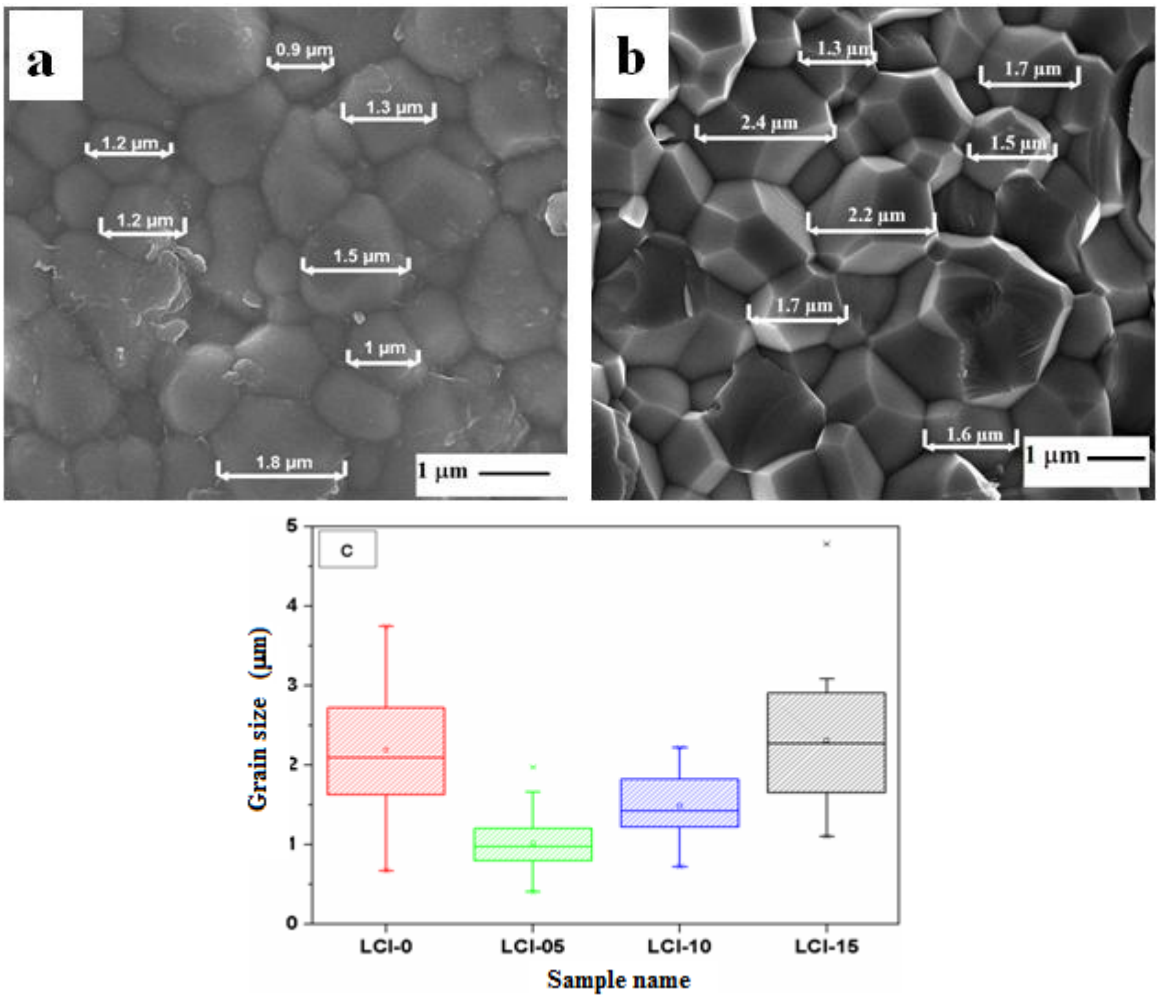

Fig. 4.47: The SEM micrographs of (a) LCI-5, (b) LCI-10 and (c) grain size distribution.

Fig. 4.47(a-b) shows the SEM micrographs of the LCI-5 and LCI-10 samples. The sintered samples exhibited fully dense packed grains having the hexagonal shape, which is more pronounced in LCI-10. These grains are uniformly distributed with minimum porosity. The relative densities of all the samples are ≥95% as listed in Table 4.23. The average grain size distribution is shown in Fig. 4.47(c). The average grain size of LCI-5 and LCI-10 is~1.2 µm and 1.5 µm, respectively. In addition, the grains size for LCI-5 is not uniform, which leads to higher grain boundary and lesser conductivity as discussed in conductivity section. In LCI-10, the densely packed uniform grains may reduce the scattering which may lead to higher conductivity in this sample. Moreover, the Ca-content increases the average grain size in all substituted samples. This behavior is similar to Ca-substituted $LaGaO_3$ system. The results indicated that Ca-substitution facilitates the grain growth through Ostwald ripening mechanism [95]. This mechanism suggests that Ca-content in the material may lower sintering temperature/time and leads to partial liquid phase sintering, which may enhance the average grain size with Ca-substitution in this series.

4.6.4. TEC analysis:

TEC values are investigated to analyze the compatibility of LCI with other components of SOFCs. All the compositions show the linear increase of TEC with temperature as shown in Fig. 4.48.

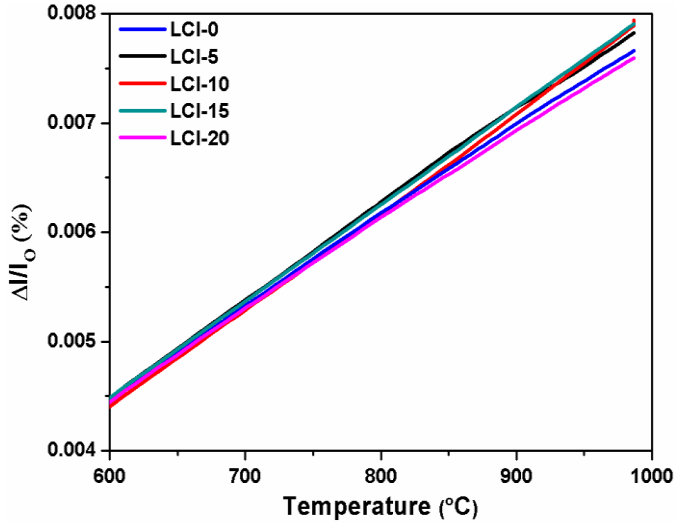

Fig. 4.48: Thermal expansion coefficient plots of LCI samples.

This increase is attributed to the weakening of the binding energy as a result of Ca substitution and creation of oxygen vacancies [11]. The TEC values calculated for the investigated samples are given in Table 4.24.

These values are in the required range for SOFC applications. It is observed that the linear change of lattices with substitution up to LCI-15 occurs, which is due to vacancy formation with Ca-content in this system. On the other hand, for LCI-20, there is a sharp decrease in TEC, which could be due to the presence of secondary phase ($CaIn_2O_4$), which suppresses the overall TEC of the system [57, 58, 79].

4.6.5. TGA analysis:

The thermal phase stability of synthesized samples at operating temperature range (600-800 °C) has been studied by thermogravimetric analysis of these samples. Fig. 4.49 shows the weight loss behavior of these samples in the inert atmosphere. All the Ca-substituted samples show higher weight loss compared to unsubstituted (LCI-0) sample. The weight loss is minimum (7% upto 1000 °C) for LCI-10 sample. It indicates that LCI-10 is most stable at the higher temperature in the inert atmosphere. Higher weight loss for LCI-15 (~12% upto 1000 °C) and LCI-20 (~9% upto 1000 °C) could be due to secondary phase, which may be less stable at the higher temperature region. Moreover, the volatile nature of In is also responsible for higher weight loss.

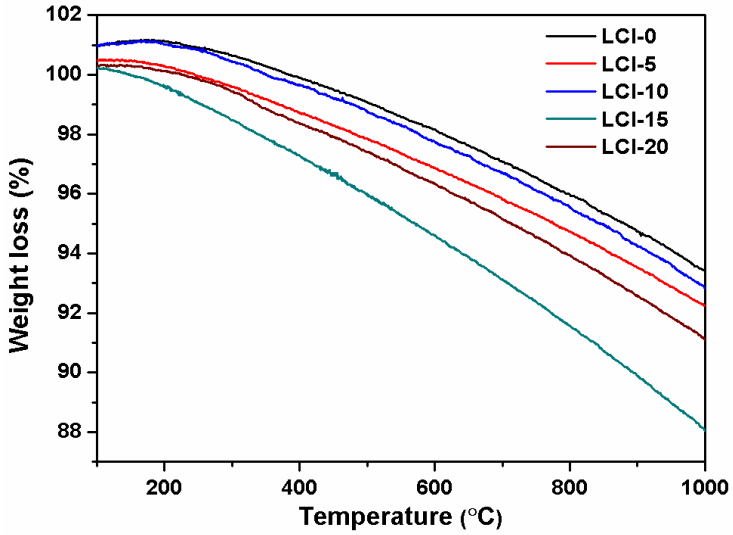

Fig. 4.49: TGA of as-sintered LCI samples in N_2 atmosphere.

4.6.6. Impedance analysis:

The impedance spectra so obtained could be resolved into three components as: the semicircle at the highest frequency side corresponds to bulk (grain) contribution, a grain boundary semicircle at intermediate frequencies and electrode polarization at low frequencies [54, 36]. Such a complete diagram is only observable in a narrow temperature range. The reason has been discussed extensively by Schouler *et al.* [36].

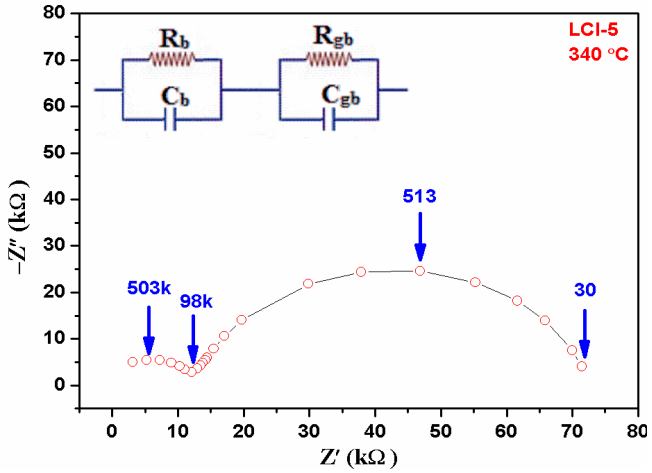

Fig. 4.50: Nyquist plot of LCI-5 sample, where numerical values represents frequency in Hz.

Nevertheless, it is generally possible to obtain the effect of bulk and grain boundary effects over a wide temperature range of interest. The Nyquist plot of LCI-5 sample is shown in Fig. 4.50. The equivalent circuit diagram representing the bulk, and grain-boundary contributions is shown in the inset of Fig. 4.50. The capacitance values corresponding to bulk and grain boundary contribution are 1.75×10^{-11} and 3.3×10^{-09} F, respectively. These capacitance values indicated that two components observed in the Nyquist plot corresponds to grain and grain-boundary effects in the operating temperature range. The electrode contribution has not appeared in Fig. 4.50. It could be due to limited frequency range of the instrument.

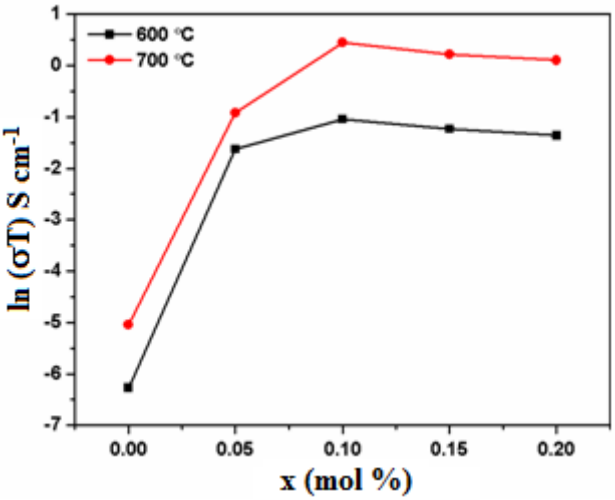

Fig. 4.51: Variation of ionic conductivity with composition (x).

The relationship of isothermal electrical conductivity of $La_{1-x}Ca_xInO_{3-\delta}$ versus Ca-substitution upto ×=0.2 is shown in Fig. 4.51. It is observed that the electrical conductivity increases up to ×=0.10 (LCI-10) and decreases with further substitution. The ionic conductivity depends on various parameters such as: substitution, mobility of conducting

ions, phase formation, density and porosity of the synthesized samples [54]. The highest conductivity of LCI-10 can be explained on the basis of increased lattice volume (as discussed in XRD section) and formation of anion vacancies with substitution. Since the ion conduction takes place through the free volume available between two *A*-site and one *B*-site cation formed in cuboid [65]. The calculated lattice volume for LCI-10 is maximum (Table 4.23), so, free volume is available for ionic conduction, which leads to higher conductivity of this sample among all the studied system. Moreover, the decrease in ionic conductivity for LCI-15 and LCI-20 samples could be due to formation of secondary phase ($CaIn_2O_4$), which in general is believed to segregate along the grain boundary region [54]. So, the formation of secondary phase has the dominant effect on decreasing the overall conductivity of the sample. This indicates that the conductivity results are strongly dependent on phase formed as discussed in previous sections. Further, the conductivity values obtained for LCI is higher than YSZ and slightly lower than LSGM at 700 ºC.

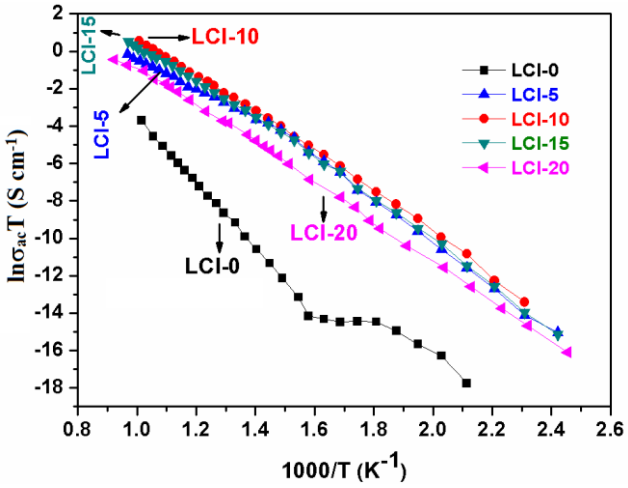

Fig. 4.52: The total conductivity LCI samples as a function of temperature.

The temperature dependence of the overall conductivity for LCI samples are shown in Fig. 4.52. In un-substituted sample (LCI-0), the two well defined conductivity regions are observed. At the low temperature region (T<300 °C), the conductivity is mainly due to mixed conduction (electronic and ionic). It could be because of the hygroscopic nature of lanthanum indate, which are reported as mixed ionic conductors in this region [35, 64]. Furthermore, above 300°C, the sample becomes dehydrated and the conductivity could be mainly due to flow of ions. Moreover, no such behavior was observed in Ca-substituted samples. It could be due to well packed grains leading to lesser porosity, high density and is responsible for non-hygroscopic nature of Ca-substituted samples. It is observed that the effect of Ca-substitution drastically increased the conductivity of the system up to x=0.10 (Fig. 4.52).

The change in slope in temperature range 420-495°C in substituted samples could be due to ordering-disordering vacancy cluster transformation [15, 39, 40]. The linear behavior above 500 °C, indicates that there may be no phase transformation in the intermediate temperature range (600- 800 °C). The activation energies were determined from a linear fit of the data using Arrhenius equation (4.3). The values of calculated activation energies are given in Table 4.24.

Table 4.24: Total conductivity, activation energy and TEC of LCI samples.

Sample name	σ (mS/cm) at 700 ºC	E_a (eV) (500-600 ºC)	TEC × 10^{-6} (/ºC) (500-1000 ºC)
LCI-0	0.002	1.15	8.79
LCI-5	1.03	0.93	9.01
LCI-10	1.64	0.97	9.10
LCI-15	1.28	0.97	9.16
LCI-20	0.41	0.94	8.33

There are several possible oxygen jumps, which were reported by Trejo *et al.* [41] in accordance with activation energy. The migration of oxygen ion takes place in skew curved path between two neighbor oxygen atoms than the straight trajectory (Fig. 4.53).

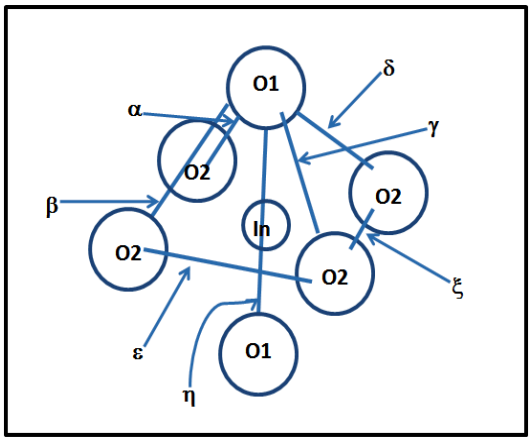

Fig.4.53: The distorted octahedral InO_6 in $LaInO_3$ indicating possible pathways of oxygen conduction [41].

Also, the possible hopping at normal conditions is jumping of O1 site into nearest O2 (Fig. 4.53), which require less activation energy. However, in the present study, the activation energies of substituted samples are in the range 0.93-0.97 eV. So, the possible paths for oxygen hopping, corresponding these values are δ and η as reported by Trezo *et al.* [41] (Fig. 4.53). These activation values indicated that the conductivity in the investigated samples is mainly ionic. Moreover, the activation values are higher than LSGM and are comparable with Sr-substituted $LaInO_3$ [96].

References

[1] P. Datta, P. Majewski, F. Aldinger, J. Alloys Compds., 438 (2007) 232.

[2] H.P. He, X. Huang, L. Chen, J. Phys. Chem. Solids, 62 (2001) 701.

[3] J. Xing, Z. Shan, K. Li, J. Bian, X. Lin, W. Wang, F. Huang, J. Phys. Chem. Solids, 69 (2008) 23.

[4] R.D. Shanon, Acta Crystallogr. Sect. A, 32 (1976) 751.

[5] H. Hayashi, H. Inaba, M. Matsuyama, N.G. Lan, M. Dokiya, H. Tagawa, Solid State Ionics, 122 (1999) 1.

[6] R.L. Cook, A.F. Sammells, Solid State Ionics 45 (1991) 311.

[7] V.D. Mote, Y. Purushotham, B.N. Dole, J. Theor. Appl. Phys., 6 (2012) 1.

[8] G.K. Williamson, W.H. Hall, Acta Metallurgica, 1 (1953) 22.

[9] P.R. Slater, J.T.S. Irvine, T. Ishihara, Y. Takita, J. Solid State Chem., 139 (1998) 135.

[10] H. Inaba, H. Hayashi, M. Suzuki, Solid State Ionics, 144 (2001) 99.

[11] P. Datta, P. Majewski, F. Aldinger, J. Eur. Ceram. Soc., 29 (2009) 1463.

[12] J.E. Baurele, J. Hrizo, J. Phys. Chem. Solids, 30 (1969) 565.

[13] R. Kant, K. Singh, O.P. Pandey, Int. J. Hydrogen Energy 33 (2008) 455.

[14] Z. Shui, R. Zhang, W. Chen, D. Xuan, Cons. Build. Mater., 24 (2010) 1761.

[15] Y.C. Wu, M.Z. Lee, Ceram. Int., 39 (2013) 9331.

[16] R. Gerhardt, J. Phys. Chem. Solids, 55 (1994) 1491.

[17] T. Ishihara, H. Matsuda, Y. Takita, J. Am. Chem. Soc., 116 (1994) 3801.

[18] P.S. Anderson, G.C. Mather, F.M.B. Marques, D.C. Sinclair, A.R. West, J. Eur. Ceram. Soc., 19 (1999) 1665.

[19] K. Huang, R.S. Tichy, J.B. Goodenough, J. Am. Ceram. Soc., 81 (1998) 2565.

[20] S. Kim, M.C. Chun, K.T. Lee, H.L. Lee, J. Power Sources, 93 (2001) 279.

[21] G. Chandra, S. Radha, A.K. Nigam, S. Prasad, R. Krishnan, J. Magn. Magn. Mater**.,** 83 (1990) 354.

[22] M.A. Howson, J. Phys. F, 14 (1984) 25.

[23] M. Feng, J.B. Goodenough, Eur. J. Solid State Inorg. Chem., 31 (1994) 663.

[24] J. Drennan, V. Zelizko, D. Hay, F.T. Ciacchi, S. Rajendran, S.P.S. Badwal, J. Mater. Chem., 7 (1997) 79.

[25] M. Kajitani, M. Matsuda, A. Hoshikawa, S. Harjo, T. Kamiyama, T. Ishigaki, F. Izumi, M. Miyake, J. Phy. Chem. Solids, 68 (2007) 758.

[26] W. Marti, P. Fischer, F. Altorfer, H.J. Scheel, M. Tadin, J. Phys. Condens. Matter., 6 (1994) 127.

[27] P. Lacorre, J.B. Torrance, J. Pannetier, A.I. Nazzal, P.W. Wang, T.C. Huang, J. Solid State Chem., 91 (1991) 225.

[28] X. Kuang, M.K. Green, H. Niu, P. Zajdil, C. Dikinson, J.B. Claridge, L. Jantsky, M.J. Rosseinsky, Nat. Mater., 7 (2008) 498.

[29] C.I. Thomas, X. Kuang, Z. Deng, H. Niu, J.B. Claridge, M.J. Rosseinsky, Chem. Mater., 22 (2010) 2510.

[30] M. Ghatee, M.H. Shariat, J.T.S. Irvine, Solid State Ionics, 180 (2009) 57.

[31] B. Dalslet, P. Blennow, P.V. Hendriksen, N. Bonanos, D. Lybye, M. Mogensen, J. Solid State. Electrochem., 10 (2006) 547.

[32] V.V. Kharton, F.M.B. Marques, A. Atkinson, Solid State Ionics, 174 (2004) 135.

[33] L. Malavasi, C.A.J. Fisher, M.S. Islam, Chem. Soc. Rev., 39, (2010) 4370.

[34] K. Kakinuma, H. Yamamura, H. Haneda, T. Atake, Solid State Ionics, 140 (2001) 301.

[35] T. Hashimoto, Y. Inagaki, A. Kishi, M. Dokiya, Solid State Ionics, 128 (2000) 227.

[36] E.J.L. Schouler, N. MesBahi, G. Vitter, Solid State Ionics, 9-10 (1983) 989.

[37] X. Zhao, N. Xu, K. Romito, K. Huang, A. Lucas, C. Qin, Advances in Solid Oxide Fuel Cells VIII (eds P. Singh, N. P. Bansal, M. Halbig, S. Mathur), John Wiley & Sons, Inc., Hoboken, NJ, USA, (2012) 85-91.

[38] X.L. Xia, Z.G. Liu, J.H. Ouyang, J. Power Sources, 196 (2011) 1840.

[39] D. Chakravarty, P. Singh, S. Singh, D. Kumar, O. Parkash, J. Alloys Compd., 438 (2007) 253.

[40] C. Haavik, E.M. Ottesen, K. Normura, J.A. Kilner, T. Norby, Solid State Ionics, 174 (2004) 233.

[41] E.R. Trejo, G. Tavizon, A.A. Landeros, J. Phys. Chem. Solids, 64 (2003) 515.

[42] C.J. Watson, A. Coats, D.C. Sinclair, J. Mater. Chem., 7 (1997) 2091.

[43] S. Gupta, K. Singh, Physica B, 431 (2013) 89.

[44] F.P. Koffyberg, J. Phys. Chem. Solids, 53 (1992) 1285.

[45] S. Thakur, M. Devi, K. Singh, Ionics, 20 (2014) 73.

[46] F. Urbach, Phys. Rev., 92 (1953) 1324.

[47] M. Kranjcec, I.P. Studenyak, M.V. Kurik, J. Non Cryst. Solids, 355 (2009) 54.

[48] D.I. Desnica, M. Kranjcec, B. Celustka, J. Phys. Chem. Solids, 52 (1991) 915.

[49] B. Abay, H.S. Guder, H. Efeoglu, Y.K. Yogurtcu, J. Phys. Chem. Solids, 62 (2001) 747.

[50] S.M. Wasim, G. Martin, C. Rincon, G.J. Sanchez Perez,J. Appl. Phys., 84 (1998) 5823.

[51] S.R. Johnson, T.J. Tiedje, J. Appl. Phys., 78 (1995) 5609.

[52] J.W. Stevenson, T.R. Armstrong, D.E. McCready, L.R. Pederson, W.J. Weber, J. Electrochem. Soc., 144 (1997) 3613.

[53] T.H. Etsell, S.N. Flengas, Chem. Rev., 70 (1970) 339.

[54] H. He, X. Huang, L. Chen, Solid State Ionics, 130 (2000) 183.

[55] H. He, X. Huang, L. Chen, Electrochim. Acta, 46 (2001)2871.

[56] K. Nomura, T. Takeuchi, H. Kageyama, Y. Miyazaki, Solid State Ionics 162-163 (2003) 99.

[57] J. Richter, P. Holtappels, T. Graule, L.J. Gauckler, Solid State Ionics, 179 (2008) 2284.

[58] M. Matsuda, K. Ihara, M. Miyake, Solid State Ionics, 172 (2004) 57.

[59] A. Manthiram, J.F. Kuo, J.B. Goodenough, Solid State Ionics, 62 (1993) 225.

[60] P.S. Sahoo, A. Panigrahi, S.K. Patri, R.N.P. Choudhary, Bull. Mater. Sci., 33 (2010) 129.

[61] V. Gupta, A. Mansingh, Phys. Rev. B, 49 (1994) 1989.

[62] J. Kimpton, T.H. Randle, J. Drennan, G. Auchterlonie, J. Mater. Res. Bull. 36 (2001) 639.

[63] K. Nomura, S. Tanase, Solid State Ionics, 98 (1997) 229.

[64] H.L. Kim, K.H. Lee, S. Kim, H.L. Lee, Jpn. J. Appl. Phys., 45 (2006) 872.

[65] D.S. Byeon, S.M. Jeong, K.J. Hwang, M.Y. Yoon, H.J. Hwang, S. Kim, H.L. Lee, J. Power Sources, 222 (2013) 282.

[66] J.D. Freire, R.S. Katiyar, Phys. Rev. B, 37 (1998) 2074.

[67] M.C. Saine, E. Husson, Spectrochim. Acta, 40A (1984) 733.

[68] T. Runka, M. Berkowski, J. Mater. Sci., 47 (2012) 5393.

[69] M.N. Iliev, A.P. Litvinchuk, V.G. Hadjiev, Y.Q. Wang, J. Cmaidalka, E.L. Meng, Y.Y. Sun, N. Kolev, M.V. Abrashev, Phys. Rev. B, 74 (2006) 214301.

[70] M.V. Abrashev, J. Backstrom, L. Borjesson, V.N. Popov, R.A. Chakalov, N. Kolev, R.L. Meng, M.N. Iliev, Phys. Rev. B, 65 (2002) 184301.

[71] E. Granado, J.A. Sanjurjo, C. Rettori, J.J. Neumeier, S.B. Oseroff, Phys. Rev. B, 62 (2000) 11304.

[72] M.S. Reddy, G.N. Raju, G. Nagarjuna, N. Veeraiah, J. Alloys Compds., 438 (2007) 41.

[73] P.L. Gentili, M. Penconi, F. Costantino, P. Sassi, F. Ortica, F. Rossi, F. Elisei, Sol. Energ. Mat. Sol. C, 94 (2010) 2265.

[74] G.L. Yuan, S.W. Or, H.L.W. Chan, J. Appl. Phys., 101 (2007) 064101.

[75] Y. Yang, J.Y. Sun, K. Zhu, Y.L. Liu, J. Chen, X.R. Xing, Physica B, 404 (2009) 171.

[76] Y. Shi, C.H. Wang, X.P. Jing, J. Electrochem. Soc., 155 (2008) 148.

[77] I.H. Campbell, P.M. Fauchet, Solid State Commun., 58 (1986) 739.

[78] H. Ullmann, N. Trofimenko, F. Tietz, D. Stöver, A.A. Khanlou, Solid State Ionics, 138 (2000) 79.

[79] K. Sood, K. Singh, O.P. Pandey, J. Mater. Sci., 47 (2012) 4520.

[80] L.W. Tai, M.M. Nasrallah, H.U. Anderson, D.M. Sparlin, S.R. Sehlin, Solid State Ionics, 76 (1995) 273.

[81] X. Guo, W. Sigle, J. Maier, J. Am. Ceram. Soc., 86 (2003) 77.

[82] J.T.C. Irvine, D.C. Sinclair, A.R. West, Adv. Mater., 2 (1990) 132.

[83] K. Kakinuma, H. Yamamura, H. Haneda, T. Atake, J. Therm. Anal. Cal., 57 (1999) 737.

[84] J.E. Bauerle, J. Hrizo, J. Phys. Chem. Solids, 30 (1969) 565.

[85] M. Cherry, M.S. Islam, C.R.A. Catlow, J. Solid State Chem., 118 (1995) 125.

[86] M.S. Khan, M.S. Islam, J. Phys. Chem. B, 102 (1998) 3099.

[87] M.N. Iliev, M.V. Abrashev, H.G. Lee, V.N. Popov, Y.Y. Sun, C. Thomsen, R.L. Meng, C.W. Chu, Phys. Rev. B, 57 (1998) 2872.

[88] S. Thakur, O.P. Pandey, K. Singh, Phase Transitions, 87 (2014) 527.

[89] B. Ramachandran, M. S. Ramachandra Rao, J. Appl. Phys., 112 (2012) 073516.

[90] B. Ramachandran, A. Dixit, R. Naik, G. Lawes, M. S. R. Rao, J. Appl. Phys.,111 (2012) 023910.

[91] P. Byszewski, R. Aleksiyko, M. Berkowski, J.F. Finowicki, R. Diduszko, W. Gebickic, J. Baran, K. Antonova, J. Mol. Struct., 792-793 (2006) 62.

[92] M. Baldini, D.D. Castro, M.C. Guidi, J. Garcia, P. Postorino, Phys. Rev. B, 80 (2009) 045123.

[93] W. Zhang, Z. Wang, X.M. Chen, J. Appl. Phys., 110 (2011) 064113.

[94] V.B. Podobedov, D.B. Romero, A. Weber, J.P. Rice, R. Schreekala, M. Rajeswari, R. Ramesh, T. Venkatesan, H.D. Drew, Appl. Phys. Lett., 73 (1998) 3217.

[95] A. Sinha, B.P. Sharma, P. Gopalan, Electrochim. Acta, 51 (2006) 1184.

[96] D. Lybye, F.W. Poulsen, M. Mogenson, Solid State Ionics, 128 (2000) 91.

CONCLUSIONS AND FUTURE SCOPE

5.1. Conclusions:

In this work, alkaline earth metals (Ca^{2+}, Sr^{2+} and Ba^{2+}) are substituted at A-site in $LaGaO_3$ and $LaInO_3$ series. The motive of the present work is to achieve better ionic conductivity without compromising other properties required for solid electrolyte such as stability, higher density, compatible TEC values (9-13 $\times 10^{-6}$ /°C) at operating temperature of SOFC. It was expected that substitution of aliovalent impurity will produce oxygen vacancies and lead to the disordered perovskite structure, which will increase the overall electrical conductivity of the system. Various characterization techniques are used to verify the synthesized phase, stability, morphology, density, TEC, phase stability and electrical conductivity.

The present systems ($La_{1-x}M_xNO_{3-\delta}$, where M=Ca, Sr and Ba, N=Ga and In) have been synthesized using solid-state reaction method. The ionic radii of aliovalent impurity played an important part in structure formation and other properties at operating temperature range (600-800 °C) of IT-SOFCs. The six series so synthesized are concluded as follows:

The solid solubility limit in $La_{1-x}Sr_xGaO_{3-\delta}$ system is $x \leq 0.10$. All the synthesized samples (except LSG-5) show good sinterability and high relative density. For LSG-10, uniform grain distribution with the relatively lesser grain boundary region is observed in SEM micrographs. The Sr-substitution for La-site in $La_{1-x}Sr_xGaO_{3-\delta}$ system has the significant effect on the conductivity as well as lattice expansions with temperature. TEC of LSG-10 sample (9.46 $\times$ 10^{-6} /°C) from 600-800 °C is in the required limit for SOFC applications. Higher Sr-substitution stabilized the rhombohedral phase to room temperature. The conductivity of single phase samples (LSG-0, LSG-5 and LSG-10) is dominated by the grains. On the other hand, the conductivity of LSG-15 sample is low due to secondary phase formation and higher grain boundary effect. LSG-10 shows the highest conductivity (2.37 $\times$ 10^{-3} S/cm) at 800 °C with activation energy of 0.81 eV from 600-800 °C range.

In $La_{1-x}Ba_xGaO_{3-\delta}$ ($\times$= 0.0-0.20) series, the XRD result indicates the formation of secondary melilite phase ($LaBaGa_3O_7$) in all substituted samples. Rietveld and TEC analysis indicated the stabilization of rhombohedral phase at higher Ba-content, which enhances the overall conductivity of the system. Among all the synthesized samples, LBG-15 is relatively most

thermally stable. The highest conductivity observed is 6×10^{-3} S/cm (at 800 °C) for LBG-15 sample. The activation energy calculated from Arrhenius plot confirm that overall conductivity is dominated by oxide ions. The phenomenon of ordering-disordering of oxygen vacancy occurred in the range 570-670 °C.

A single phase is formed up to 10 mol% of Ca-substitution in $La_{1-x}Ca_xGaO_{3-\delta}$. The lattice parameters decrease with Ca-substitution up to solid solubility limit after that lattice parameters remain invariant with substitution following Vegard's rule. Urbach energy calculations from UV-visible data confirmed the disorderness/defects increases up to LCG-10. The SEM micrographs indicated densely packed grains in this system. LCG-10 shows the highest conductivity in all the studied samples of this series. The value of activation energy indicated the ionic dominated conduction within the system.

The $La_{1-x}Sr_xInO_{3-\delta}$ series show higher solid solubility limit as compared to earlier studied similar systems. The higher content of Sr^{2+} leads to formation of secondary phase. The presence of oxygen vacancies might be higher in the LSI-23 sample. The uniform grain distributions, less porosity and higher vacancies of oxygen lead to better conductivity in the LSI-23 sample. At the higher temperatures, the conductivity phenomena change from protonic to oxide ion conductivity in all the samples. The thermal expansion of LSI-23 sample (9.15×10^{-6} /°C from 600-800 °C) is in the required range for SOFC applications.

The solid solubility for Ba-substitution is less than 10 mol% in $La_{1-x}Ba_xInO_{3-\delta}$ series. The structural refinement of 10 and 15 mol% indicates the co-existence of two phases, namely orthorhombic and cubic with similar chemical formula. Raman analysis indicated the A-site substitution of Ba-ion and formation of oxygen vacancies. The presence of cubic (minor) phase enhances the conductivity with lower TEC. The calculated TEC values of the system are suitable for SOFC applications. LBI-10 shows the highest ionic conductivity (7.3×10^{-3} S/cm at 800 °C) among all investigated samples with well packed grains, which is the optimum composition for its use as solid electrolyte.

The $LaInO_3$ formed single phase up to 10 mol% of Ca-substitution. Ca-substitution leads lattice expansion due to partial Ca^{2+} occupancies at In-sites (B-sites). It is also confirmed by Raman bands, particularly the 180-300 cm^{-1} shift to the lower wave number. The decrease in intensity and an increase in FWHM in Raman bands with substitution indicated the disorderness in the system. SEM micrographs exhibit closely packed grains with good

apparent density of the present system. TEC values obtained for LCI are in the compatible range with other components of SOFCs. The Arrhenius plots of all LCI samples show almost linear behavior and activation energy values indicated that the conduction is dominated by ions. The ionic conductivity of LBI-10 (σ=0.07 S/cm) is nearly one order less than LSGM (σ=0.1 S/cm) at 800 °C. For $LaInO_3$ system, the electrical conductivity strongly dependent on the alkaline-earth substitution and follows the order: Ba>Sr>Ca.

5.2. Scope of the future work:

After analyzing the data presented in the thesis, the following suggestions are recommended for further investigation:

The sample preparation plays an important role to improve the ionic conductivity. Therefore reducing atmosphere conditions should be created inside the furnace for conductivity measurement of the samples. The interaction study of best conductive series, i.e. LBI should be performed with other components of SOFCs.